



Max-Planck-Institut für Metallforschung
Stuttgart

Phase Transformations in Interstitial Pd-B Alloys

Tilmann Georg Berger

Dissertation
an der
Universität Stuttgart

Bericht Nr. 164
April 2005

Meinen Eltern gewidmet

Phase transformations in interstitial Pd-B alloys

Von der Fakultät Chemie der Universität Stuttgart zur

Erlangung der Würde eines Doktors der Naturwissenschaften (Dr. rer. nat.)

genehmigte Abhandlung

Vorgelegt von

Tilmann Georg Berger

aus Stuttgart

Hauptberichter: Prof. Dr. Ir. E.J. Mittemeijer

Mitberichter: Prof. Dr. T. Schleid

Mitprüfer: Prof. Dr. F. Aldinger

Tag der mündlichen Prüfung: 20.04.05

INSTITUT FÜR METALLKUNDE DER UNIVERSITÄT STUTTGART
MAX-PLANCK-INSTITUT FÜR METALLFORSCHUNG STUTTGART

2005

Contents

1. Introduction.....	7
2. Static displacements of Pd in the solid solution PdB_y (0 < y < 0.2) as determined by neutron diffraction.....	13
2.1. Introduction.....	14
2.2. Experimental.....	16
2.2.1. Preparation.....	16
2.2.2. X-ray diffraction.....	17
2.2.3. Neutron diffraction.....	17
2.2.4. Rietveld refinement.....	18
2.3. Results.....	19
2.3.1. X-ray diffraction experiments.....	19
2.3.2. Rietveld refinement of neutron diffraction data.....	20
2.4. Discussion.....	22
2.4.1. Comparison with EXAFS experiments.....	22
2.4.2. Comparison with theoretical predictions and with experimental observations of static displacements in defect-NaCl type transition metal nitrides and carbides.....	24
2.5. Conclusions.....	27
3. A time-resolved X-ray powder diffraction method to trace the decomposition of PdB_y solid solutions.....	29
3.1. Introduction.....	30
3.2. Experimental.....	31
3.2.1. Preparation and heat treatment.....	31
3.2.2. X-ray diffraction measurements.....	32
3.3. Data evaluation method.....	32
3.3.1. X-ray data evaluation.....	33

3.3.2.	Penalty functions to achieve stability in refinements of $p(\nu)$	34
3.4.	Results and Discussion	35
3.5.	Conclusions.....	38
4.	On the formation and crystal structure of the Pd₆B phase	39
4.1.	Introduction.....	40
4.2.	Possible ordering patterns for B in Pd ₆ B	44
4.3.	Experimental.....	46
4.3.1.	Preparation of the Pd-B alloys	46
4.3.2.	DSC Measurements	48
4.3.3.	X-ray diffraction measurements	49
4.3.4.	Neutron diffraction measurements.....	49
4.3.5.	TEM sample preparation.....	50
4.4.	Results.....	51
4.4.1.	Thermal analysis; phase transition ordered Pd ₆ B \rightleftharpoons disordered PdB _{1/6} ..	51
4.4.2.	Electron diffraction; type of B ordering in the Pd ₆ B phase	53
4.4.3.	X-ray powder diffraction; identification of two-phase equilibria.....	55
4.4.4.	Neutron diffraction; structure parameters of Pd ₆ B	60
4.5.	Discussion.....	64
4.5.1.	The ordered arrangement of B in Pd ₆ B.....	64
4.5.2.	Consequences for the constitution of the binary system Pd-B	68
4.6.	Conclusions.....	71
5.	The Pd-rich part of the Pd-B phase diagram	73
5.1.	Introduction.....	74
5.2.	Solid solution	76
5.3.	Miscibility gap in the solid solution field	77
5.4.	Low-temperature phases	79
5.4.1.	Pd ₆ B phase:	80
5.4.2.	'Pd ₅ B' phase:	82
5.5.	Conclusions for the phase diagram.....	86
6.	Zusammenfassung der Dissertation in deutscher Sprache	89
6.1.	Einleitung.....	90
6.2.	Experimentelles.....	90

6.3. Neutronenbeugung: Statische Auslenkungen der Palladiumatome im PdB _y -Mischkristall ($0 < y < 0.2$)	92
6.4. Eine zeitaufgelöste Methode zur Beschreibung der Entmischung im PdB _y Mischkristall	93
6.5. Die Tieftemperaturphasen Pd ₆ B und ‚Pd ₅ B‘	95
6.5.1. Die Pd ₆ B-Phase	95
6.5.2. Die ‚Pd ₅ B‘-Phase	98
6.6. Zusammenfassung und Phasendiagramm	99
References	101
Curriculum Vitae	105
Danksagung	107

1.

Introduction

Metals constitute one of the most important group of materials used to craft tools since mankind acquired the necessary knowledge to extract metals from raw ore. This is due to the valuable and for many different purposes adjustable properties of metals. For a long time in history, improvement of the quality of metallic workpieces or jewellery, mostly bronze, steel and precious metals, was achieved on a largely empirical basis by varying the composition of the alloys and the applied heat treatments. A deeper understanding of the importance of the microstructure, e.g. the kind and density of crystal defects and the distribution of chemical elements and different phases in the metal, was only developed in the last century.

This research revealed that a profound knowledge in particular about the occurring phase transformations is required to make predictions about the resulting microstructure for a certain alloy composition and the applied heat treatment. A prerequisite for this is sufficient knowledge about the phase-equilibria between the components of an alloy and about the crystal structures adopted by the different phases, which are themselves very revealing with respect to the nature of long-range and local interactions between different atomic species.

Many alloys with attractive and adjustable mechanical properties contain interstitial solid solutions as important constituents, which are mainly phases formed by transition metals and small-sized elements such as carbon, nitrogen, oxygen, boron and hydrogen. However, the properties of substitutional solid solutions are still considerably better understood than those of interstitial solid solutions. This is probably due to the restricted number of systems with an extensive (terminal) interstitial solubility available for experimental investigations.

One, on the first view exotic interstitial phase, but as model system very interesting is the terminal palladium-rich solid solution PdB_y [1-12]. It is able to dissolve boron up to a B content corresponding to $\text{PdB}_{0.25}$ [9], the highest (terminal) solid solubility of B in a transition metal¹. This solid solution is a high-temperature phase which is only stable above about 450°C but which can, however, be retained at room temperature by quenching. The low-temperature regime consists of a miscibility gap, other two-phase areas and one or two low-temperature phases [4, 5, 10, 12] (see Figure 1.1).

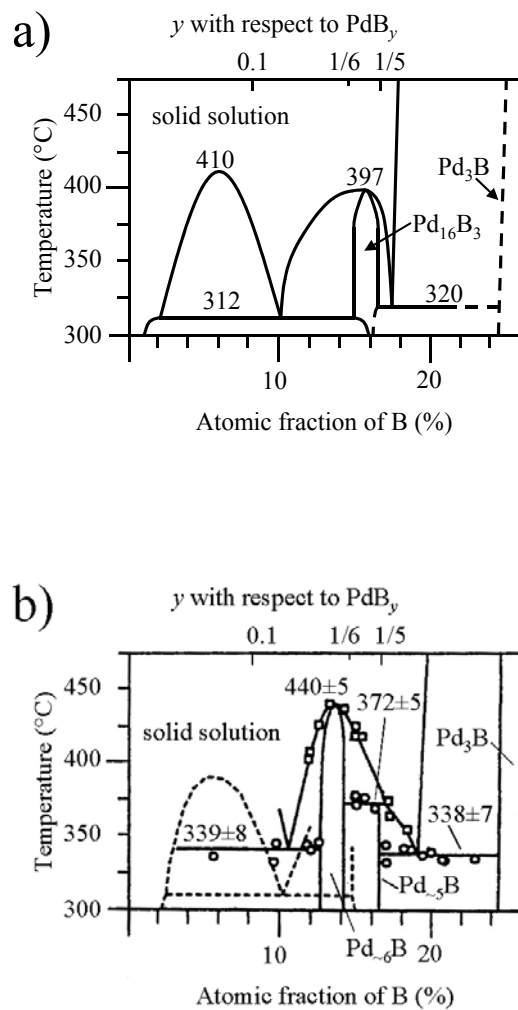


Figure 1.1. Pd-B phase diagrams according to (a) Ref. [5] and Ref. [10]

¹ y denotes the for crystallographic purposes more significant atomic ratio instead of the often for phase diagrams used atomic fraction. At the same time, y denotes the fraction of occupied octahedral interstices in the *fcc*-type Pd host lattice.

The Pd host lattice experiences an extraordinarily large expansion upon dissolving boron. Earlier H diffusivity investigations in Pd-B alloys [7] and EXAFS measurements [8] have indicated a random occupation of the octahedral interstices by the boron atoms in the solid solution. The observed lattice expansion upon incorporation of boron atoms suggested large static displacements of the Pd atoms from their ideal coordinates in the crystal resulting in a large attenuation of diffracted Bragg intensities (as described in terms of a Debye-Waller factor) with a characteristic dependence from the interstitial boron content [13]. Results from neutron powder diffraction experiments performed on a series of PdB_y alloys to study these static displacements as a function of composition are presented in Chapter 2 [14]. Indeed significant static displacements were observed for the PdB_y alloys when their diffraction patterns were compared to those of pure Pd, for which no static displacements should occur. However, no further systematic interdependency between the interstitial content y and the magnitude of the static displacements was obtained. Comparison with isotypic defect-NaCl (interstitial) type transition metal nitrides and carbides indicated that the measured values for the static displacements of the PdB_y alloys are exceptionally small. Additionally, the analysis of a compilation of data on static displacement parameters for these non-stoichiometric (interstitial) transition metal nitrides and carbides didn't show the expected magnitude of the composition-dependent static displacement parameter either, in contrast to the currently accepted theories. The latter seem to, however, work well for substitutional solid solutions [15].

The miscibility gap in the phase PdB_y is a rare phenomenon for binary interstitial solid solution with *fcc*-type structure. It was reported in the range of $0.02 < y < 0.11$ at 312°C with a critical point at 410°C ($y = 0.065$) [4]. An annealing time-resolved X-ray powder diffraction study of composition distributions is presented in Chapter 3 to trace the process of the decomposition of the solid solution upon annealing for various times in the field of the miscibility gap. For the analysis of the diffraction data a method was developed to fit the composition distribution of PdB_y in partially decomposed samples by a discretised probability-density function for composition to the diffraction data [16]. Three main component phases could be observed, first the initial solid solution with a phase content decreasing with increasing annealing time and secondly two boundary phases with increasing phase contents. It was shown that the decomposition into two solid solution phases is not complete even after the longest applied annealing times. One striking observation is that the observed final state after long annealing times with respect to the compositions of the boundary phases depends slightly on the boron content of the initial solid solution.

As mentioned above, one or two low-temperature phases have been reported in the composition range of $0.16 < y < 0.20$ without providing convincing and consistent crystal structure information [5, 10, 12]. The low-temperature phases occur in relatively small composition ranges because their formation is driven by ordering of boron atoms on the octahedral interstices. The loss of symmetry as exhibited by the occurrence of superstructure reflections and splitting of fundamental reflections (those reflections already occurring for the solid solution) is difficult to observe on the basis of X-ray powder diffraction data alone, (i) due to the low scattering power of the boron atoms for X-ray radiation leading to very weak superstructure reflections and (ii) due to the partially severe overlap between inequivalent fundamental reflections. Therefore, transmission electron microscopy and neutron powder diffraction were additionally employed to characterise in particular the superstructure reflections. The monoclinic superstructures of the low temperature phases Pd₆B (cf. Chapter 4 [17]) and ‘Pd₅B’ (cf. Chapter 5 [18, 19]) could be identified. The basic ‘rule’ underlying the boron ordering in the *fcc* host lattice was determined to be avoidance of simultaneous occupation of nearest and in particular of next nearest octahedral interstices by B. The crystal structure information obtained by electron and neutron diffraction allowed a successful interpretation of the X-ray powder diffraction data. Surprisingly, the Pd₆B phase was found to occur in two different forms: a *pseudotetragonal* form, which shows an apparent tetragonal splitting of the fundamental reflections, as well as a *pseudocubic* form, showing no visible splitting of the fundamental reflections as if Pd₆B was cubic. Yet, both forms show the same monoclinic superstructure.

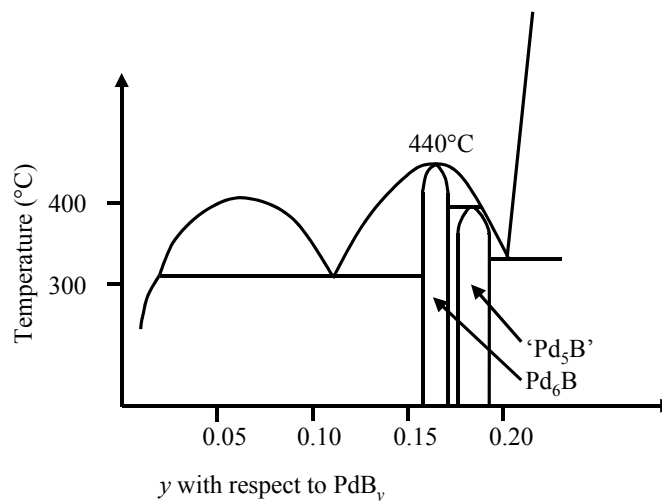


Figure 1.2. Pd-B phase diagram as presented in detail in Chapter 5.

Many disagreements about the crystal structure and composition of the low-temperature phases and about the miscibility gap in the Pd-B system remained in spite of several works on that topic. In the light of the recent crystallographic investigations, in particular about the Pd₆B and the incommensurate ‘Pd₅B’ low-temperature phases, a summary is given in Chapter 5 leading to a revised Pd-B phase diagram (see Figure 1.2), which explains nearly all observations from this and previous works.

2.

Static displacements of Pd in the solid solution PdB_y (0 < y < 0.2) as determined by neutron diffraction

T. G. Berger, A. Leineweber, E. J. Mittemeijer, and P. Fischer

The mean square atomic displacement parameter of Pd in the *fcc* interstitial solid solution PdB_y, $\langle u_{\text{Pd}}^2(y) \rangle$, was determined for atomic ratios of $y = 0.050$, 0.100 , and 0.184 using neutron powder diffraction data obtained at 15 K and 300 K. The values determined are significantly larger than those determined for pure Pd, $\langle u_{\text{Pd}}^2(0) \rangle$, at the same temperatures. Assuming that the dynamic (thermal) contribution to $\langle u_{\text{Pd}}^2(y) \rangle$ equals $\langle u_{\text{Pd}}^2(0) \rangle$, the static mean square atomic displacement parameter $\langle u_{\text{Pd}}^2(y) \rangle_{\text{st}} = \langle u_{\text{Pd}}^2(y) \rangle - \langle u_{\text{Pd}}^2(0) \rangle$ was obtained as $0.0020(1) \text{ \AA}^2$ to $0.0027(1) \text{ \AA}^2$. $\langle u_{\text{Pd}}^2(y) \rangle_{\text{st}}$ showed no systematic variation with y or the sample temperature. This contrasts with an expected $y \cdot (1 - y)$ concentration dependence for $\langle u_{\text{Pd}}^2(y) \rangle_{\text{st}}$. Comparison of $\langle u_{\text{Pd}}^2(y) \rangle_{\text{st}}$ with values for the static mean square displacements of the metal atoms in different defect-NaCl type transition metal nitrides and carbides indicates that the current values for Pd in PdB_y are exceptionally small.

2.1. Introduction

The palladium rich terminal solid solution PdB_y (*fcc* arrangement of Pd, B on octahedral sites without long-range order) is a remarkable model system for the study of the character of interstitial compounds. According to Hägg's rule of critical atomic radius ratio [20, 21], boron should actually be too large in order to fit into the *fcc* lattice [11]. Yet, the interstitial solubility extends to approximately $\text{PdB}_{0.20}$ (corresponding to ~17 at. % boron) above about 720 K [22], which is by far the largest one of boron in transition metals. The solid solution is only stable at elevated temperatures, but can be retained by quenching²; the low temperature region of the Pd-B phase diagram in the range of compositions Pd - $\text{PdB}_{0.20}$ consists of several low-temperature phases and two-phase regions [10, 12].

The wide range of solid solubility of B in Pd motivated a large number of studies of the PdB_y solid solution, in particular devoted to its crystal structure [4, 8, 11], its thermodynamic properties [4, 6] and the boron diffusivity [23, 24]. Besides the high solubility of B in Pd itself, also the large lattice expansion occurring upon dissolving B in Pd has attracted considerable interest [4, 11]. The following equation describes the dependence of the lattice parameter, a , upon composition y [11]

$$a = a_0 + \alpha \cdot y = 3.8920 \text{ \AA} + 0.6882 \text{ \AA} \cdot y \quad (2.1)$$

at room temperature, where y equals the average occupancy of the octahedral sites and is equal to y in the formula PdB_y . Eq. (2.1) can be used to derive the B contents of PdB_y solid solutions from X-ray diffraction data.³

Boron in the solid solution PdB_y appears to be randomly distributed (without long-range order) over the octahedral interstices, i.e. in the *fcc* unit cell any octahedral site can either be occupied by a B atom or by a vacancy. Around such locally different configurations the structure can relax by shifts of atoms relative to their positions in the average lattice. These displacements of the atoms are called "static displacements" [13] and are of a

² Internal friction experiments [23] hinted at local aging/decomposition effects of the material at room temperature on the time scale of months. However, there is no confirmation from other experiments, including those performed in the present project, for such effects.

³ It should be noted that equations slightly different from Eq. (2.1) have been reported previously (e.g. [4]) and used to derive compositions from cell parameters.

statistically largely uncorrelated nature, i.e. they do not cause diffraction line broadening. These static displacements attenuate the diffracted intensity in the same way as the dynamic (thermal) displacements due to the thermal vibrations do. Hence, both these static and dynamic displacements exhibit themselves in their effect on the diffracted intensity through a so-called Debye-Waller factor [13].

It has been derived on a common basis for *fcc* based solid solutions of interstitial character (MX_y , with M indicating the *fcc* arranged metal atoms and X the interstitial atoms, e.g. N, C, O, B, H... located on octahedral sites) and of substitutional character ($\text{M}'_y\text{M}''_{1-y}$, with M' and M'' indicating atoms of two different metal elements) that in the absence of short-range ordering the static mean square atomic displacements of a three-dimensional Gaussian distribution of M (for the substitutional case $\text{M} = \text{M}'$ or M''), $\langle u_{\text{M}}^2 \rangle_{\text{st}}$, should vary with the composition variable y (note that y in MX_y and in $\text{M}'_y\text{M}''_{1-y}$ denotes in both cases the atomic fraction of solute on the (sub)lattice available for the solute) like [13]:

$$\langle u_{\text{M}}^2(y) \rangle_{\text{st}} \sim \Omega_{\text{sf}}^2 \cdot y \cdot (1 - y) \quad (2.2)$$

where Ω_{sf}^2 is the so-called volume size factor, which has been taken in Eq. (2.2) as [26]

$$\Omega_{\text{sf}}^2 = \left. \frac{\partial \ln V(y)}{\partial y} \right|_{y=0} \quad (2.3)$$

where V is the volume of the *fcc* type unit cell. In order to use the volume size factor at $y = 0$ in Eq. (2.3), it has been assumed to be constant over the relevant composition range.

Extended X-ray Absorption Fine Structure (EXAFS) measurements on two *fcc* PdB_y solid solutions ($\text{PdB}_{0.114}$ and $\text{PdB}_{0.160}$) indicated the presence of static displacements for the Pd atoms [8]. The values reported for the static displacements are not compatible with the $y \cdot (1 - y)$ dependence as expected from Eq. (2.2). The reported static displacements for $\text{PdB}_{0.160}$ are even smaller than for $\text{PdB}_{0.114}$.

In this work, neutron powder diffraction experiments for PdB_y samples with $y = 0.050$, 0.100 , and 0.184 were performed, in order to determine the magnitude of the static displacements as a function of the boron content. Compared to X-ray diffraction, which is dominated by heavy atoms and characterised by an atomic scattering factor that decreases strongly with $\sin\theta/\lambda$ and thus leads to relatively weak high angle reflections, neutron

diffraction is particularly sensitive to light atoms and well suited for atomic displacement measurements because of relatively strong high angle reflections due to a coherent nuclear scattering length which does not depend on $\sin\theta/\lambda$. The results obtained will be discussed with respect to theoretical expectations [13, 25] and experimental results on static displacements in the structurally related defect-NaCl type transition metal carbides and nitrides.

2.2. Experimental

2.2.1. Preparation

The alloys were prepared from weighted amounts of ca. 3.5 g palladium foils (99.9 wt.%; Heraeus) and an appropriate amount of boron pieces (99.29% ^{11}B ; chemical purity 99.97 wt.%; Eagle Picher) by arc melting under argon (550 hPa, 99.999 vol.%; Messer Griesheim). The pure isotope ^{11}B was used instead of boron with the natural mixture of its isotopes, corresponding to about 20% ^{10}B , because ^{10}B has a very high neutron absorption cross section [27] and by its use the diffracted intensities would decrease dramatically.

The homogeneity of the reguli and their compositions was checked by means of X-ray diffraction (cf. Eq. (2.1)). For that purpose, small parts of the cast bulk were removed by filing from the top and bottom of the reguli using a diamond rasp. The filings were sealed under vacuum in quartz capsules, annealed at 1073 K for 5 min and subsequently quenched in water. The heat treatment was performed in order to relieve deformation stresses due to the filing procedure. If homogeneity had not been achieved, the corresponding regulus was remelted and the X-ray test procedure was repeated.

Homogenous reguli were fully filed. For relief of internal stresses, the resulting powders (ca. 2.5 g) were encapsulated under helium (ca. 500 hPa, 99.999 vol.%; Westfalen Reinstgase) in a quartz tube, heated for 5 min at 1073 K and water quenched.⁴

The same procedure, except for the arc melting, was performed to prepare a pure palladium powder sample from the initial palladium foil.

⁴ The He-atmosphere was chosen in order to achieve a fast cooling rate for the relatively large batch sizes.

2.2.2. X-ray diffraction

X-ray powder diffraction patterns were recorded at a Philips X'Pert MPD diffractometer applying Bragg-Brentano geometry and equipped with a primary beam monochromator selecting the $K\alpha_1$ component of the employed copper radiation (1.54056 Å). The samples consisted of a thin layer of the PdB_y alloy filings mixed with silicon powder ($a = 5.43102$ Å) as internal standard, deposited onto single crystalline silicon wafers with a (510)-plane parallel to the surface.

All reflections were recorded by measuring over 2θ -ranges sufficiently large to determine the background at both sides of each reflection. The reflection positions from the X-ray diffraction pattern were obtained by fitting the reflections with symmetrical pseudo-Voigt functions [28]. The 2θ -values of the PdB_y reflections were corrected using the positions of the Si reflections. The lattice parameters of the *fcc* solid solutions were subsequently determined by using the programme CELREF [29].

2.2.3. Neutron diffraction

Neutron diffraction experiments were performed at the HRPT powder diffractometer [30] installed at the spallation neutron source SINQ (Paul Scherrer Institute, Villigen, CH) employing the high intensity mode of the instrument. The wavelength of the neutron beam ($\lambda = 1.1966$ Å) was determined by using a silicon standard sample. The powder filings (Pd, $\text{PdB}_{0.050}$, $\text{PdB}_{0.100}$, $\text{PdB}_{0.184}$) were kept in closed vanadium cylinders ($d = 4$ mm). To avoid frozen air in the vanadium cylinders and for better thermal contact, the powders had been put into the cylinders in a glovebox under helium atmosphere. Each sample was measured for about 8 h at 15 K and at 300 K, respectively (closed cycle CTI refrigerator).

For the applied wavelength the absorption of a representative sample was determined by a transmission experiment as $\mu R = 0.065$ (R : cylinder radius, μ : linear absorption coefficient); for this value of μR , calculations show that the resulting angle dependent effects on reflection intensities are negligible [27]. Therefore, absorption was not considered in the course of all Rietveld refinements (cf. section 2.2.4.)

2.2.4. Rietveld refinement

Rietveld refinement of the neutron diffraction patterns was performed using the programme Jana2000 [31]. A fixed background was estimated from measured intensities at a series of 2θ values in between occurring reflections and subtracted from the intensity profile. In the subsequent Rietveld refinements allowance was made for a residual background described by a Legendre function with fitted coefficients. The reflection profiles were refined using the Thompson-Cox-Hastings version of the pseudo-Voigt function [32]. The values used for the coherent nuclear scattering lengths of Pd and ^{11}B were $b_{\text{Pd}} = 5.91 \cdot 10^{-12}$ cm and $b_{\text{B}} = 6.65 \cdot 10^{-12}$ cm, respectively [27]. The crystal structure model used for refinement is based on the *fcc* Pd host lattice with the boron atoms statistically distributed over the octahedral interstices (Table 2.1). This yields the following formula for the structure factor of the *hkl* reflection, allowed by the *fcc* Bravais lattice, $F(hkl)$:

$$F(hkl) = 4 \cdot \left[b_{\text{Pd}} \cdot T_{\text{Pd}}(hkl) + (-1)^{(h+k+l)} y \cdot b_{\text{B}} T_{\text{B}}(hkl) \right] \quad (2.4)$$

where T_{Pd} and T_{B} are the overall Debye-Waller factors for palladium and boron which contain contributions from both dynamic and static displacements.

Adopting a Gaussian distribution for the atomic displacements, T_{Pd} and T_{B} can be expressed as [33]

$$T_{\text{Pd,B}}(hkl) = \exp \left[-8\pi^2 \frac{\sin^2 \theta_{hkl}}{\lambda^2} \langle u_{\text{Pd,B}}^2 \rangle \right] \quad (2.5)$$

with $\langle u_{\text{Pd,B}}^2 \rangle$ being the atomic displacement parameter of the respective atom containing in principle both static and dynamic contributions. Separate refinement of the atomic displacement parameters of the boron atoms was not done for the samples of low boron content since the influence of their values on the diffraction patterns is very small for these samples. Therefore, the boron displacements $\langle u_{\text{B}}^2 \rangle$ were determined for the alloy with the highest boron content, $\text{PdB}_{0.184}$, by a first Rietveld refinement applied to the diffraction data recorded at both 15 K and 300 K. The thus resulting values for $\langle u_{\text{B}}^2 \rangle$ were used as fixed values for the alloys of all boron contents in the final Rietveld refinements.

A little, but diffraction detectable, diamond impurity was present in the powders (cf. section 2.3.2.), originating from the rasp used for filing. The presence of this diamond impurity was accounted for by multiphase refinements. Peak profile parameters of the impurity phase were taken equal to those of the PdB_y reflections, because of insufficient intensity for their separate refinement (cf. Figure 2.1) and because the peak profile shape was largely determined by the instrumental broadening.

Table 2.1. Structural models used for the Rietveld refinement on the basis of the neutron diffraction patterns

Atom, Wyckoff label	Fractional coordinates	Atomic displacement parameter	Site occupancy factor
PdB _y , $Fm\bar{3}m$			
Pd, $4a$	0 0 0	$\langle u_{\text{Pd}}^2(y) \rangle$	1
B, $4b$	1/2 1/2 1/2	$\langle u_{\text{B}}^2 \rangle^a$	y^b
Diamond, $Fd\bar{3}m$			
C, $8a$	1/8 1/8 1/8	$\langle u_{\text{C}}^2 \rangle$	1

^a Fixed for all PdB_y compositions to the displacements of boron in the PdB_{0.184} sample at the corresponding temperature (see text).

^b Calculated from the lattice parameter as determined by X-ray diffraction and application of Eq. (2.1)

2.3. Results

2.3.1. X-ray diffraction experiments

The lattice parameters for the four different samples used for neutron diffraction analysis, as determined by X-ray diffraction analysis, are shown in Table 2.2. These lattice parameters were used to determine the PdB_y compositions by application of Eq. (2.1). These compositions were adopted in the following to identify the samples and were used as known data in the Rietveld refinements.

Table 2.2. Lattice parameters as determined after filing the whole reguli by X-ray diffraction (XRD) measurements at room temperature (RT) and by neutron diffraction measurements (ND) at 15 K and 300 K

Composition for weighing	Lattice parameter XRD data at RT (Å)	Calculated composition using Eq. (2.1)	Lattice parameter ND data at 300 K (Å) ^a	Lattice parameter ND data at 15 K (Å) ^a
Pd	3.8910(1)	-	3.8898	3.8804
PdB _{0.05}	3.9264(1)	PdB _{0.050}	3.9252	3.9163
PdB _{0.10}	3.9608(1)	PdB _{0.100}	3.9598	3.9509
PdB _{0.20}	4.0186(1)	PdB _{0.184} ^b	4.0173	4.0090

^a Standard deviations by Rietveld refinements have not been listed here. The numerical values are <0.0001 Å, disregarding uncertainties in the neutron wavelength.

^b For this sample arc melting had to be repeated due to inhomogeneities in the bulk. This resulted for this sample in an overall loss of boron, cf. weighted and calculated boron content.

2.3.2. Rietveld refinement of neutron diffraction data

The relative intensities of the reflections in the neutron diffraction patterns agreed well with the expectation on the basis of Eqs. (2.4) and (2.5), thereby confirming that the boron atoms are located in all cases on the interstitial octahedral sites of the Pd *fcc* arrangement. No superstructure reflections due to a possible long-range ordering of boron atoms were observed. The site occupancies of the boron atoms were imposed on the basis of the value of y obtained from the lattice parameter determined by X-ray diffraction and application of Eq. (2.1); refinements of the occupancy of the B site did not lead to significantly different values for y . A Rietveld fit of the neutron diffraction pattern recorded for PdB_{0.184} at 300 K is shown in Figure 1. The amount of diamond impurity in this powder caused by the filing (cf. section 2.2.1. and section 2.2.4.) is well below 1 mass %. The other samples contained similar amounts of diamond impurity.

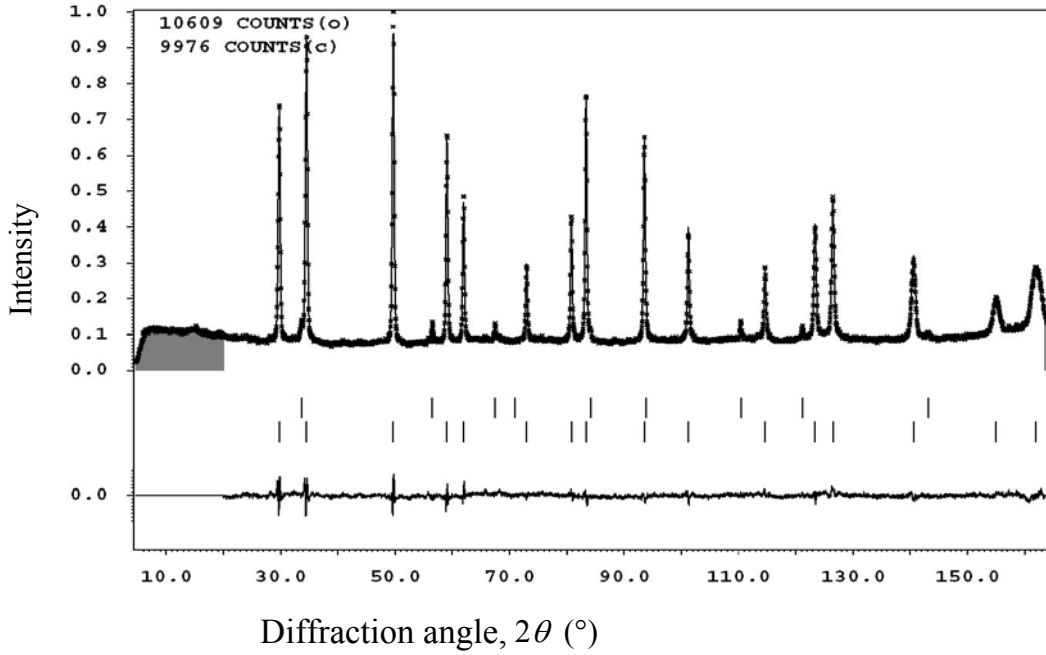


Fig 2.1. Rietveld fit of a neutron diffraction pattern of the $\text{PdB}_{0.184}$ sample measured at 300 K: Measured data points, calculated pattern (full line); difference curve as well as reflection markers (upper line: diamond, lower line: $\text{PdB}_{0.184}$). The shaded regions were excluded from the refinement. The intensity of 1 corresponds to 10609 counts (Residual values (see Ref. [34] for definitions): $R_p = 3.86$; $R_{wp} = 4.82$; $R_{Bragg} = 1.09$).

The atomic displacement parameters determined for Pd in PdB_y and pure Pd, as resulting from the Rietveld refinements, have been listed in Table 2.3. The atomic displacements for pure Pd, $\langle u_{\text{Pd}}^2(0) \rangle$, are close to previously published values [35] for both temperatures. Evidently, the atomic displacements parameters $\langle u_{\text{Pd}}^2(y) \rangle$ determined for the PdB_y alloys are significantly larger than those for pure Pd.

The atomic displacement parameters $\langle u_{\text{Pd}}^2(y) \rangle$ of pure Pd are only caused by dynamic contributions from lattice vibrations. For the PdB_y alloys an additional contribution from static displacements is expected for the Pd atoms. If for PdB_y the dynamic contribution to $\langle u_{\text{Pd}}^2(y) \rangle$ equals $\langle u_{\text{Pd}}^2(0) \rangle$ at the same temperature, the static atomic displacement parameter $\langle u_{\text{Pd}}^2(y) \rangle_{\text{st}}$ is obtained according to

$$\langle u_{\text{Pd}}^2(y) \rangle_{\text{st}} = \langle u_{\text{Pd}}^2(y) \rangle - \langle u_{\text{Pd}}^2(0) \rangle \quad (2.6)$$

thereby implicitly assuming that both the static and the dynamic contributions obey a Gaussian distribution.

For each composition the static displacement parameters thus calculated at 15 K and 300 K agree well, as should be expected (cf. Table 2.3); the values at 300 K are only slightly higher. This supports the above adopted treatment.

Table 2.3. Values of the mean square atomic displacements for the Pd atoms, $\langle u_{\text{Pd}}^2(0) \rangle$ and $\langle u_{\text{Pd}}^2(y) \rangle$, obtained from Rietveld refinements and the static displacement parameters $\langle u_{\text{Pd}}^2(y) \rangle_{\text{st}}$ calculated from these data according to Eq. (2.6).

y according to PdB _{y}	$\langle u_{\text{Pd}}^2(y) \rangle$ at 15 K (Å ²)	$\langle u_{\text{Pd}}^2(y) \rangle$ at 300 K (Å ²)	$\langle u_{\text{Pd}}^2(y) \rangle_{\text{st}}$ at 15 K (Å ²)	$\langle u_{\text{Pd}}^2(y) \rangle_{\text{st}}$ at 300 K (Å ²)
0	0.00092(7)	0.00511(7)	0	0
0.050 ^a	0.00325(8)	0.00767(8)	0.0023(1)	0.0026(1)
0.100 ^a	0.00343(8)	0.00785(8)	0.0025(1)	0.0027(1)
0.184 ^a	0.00292(7)	0.00749(8)	0.0020(1)	0.0024(1)

^a $\langle u_{\text{B}}^2 \rangle = 0.0071 \text{ \AA}^2$ at 15 K and $\langle u_{\text{B}}^2 \rangle = 0.0124 \text{ \AA}^2$ at 300 K as determined in the course of the separate refinement of the PdB_{0.184} data (see section 2.2.4.).

2.4. Discussion

2.4.1. Comparison with EXAFS experiments

EXAFS measurements of PdB_{0.114} and PdB_{0.160}, with reference to pure Pd, were evaluated [8] in terms of local interatomic Pd-Pd distances (1st, 3rd and 4th ‘shell’ of Pd around a reference Pd atom⁵) as well as Gaussian smearing expressed in terms of the ‘EXAFS Debye-Waller factor’ σ_{Pd} , which has the dimension of length, and can be conceived as more or less an analogue of $\langle u_{\text{Pd}}^2 \rangle^{\frac{1}{2}}$ rather than of T_{Pd} (cf. Eq. (2.4)). $\sigma_{\text{Pd},i}^2(y)$ (i designates the shell number) of the PdB _{y} alloys, due to dynamic and static displacements, was related to the corresponding

⁵ The 2nd shell contribution to the EXAFS signal could not be evaluated quantitatively because it is corrupted by the boron atoms acting as ‘lens’ atoms [9].

value of pure palladium, $\sigma_{\text{Pd},i}^2(0)$, assumed to be of purely dynamic nature, by the static contribution $\delta\sigma_{\text{Pd},i}^2(y)$ (cf. Eq. (2.6)):

$$\sigma_{\text{Pd},i}^2(y) = \sigma_{\text{Pd},i}^2(0) + \delta\sigma_{\text{Pd},i}^2(y) \quad (2.7)$$

For the first shell, which corresponds to an average Pd-Pd distance of $a/2^{1/2}$, the pair distribution function $g_1(r)$, with r as the Pd-Pd distance, was found to be largely bimodal; two Pd-Pd distances with high frequency occurred, which both are only marginally smeared by small values of $\delta\sigma_{\text{Pd},i}^2$. The longer Pd-Pd distance was interpreted as an elongated Pd-Pd pair which forms an edge of an *occupied* Pd₆ octahedron, while the shorter Pd-Pd distance was interpreted as an Pd-Pd pair which forms an edge of an *empty* Pd₆ octahedron. These discrete Pd-Pd pair distances are not easily translated into root mean square atomic displacement parameters as observed by diffraction experiments.

For the 3rd and 4th shell the pair distributions $g_3(r)$ and $g_4(r)$ could not be decomposed into different contributions. They each showed only one maximum at a Pd-Pd distance of $(3/2)^{1/2}a$ and $2^{1/2}a$, respectively, which were smeared by significant static displacements $\delta\sigma_{\text{Pd},3}^2$ and $\delta\sigma_{\text{Pd},4}^2$, respectively, because of the different possibilities to place one or more boron interstitials along the Pd-Pd distance concerned.

For large interatomic distances (i.e. for high shell numbers) and thereby minimising the influence of short-range order, the displacement parameters $\sigma_{\text{Pd},i}^2$ used to fit EXAFS data [8] can be related to the atomic displacement parameter $\langle u_{\text{Pd}}^2 \rangle$ according to Ref. [36]

$$\sigma_{\text{Pd},i \rightarrow \infty}^2 = 2\langle u_{\text{Pd}}^2(y) \rangle \quad (2.8a)$$

and thus for the static displacements

$$\delta\sigma_{\text{Pd},i \rightarrow \infty}^2 = 2\langle u_{\text{Pd}}^2(y) \rangle_{\text{st}} \quad (2.8b)$$

Eq. (2.8b) can be used to compare the $\delta\sigma_{\text{Pd},3}^2$ - and $\delta\sigma_{\text{Pd},4}^2$ -values of the 3rd and 4th shells (cf. Eq. (2.7)) with $\langle u_{\text{Pd}}^2(y) \rangle_{\text{st}}$. Thus, from the $\delta\sigma_{\text{Pd},3}^2$ - and $\delta\sigma_{\text{Pd},4}^2$ -values in Ref. [8],

one obtains $\langle u_{\text{Pd}}^2(y) \rangle_{\text{st}}$ -values of 0.0019 \AA^2 and 0.0025 \AA^2 for $\text{PdB}_{0.114}$ and 0.0014 \AA^2 and 0.0019 \AA^2 for $\text{PdB}_{0.160}$. It can be concluded that, even recognising the limited range of evaluated i , the EXAFS data of Ref. [8] give estimates for the static displacements of Pd which are of the same order of magnitude as those obtained directly in this study on the basis of neutron diffraction data (cf. Table 2.3).

2.4.2. Comparison with theoretical predictions and with experimental observations of static displacements in defect-NaCl type transition metal nitrides and carbides

Different approaches exist for the prediction of the static displacements in *fcc* based interstitial solid solutions as a function of concentration [13, 37]. If short-range order is absent and if a Gaussian distribution of the displacements is assumed, the different approaches give expressions like Eq. (2.2) in case of sufficiently small static displacements. Calculations of static displacements on the basis of micromechanical models for *fcc* based interstitial solid solutions (employing the elastic constants of pure Pd and the concentration dependence of the lattice parameters as given by Eq. (2.1)) [13] and consideration of the consequences of these displacements for diffraction [13] yield an explicit version of Eq. (2.2) for PdB_y [A. Udyansky, V. N. Bugaev, unpublished]:

$$\langle u_{\text{Pd}}^2(y) \rangle_{\text{st}} = 0.113 \text{ \AA} \cdot y \cdot (1 - y) \quad (2.9)$$

Values of $\langle u_{\text{Pd}}^2(y) \rangle_{\text{st}}$ according to Eq. (2.9) are shown for the relevant range of y in Figure 2.2 in comparison with the present experimental values (Table 2.3). The disagreement is obvious: PdB_y shows neither the expected concentration dependence of $\langle u_{\text{Pd}}^2(y) \rangle_{\text{st}}$, nor do the static displacement values have the large magnitude as expected from theory. A reason may be that chemical (electronic) interactions may modify the static displacements, recognising that Eq. (2.9) is based on purely elastic interactions. Indeed there are hints that chemical interactions are quite important as suggested by the high solubility of boron in palladium and the lattice parameter change upon boron dissolution [11]. Furthermore, it was shown, that the electronic structure of the palladium, which changes considerably upon

dissolving boron, has an important influence on the thermodynamic properties of the solid solution [4].

There is a lack of static atomic displacement data for other metal rich *fcc* based interstitial solid solutions as a function of the interstitial content. According to Refs. [13, 38, 39] the models leading to Eq. (2.2) should also apply to non-stoichiometric defect NaCl-type intermediate solid solutions $\text{MX}_{1-y'}$, for which M is an early transition metal (groups IVb and Vb) having an *fcc* arrangement and X is N, C on octahedral sites. Here, the state of reference is not the pure *fcc* type metal but the defect free NaCl type solid MX_1 (i.e. $y' = 0$). Upon raising y' , vacancies are introduced on the initially fully occupied octahedral interstitial sites. These vacancies play the same role as the interstitials on the metal rich side (e.g. PdB_y). Experimental data for static displacements in $\text{MX}_{1-y'}$ are available for several systems [38], but for one and the same system the values given in the literature may vary considerably, as for $\text{TiC}_{1-y'}$ [40, 41]. These data have been plotted in Figure 2.2. For most of the systems concerned the static displacements are considerably larger than for PdB_y ; the values show more or less an increase of $\langle u_M^2 \rangle_{\text{st}}$ with increasing y' for $y' < 0.5$.

It is difficult to give reasonable values for the volume size factors for some of the $\text{MX}_{1-y'}$ systems considered in Fig 2.2, except for $\text{ThC}_{1-y'}$, $\text{ZrN}_{1-y'}$ and $\text{TiN}_{1-y'}$, because the volume size factors vary considerably with y [42, 43]. Average values for the range $0 \leq y' \leq 0.2$ have also been given in Figure 2.2. The volume size factor should play an important role for the magnitude of the static displacements of the metal atoms according to Eq. (2.2), but this is not apparent from the data compiled in Figure 2.2. The largest value for the volume size factor occurs for PdB_y , which is according to Eq. (2.1) and Eq. (2.3) given by:

$$\Omega_{\text{sf}}(\text{PdB}_y) = 3 \frac{\alpha}{a_0} \approx 0.53$$

The second largest volume size factor occurs for $\text{VC}_{1-y'}$ (0.12). Yet, for both PdB_y and $\text{VC}_{1-y'}$, the observed static displacements are, by far, not the largest ones (cf. Figure 2.2). If, according to Eq. (2.2), the volume size factor dominates the magnitude of the static displacements, then values of $\langle u_M^2(y) \rangle_{\text{st}} / \Omega_{\text{sf}}^2$ should be similar for the different systems. Clearly such behaviour does not occur.

Hence, the observed static displacements of the metal atoms in *fcc* based interstitial solid solutions do not comply with Eq. (2.2) regarding the dependencies on (a) concentration (especially for PdB_y) and (b) the volume size factor. This contrasts with several examples of substitutional solid solutions which obey Eq. (2.2), e.g. see Ref. [15]. It is unclear why the approximations used to derive Eq. (2.2) are apparently less well justified for interstitial than for substitutional *fcc* based solid solutions. An explanation might be that occurrence of short-range order and the influence of other than microelastic interaction has a more important impact on the static atomic displacements of interstitial solid solutions than on those of substitutional solid solutions.

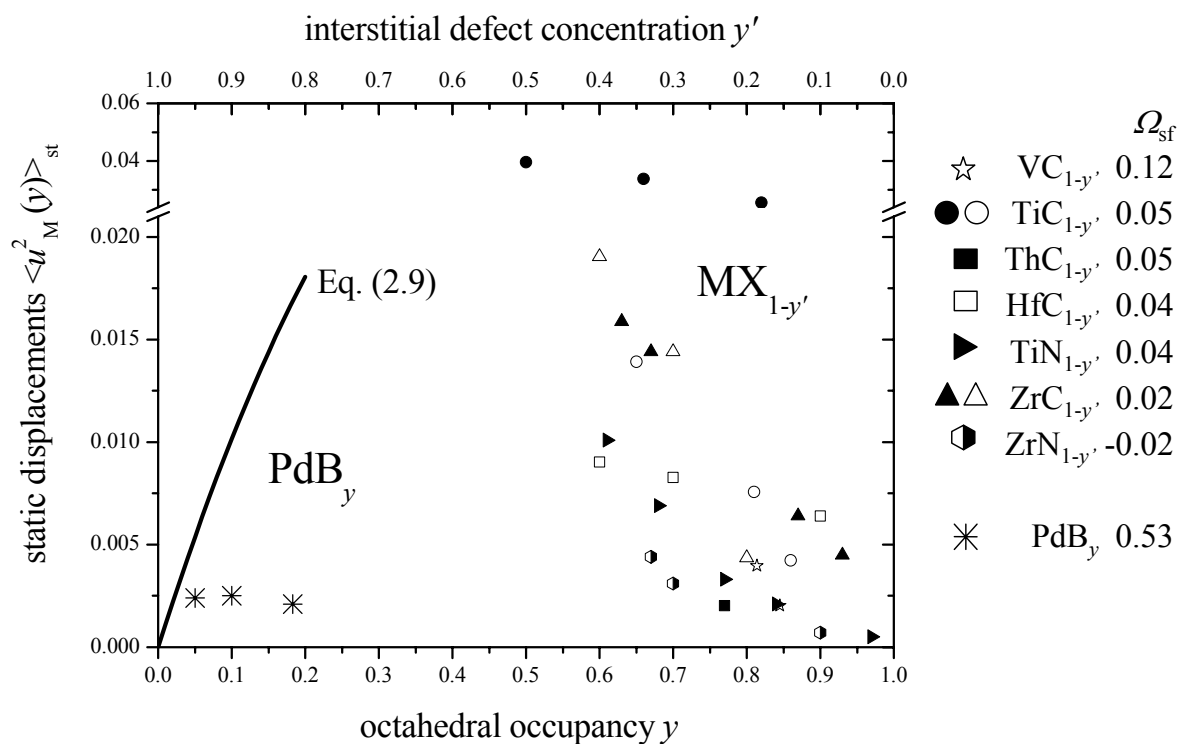


Fig 2.2. Static displacements of the *fcc* arranged M atoms in PdB_y ($M = \text{Pd}$) and in various defect NaCl-type transition metal carbides and nitrides $\text{MX}_{1-y'}$. [38-40, 44]. The volume size factors Ω_{sf} (cf. Eq. (2.2)) for the different compounds have been listed to the right of the figure (calculated from data in Refs. [42, 43, 45]).

2.5. Conclusions

It has been proven for the first time on the basis of diffraction intensity measurements that boron occupies the octahedral interstices in Pd, thus confirming previous results from EXAFS measurements.

Static displacements of Pd in PdB_y could be determined by subtracting the atomic displacement parameter of pure Pd, which can be assumed to be of purely dynamic nature, from the total atomic displacement parameters measured for PdB_y. Indeed, practically similar values were determined for the static displacements in PdB_y at 15 K and 300 K.

The PdB_y alloys show similar values for the static displacements for PdB_{0.050}, PdB_{0.100} and PdB_{0.184}. The results obtained by neutron diffraction analysis agree with those obtained by previous EXAFS measurements.

The results for the static atomic displacements in PdB_y are incompatible with predictions based on elastic interaction of the (misfitting) interstitial atoms and the (metal) atoms of the host lattice.

The observed static displacements of the metal atoms in *interstitial fcc* based solid solutions do not comply with predictions based on purely elastic interactions, in contrast with well documented examples for *substitutional fcc* based solid solutions.

3.

A time-resolved X-ray powder diffraction method to trace the decomposition of PdB_y solid solutions

T. G. Berger, A. Leineweber, E. J. Mittemeijer, M. Knapp

A powder diffraction method is presented for reconstructing probability density functions for the composition, $p(y)$, of a PdB_y solid solution material with composition (y)-dependent lattice parameter from the simultaneous analysis of all reflections in the powder diffraction patterns. The method is applied to the decomposition of a solid solution in a miscibility gap: two ‘boundary phases’ appear which gradually approach but don’t attain fully the compositions of the expected equilibrium phases whereas a significant amount of material with intermediate compositions remains.

3.1. Introduction

X-ray powder diffraction provides information about the atomic structure (size and symmetry of unit cell, atom positions and displacements) of crystalline materials via the positions (Bragg angles) and intensities of reflections. Analysis of the width and shape of diffraction-line profiles, furthermore, allows extraction of microstructural information, e.g. in terms of microstrain and crystallite size [46]. Analysis of this *physical broadening*, denoted f , is, however, considerably hindered by the instrumental contribution g , with which f is convoluted leading to the real measured profile h . Various convolution and deconvolution methods exist to determine the physical from the measured profile [47]. The present work aims at developing a method to reconstruct complicated *probability density functions* for composition, $p(y)$, of a solid solution material, with composition (y)-dependent lattice parameters, from the simultaneous analysis of *all* reflections in the powder pattern.

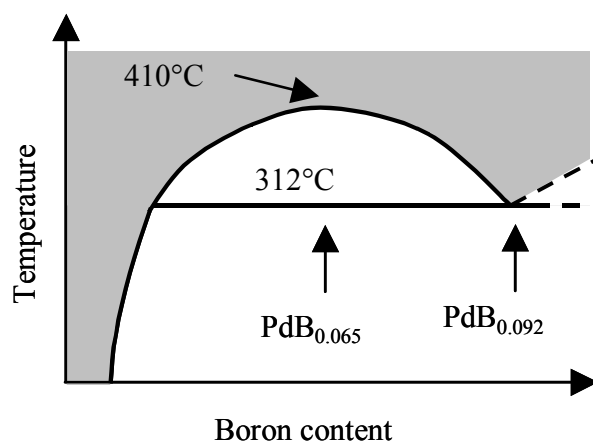


Figure 3.1. Part of the Pd-B phase diagram with the miscibility gap [22]. The grey shaded area shows the phase field of the solid solution.

The solid solution considered here is the palladium-rich solid solution PdB _{y} . It exhibits an extraordinarily high interstitial solid solubility up to about PdB_{0.25} above temperatures of 440°C (y in PdB _{y} denotes both the atomic ratio and the occupancy by boron atoms of the octahedral sites in the *ccp* palladium host lattice) as well as several low-temperature phases and two-phase fields below temperatures of about 400-450°C [22]. A remarkable and for binary interstitial solid solutions rare feature is the miscibility gap with a critical temperature of $T_{\text{crit}} = 410^\circ\text{C}$ which covers at the monotectic temperature of $T_{\text{mono}} = 312^\circ\text{C}$ a composition range of about $0.03 < y < 0.10$ (figure 3.1) [5, 48].

Decomposition in this miscibility gap upon annealing can be considered as a redistribution of boron atoms over the octahedral interstices leading to changes in the composition distribution function $p(y)$ as averaged over the sample, which shows up in a characteristic way in powder diffraction patterns.

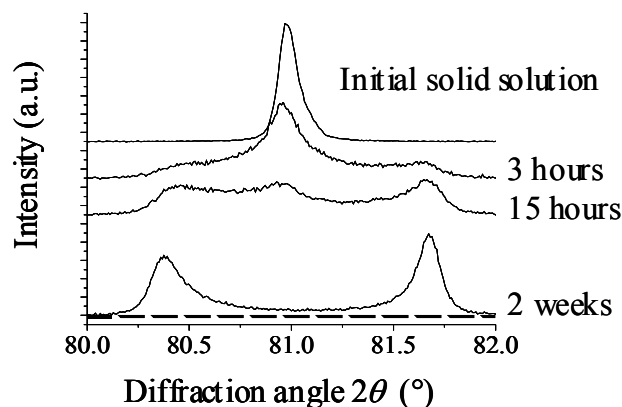


Figure 3.2. 311-Diffraction peak group ($\text{CuK}\alpha_1$ radiation) recorded from a $\text{PdB}_{0.064}$ sample annealed for various times at 340°C .

3.2. Experimental

3.2.1. Preparation and heat treatment

$\text{PdB}_{0.064}$ was prepared by arc melting under argon from weighted amounts of palladium foils and an appropriate amount of boron pieces. $\text{PdB}_{0.050}$, previously used in a neutron diffraction study, was prepared similarly from ^{11}B [14]. Both reguli were checked for homogeneity [11, 14, 48].

The powder samples (filed from the reguli) were sealed under vacuum in quartz capsules, annealed at 800°C for 5 min and subsequently quenched in water. The annealing was performed to relieve deformation stresses due to the filing procedure. The composition was calculated [11] by

$$a = a_0 + \alpha \cdot y = 3.8920 + 0.6882y \text{ [\AA]}. \quad (3.1)$$

The heat treatments for the decomposition were performed from 3 hours till up to 8 weeks (in sealed quartz tubes encapsulated in a salt bath for up to 4 days, longer annealings in a furnace) at 340°C or 355°C with subsequent water quenching.

3.2.2. X-ray diffraction measurements

X-ray powder diffraction measurements of the initial, stress-relieved solid solution and of the subsequently annealed samples were performed

- *in house* on a Philips X'Pert MPD instrument (CuK α_1 radiation in Bragg-Brentano geometry, powder samples were deposited as a thin layer together with internal silicon standard powder on Si wafers cut parallel to the (510) plane) and
- for two selected PdB_{0.064} specimen, one quenched from 800°C to preserve the solid solution and one annealed for 18 days at 340°C to evoke the decomposed state, employing synchrotron radiation with $\lambda = 1.1315 \text{ \AA}$ on the B2 beamline [49], HASYLAB, Hamburg (no internal standard, separate LaB₆ standard (SRM 660a) measurements; powder deposited on Kapton foil, measurements performed in transmission geometry).

All reflections were recorded by measuring over 2θ (diffraction-angle) subranges sufficiently large to determine the background at both sides of each reflection (group).

3.3. Data evaluation method

The decomposition of the initially homogeneous solid solution into a boron-rich and a boron-poor solid solution phase is clearly revealed by the occurring splitting of the Bragg reflections. For short annealing times (e.g. figure 3.2), the original solid solution is still present. Even after the longest applied heat-treatment times (8 weeks at 340°C and 2 weeks at 355°C), still considerable diffraction-line broadening remains which is asymmetric for both the high and the low boron components ('boundary phases') such that residual intensity between the pairs of reflections remains. To analyse the time-dependent decomposition as observed in the X-ray diffraction patterns, the reflection profiles were modelled using the program TOPAS [50] as described below.

3.3.1. X-ray data evaluation

For each heat treatment, all individually measured reflections, from PdB_y, as well as from the internal standard (*in house* data), were merged into one data set after manually subtracting the background. This complete pattern was modelled in a Rietveld-like fashion, considering a convolution of three line-broadening contributions:

$$h = g \otimes f_1 \otimes f_2, \quad (3.2)$$

with g and f_1 taken as *Voigt* functions with angle-dependent Gaussian and Lorentzian full width at half maximum values B_L and B_G , respectively. The instrumental profile g was determined from the internal Si standard (*in house* data) or the separately measured LaB₆ standard (*synchrotron* data), respectively, by fitting LY , LX , GU , GV , GW according to:

$$\begin{aligned} g: \quad B_{g,L} &= LY \tan \theta + LX / \cos \theta ; \\ B_{g,G}^2 &= GU \tan^2 \theta + GV \tan \theta + GW . \end{aligned} \quad (3.3)$$

The structural line broadening f_1 of the two quenched solid solution samples was described semi-empirically by size and anisotropic microstrain broadening, fitting L_1 , L_2 , S_1 , S_2 , G_2 :

$$\begin{aligned} f_1: \quad B_{f_1,L} &= L_1 \tan \theta + L_2 / \cos \theta ; \\ B_{f_1,G}^2 &= \left(S_1 + S_2 \frac{h^2 k^2 + k^2 l^2 + h^2 l^2}{(h^2 + k^2 + l^2)^2} \right) \tan^2 \theta + (G_2 / \cos \theta)^2 . \end{aligned} \quad (3.4)$$

The present description of the microstrain broadening anisotropy was derived from the assumption of an isotropic microstress distribution leading to anisotropic microstrain if the crystals are elastically anisotropic [51] (as is the case for Pd).

The additional line broadening occurring in the diffraction patterns of the annealed specimen, f_2 , can be attributed to the occurrence of decomposition-induced compositional variations described by $p(y)$, starting from a delta-shaped distribution for the initial solid solution. For the annealed samples $p(y)$ was approximated by a frequency polygon (figure 3.3) with composition steps of $\Delta y = 0.001$. Due to the composition dependence of the lattice

parameters of the cubic crystal lattice (equation (1)) of PdB_y , $p(y)$ reflects itself directly in each reflection [52]. In Topas [50] this was incorporated in terms of a multiphase refinement of 120 ‘phases’ with composition values y' which are spaced by Δy . Each ‘phase’ $\text{PdB}_{y'}$ has been ascribed a compositional line broadening contribution corresponding to a trapezoid (shaded in grey in figure 3.3) with a width of $2\alpha\Delta y \tan\theta/a$ (cf. equation (3.1)), and an area (integral intensity) proportional to $(p(y') + p(y' + \Delta y))/2$.

3.3.2. Penalty functions to achieve stability in refinements of $p(y)$

Refining the $p(y')$ values without any constraints leads to severe correlations between different $p(y')$ [53, 54]. These correlations can be reduced to achieve physically realistic ‘smooth’ $p(y)$ by application of so-called penalty functions (PF). These serve as contribution to the overall χ_{pen}^2 (*penalised least squares*), additional to the usual χ^2 from the difference between observed and the calculated profile [55]:

$$\chi_{pen}^2 = \chi^2 + (K \cdot PF)^2; \quad K: \quad \text{penalty weighting factor [50].} \quad (3.5)$$

Commonly [53, 54], these penalty functions are modified integrals of the first or second derivatives of $p(y)$, e.g. as used here:

$$PF_1 = \int q_1 \cdot (p'(y))^2 dy; \quad q_1: \quad p^{-1}(y); \quad (3.6)$$

$$PF_2 = \int q_2 \cdot (p''(y))^2 dy; \quad q_2: \quad (C^2 + (p''(y))^2)^{-1}. \quad (3.7)$$

A compromise for the weight K of the penalty function contribution to the overall χ^2 must be found to obtain a reasonable $p(y)$: In case of too low weight the correlations are not sufficiently suppressed; in case of a too high weight, physical features in the shape of $p(y)$ may be suppressed (*oversmoothing*) [54]. In the present case, the application of the penalty function was allowed to increase the χ^2 value by not more than 10% as compared to the value obtained with an unconstrained refinement. For most of the performed refinements, PF_1

produced satisfactory results; PF_2 (with another constant C to be adjusted empirically) was only used for the refinement of the microstrain broadening change (see Results).

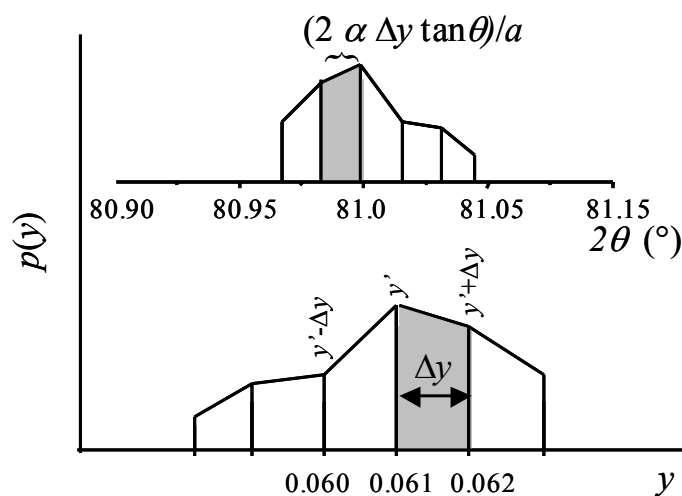


Figure 3.3. Frequency polygon type description of the probability density function of composition $p(y)$ and the corresponding line-broadening f_2 for the 311-reflection. The grey area shows the contribution associated with composition $y=0.061$ (with an area proportional to $(p(y') + p(y'+\Delta y))/2$).

3.4. Results and Discussion

Results for $p(y)$ obtained with the described method are shown in figures 4a-c for $\text{PdB}_{0.064}$ and $\text{PdB}_{0.050}$ annealed for various times at 340°C and $\text{PdB}_{0.050}$ annealed for various times at 355°C .

Initially, $p(y)$ contains a remaining contribution from the original solid solution. Its phase fraction was determined by subtracting an estimated parabolic ‘background $p(y)$ ’ between the two ‘boundary phases’ (figure 4a). The time-dependence of the molar phase fraction (referring to the formula PdB_y) of the parent solid solution is similar for the three samples, but the $\text{PdB}_{0.064}$ sample decomposes much faster than the $\text{PdB}_{0.050}$ at the same temperature of 340°C . Further, $\text{PdB}_{0.050}$ decomposes faster at 340°C than at 355°C (figure 3.5). Therefore the driving force for the decomposition has its maximum in the middle of the miscibility gap.

The values of the boundary (product) phase compositions (figure 3.6) were determined by a parabolic fit to the three locally highest $p(y')$ values in the range of the local maxima pertaining to the high and low boron product phases. For short annealing times the $p(y)$ of the $\text{PdB}_{0.050}$ sample, annealed at 355°C , did not show clear local maxima for the ‘boundary phases’, therefore the two shortest annealing times were omitted. For long

annealing times, differences in the ‘boundary phase’ composition for the same temperature occur, which is incompatible with the phase diagram (cf. figure 3.6).

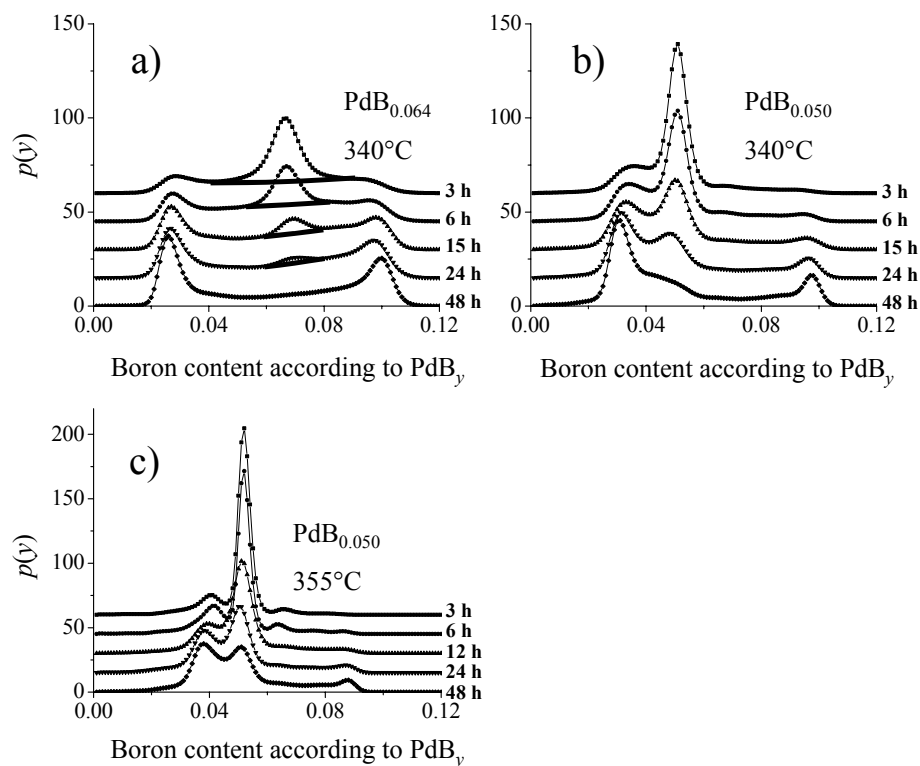


Figure 3.4a-c. $p(y)$ for different times and different initial compositions. Clearly visible is the faster decomposition at 340°C for (a) $\text{PdB}_{0.064}$ compared to (b) $\text{PdB}_{0.050}$. For $\text{PdB}_{0.050}$ the decomposition is faster at (b) 340°C compared to (c) 355°C (estimation of the fraction of initial solid solution has been indicated in 3.4a).

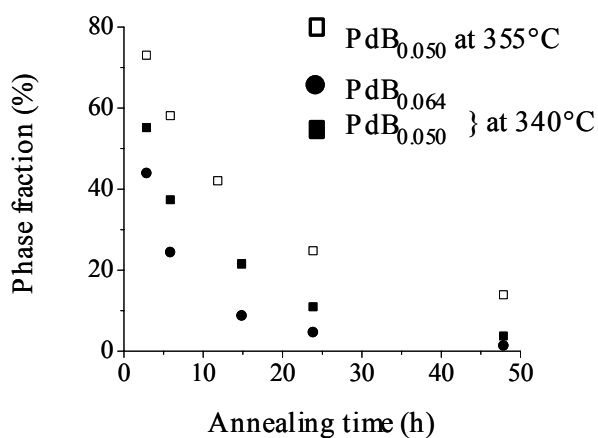


Figure 3.5. Relative phase fractions of the initial solid solutions vs. annealing time.

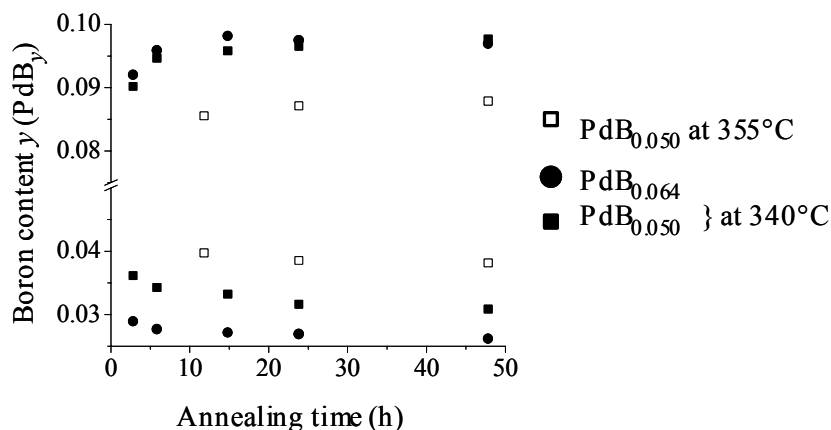


Figure 3.6. Boundary product phase compositions vs. annealing time. For Pd_B0.050 at 355°C the shorter annealing times could not be analysed (see text).

So far in the analysis the line profile parameters of the microstructural line-broadening, f_1 , were kept constant and taken equal to those determined for the initial solid solution. Since the mechanical microstrain broadening is anisotropic (cf. equation (3.4)), it should be possible to detect a change in f_1 upon decomposition, given sufficient resolution of the data, as it was the case for the *synchrotron* measurements. Unconstrained refinement of S_1 and S_2 (equation (3.4)) was not possible due to the correlation of the S_1 parameter with the also $\tan\theta$ -dependent line broadening due to $p(y)$. Therefore the ratio S_1/S_2 was fixed to the value of the initial solid solution. By stepwise increasing S_1 and S_2 it could be shown that there is indeed an increase of microstrain broadening upon decomposition. The first derivative as used in PF_1 has its highest values at the inflection points of $p(y)$ located at the ‘flanks’ of $p(y)$, thus the penalty function may suppress subtle width-related effects. Therefore, for the analysis of S_1 and S_2 , the penalty function PF_2 was employed which has its highest values at the maxima of $p(y)$.

The resulting $p(y)$ are shown in figure 3.7 for the initial solid solution values of S_1 and S_2 characterising the anisotropic microstrain broadening and for 5 S_1 and 5 S_2 ; in the last case a distinctly improved fit to the measured diffraction pattern was achieved. It follows that changes in S_1 and S_2 influence $p(y)$: broader f_1 due to higher values of S_1 and S_2 leads to a ‘sharpened’ $p(y)$ (figure 3.7).

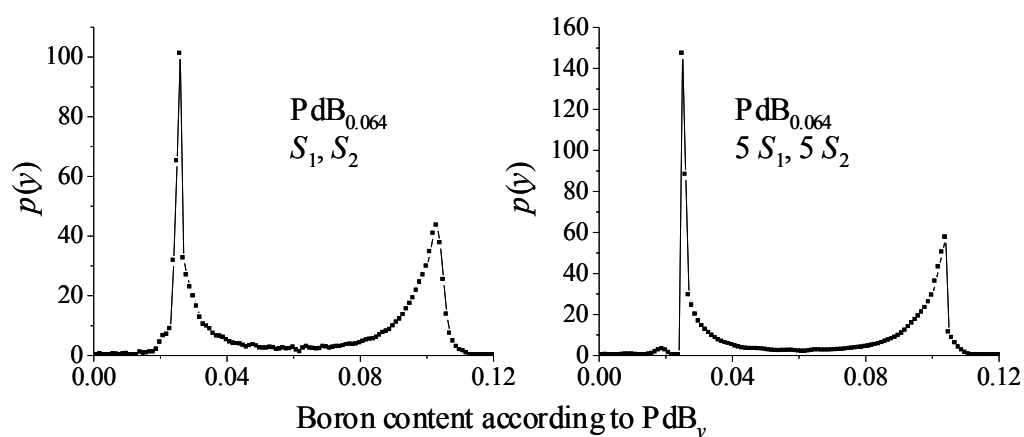


Figure 3.7. $p(y)$ as determined from synchrotron data adopting microstrain broadening parameters S_1 and S_2 equal to those of the solid solution (left) and 5 times as large (right) (PF_2 applied).

3.5. Conclusions

A method has been presented to determine presuppositionlessly composition distributions of decomposing solid solutions from complicated diffraction-line profile shapes in an simultaneous evaluation of all reflections in a powder diffraction pattern. This composition distribution is determined by convolution fitting of a probability density function $p(y)$ with an instrumental broadening contribution g measured from an internal standard and a microstrain and size broadening contribution measured from a parent solid solution sample.

4.

On the formation and crystal structure of the Pd₆B phase

T. G. Berger, A. Leineweber, E. J. Mittemeijer, C. Sarbu, V. Duppel, P. Fischer

The crystal structure of the Pd₆B phase has been elucidated employing selected area electron diffraction and X-ray and neutron powder diffraction methods. It is based on a cubic close packed arrangement of Pd with B occupying 1/6 of the octahedral sites in an ordered way, such that a monoclinic (*C2/c*) superstructure results. The crystal structure contains isolated [BPd₆] octahedral entities providing large distances between nearest neighbour boron atoms. Depending on the way of preparation, the Pd₆B phase can occur for the same composition in two different manifestations having considerably different lattice parameters, which has a microstructural background. Various phase equilibria between the ordered Pd₆B phase and the disordered interstitial solid solution of boron in cubic close packed palladium have been investigated to clarify the corresponding regions in the phase diagram Pd-B.

4.1. Introduction

The terminal interstitial solid solution of boron in palladium, Pd[B], is a remarkable model system for the study of the character of metallic interstitial phases [56]. In metallic interstitial phases a relatively rigid metal partial structure exists exhibiting usually a dense arrangement of the metal atoms (cubic close packed, hexagonal close packed or body centred cubic), which serves as a host for light non-metal atoms (usually H, B, C, N, O) which occupy octahedral or tetrahedral interstices, the so-called interstitial sites. Band-structure calculations indicate the presence of both metal-metal and metal-non-metal bonding interactions. In the crystal structure of Pd[B] the B atoms occupy octahedral interstitial sites of a cubic close packed (*ccp*) partial structure of Pd atoms [8, 11, 14] in a disordered fashion, such that both the Pd sites and the octahedral sites form *fcc* type arrays. According to Hägg's rule of critical atomic radius, B should actually be too large to fit into the octahedral interstices of the *ccp* arrangement of Pd atoms [11]. Yet, the maximum interstitial solubility above about 450°C in Pd[B] has been reported to correspond to an atomic fraction of ~ 20 at. % B [22]. In the sequel the *atomic ratio* y will be used to quantify the composition of the solid solution (and for the ordered phases derived from it) in the form of the formula PdB _{y} (e.g. PdB_{0.25} for ~ 20 at. % B); y also corresponds to the average occupancy of the octahedral sites. Except for very low B contents, the solid solution is only stable at elevated temperatures, but it can be retained by quenching.

A typical low-temperature phenomenon of solid solutions in which certain partial structures are occupied by different types of species (different types of atoms, or atoms and vacancies) is the occurrence of long-range ordering in one or several partial structures (usually accompanied by the reduction of translational symmetry and thus by the occurrence of *superstructure* reflections which are absent for the disordered phase) or decomposition. For the solid solution PdB _{y} ordering of y B vs. $(1 - y)$ vacancies can occur on the *fcc* type array of octahedral sites (often referred to as the "*fcc* sublattice" of octahedral sites).

The low-temperature region of the Pd-B phase diagram in the composition range Pd-PdB_{0.25} appears to consist of low-temperature phases and several two-phase regions; the literature is contradictory, but since X-ray powder diffraction patterns of the low temperature phases are always dominated by the typical '*fcc*-type pattern' of *fundamental reflections*, which are already observed for the solid solution, it is generally accepted that the metallic partial structure of the parent solid solution with the *ccp* arrangement of Pd atoms is largely retained as the mean crystal structure of the low-temperature phases.

One single low temperature phase was reported in Ref. [5] (Figure 4.1a), having the assigned composition PdB_{0.188} ('Pd₁₆B₃'). The X-ray powder diffraction patterns showed no splitting of the fundamental reflections, which would hint at (but which would not be required for) a symmetry lower than cubic. Observed superstructure reflections were ascribed to a not specified B ordering on the octahedral sites and were indexable (with integral indices) according to a face-centred cubic superstructure cell with $a' = 2a_{fcc}$, where a_{fcc} denotes the lattice parameter of the *fcc* parent solid solution. With respect to the parent a_{fcc} cell these superstructure reflections are indexable as $\frac{h}{2} \frac{k}{2} \frac{l}{2} fcc$ with odd h, k, l . For similar compositions (PdB_{0.18}-PdB_{0.20}) a low-temperature phase Pd₅B was reported to form from the solid solution upon annealing below of 380°C [12]; XRD patterns were similar to those of the solid solution and no additional superstructure reflections were detected, but observed splitting of fundamental reflections was interpreted in terms of a slightly tetragonally distorted variant of the solid solution phase having a face-centred tetragonal (*fmt*) unit cell with $a_{fmt}, c_{fmt} \approx a_{fcc}$ and $c_{fmt} < a_{fmt}$.

A phase diagram for the system Pd-B published in Ref. [10] (Figure 4.1b) showed two different low-temperature phases: "Pd₆B" which would form congruently from the solid solution at 440°C and "Pd₅B" which would form peritectically from the solid solution at 372°C; further crystallographic information was not given.

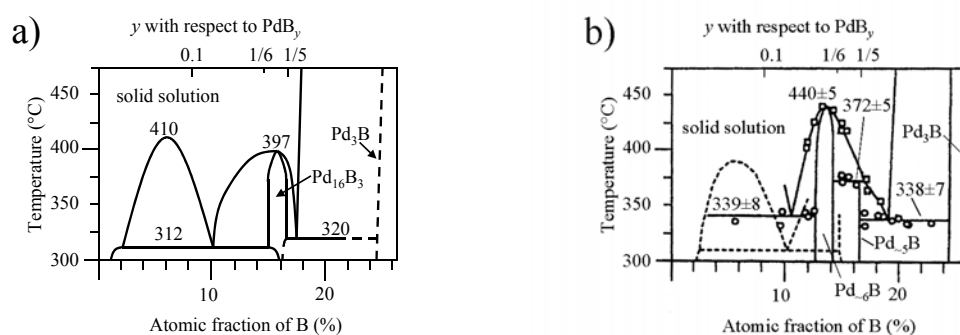


Fig. 4.1. Phase diagrams for the Pd-B system as proposed in Ref. [5] (a) and Ref. [10] (b).

In none of the mentioned previous works about the low temperature phases of the solid solution PdB_y [5, 10, 12] the way B is distributed on the *fcc* type array formed by the octahedral sites was indicated. Ordering of different species (different types of atoms or vacancies and atoms) within a partial structure formed by an *fcc*-type array of sites has been observed for various types of phases (e.g. Table 4.1) [57]: The most elementary case of this

type of ordering concerns ordering in substitutional closed packed cubic $M_yM'_{1-y}$ with M and M' being different metals; e.g. see the classical system Au-Cu [58]. The PdB_y alloys are interstitial alloys in which the ordering partial structure (i.e. the octahedral sites) is embedded in a host partial structure of metal (Pd) atoms with *ccp* arrangement, which is usually fully occupied by one type of atoms, so that ordering cannot occur on this partial structure. Thus, PdB_y can be compared with many interstitial transition metal nitrides and carbides, $MX_y\Box_{1-y}$ (M : transition metal, X : C, N, less frequently O; \Box : vacancy on ordering partial structure). In contrast with PdB_y, most representatives of these phases are known for relatively large values of y : $0.5 \leq y \leq 1$; they are often referred to as defect-NaCl (rock salt) type interstitial phases. Furthermore, there are many, basically ionic (sometimes with some additional metallic bonding for low-valent transition metals) metal chalcogenides ($X = \text{O, S, ...}$) and halides ($X = \text{F, Cl, ...}$), $M_yM'_{y'}\Box_{1-y-y'}X$ which are derived from the rock salt structure: a complete close packed cubic partial structure of chalcogenide/halide anions, X , with the *fcc* type array of the octahedral sites being occupied by different types of cations (M, M') or cations and vacancies (\Box); examples are anatase-type $\text{Ti}\Box\text{O}_2$ [59], $\text{Sc}_2\Box\text{S}_3$ [60], $\text{U}\Box_4\text{Cl}_5$ [61] (i.e. $y = 0$), LiFeO_2 and Li_5ReO_6 [62] (i.e. $y + y' = 1$; cf. Table 4.1).

The crystal structures of all phases mentioned above, exhibiting rather different chemical bonding character, attract interest because the ordering type chosen by nature out of an infinite number of possibilities reflects the nature of the interaction and the magnitude of the interaction energies between the ordering species, and thus the type of ordering provides profound insight into the thermodynamics of the system considered. Hence, investigations of, in particular, such systems for which the state of order varies as a function of temperature and/or composition, e.g. by order-disorder phase transitions, can be rewarding scientifically. Usually the atomic interactions leading to the observed state of order are expressed in terms of pair-interaction energies between the different species (atom types and vacancies) on the ordering partial structure. On the basis of such pair-interaction energies it is possible to calculate 'ordering phase diagrams' if additionally models for the configurational entropy are adopted, e.g. in a Gorsky-Bragg-Williams approach [63] or by employing the cluster variation method [64, 65].

The interatomic interactions determining the state of order are of various types. For *metallic* interstitial or substitutional solid solutions the interactions are often subdivided into strain-induced interactions (mainly due to size of the atoms leading to local distortions in the crystal structure) and into so-called chemical interactions [13]. For *ionic* phases usually

Coulomb approaches (Madelung energy) are applied, together with polarisation and strain (size) effects [66, 67].

In the following the crystal structure of the ordered low-temperature phase Pd₆B as determined in this work by electron, X-ray and neutron diffraction analyses will be presented. Furthermore, the existence of different two-phase equilibria of Pd₆B with a disordered PdB_y solid solution will be established, leading to specification of the Pd₆B phase field in the Pd-B phase diagram. In this work the formula Pd₆B will be used for this phase irrespective of the actual, experimentally determined composition of this phase in a specific specimen used in an experiment, which is specified by *y* in the formula PdB_y, likewise applied also for the solid solution.

Table 4.1. Types of phases with crystal structures showing (long-range) ordering of two types of species (metal atoms *M* or *M'*, non-metal atoms *X*, or vacancies □) on a *fcc* type array of sites.

Compound class	example	species on ordering <i>fcc</i> type array	species on additional, non-ordering <i>fcc</i> type array
<i>ccp</i> based solid solution $M_yM'_{1-y}$	Cu ₃ Au	25% Cu 75% Au	-
interstitial <i>ccp</i> based solid solution $MX_y□_{1-y}$	Pd ₆ B	16.7% B 83.3% □	Pd
defect-NaCl type nitrides, carbides, $MX_{1-y}□_y$	V ₆ C ₅	16.7% □ 83.3% C	V
ionic $M_y□_{1-y}X$	UCl ₅ ^a	20% U 80% □	Cl
ionic $M_yM'_{1-y}X$	LiFeO ₂	50% Li 50% Fe	O

^a Disordered state unknown

4.2. Possible ordering patterns for B in Pd₆B

The determination of the crystal structure of the ordered Pd₆B (ideal composition: $y = 1/6$ with respect to PdB_{*y*}) phase on the basis of selected area electron diffraction patterns (cf. section 4.4.2.) was facilitated by a successful conjecture of three main candidate structure types. Good guesses can be made by looking at already known ordered phases like those discussed in the introduction (see also Table 4.1) in which the two species (say *X* and *Y*) on the ordering *fcc* type array of sites occur in a 1:5 ratio, i.e. with compositions $X_{1/6}Y_{5/6}$ or $X_{5/6}Y_{1/6}$. Considering first the crystal structures of interstitial phases with the formula $MX_{1/6}Y_{5/6} = MX_{1/6}\square_{5/6}$ as candidate structures for Pd₆B (= PdB_{1/6}\square_{5/6}), no example was found in literature. However, the crystal structures of the interstitial phases with the formula $MX_{1/6}Y_{5/6} = M\square_{1/6}Y_{5/6}$ may also be candidate structures for Pd₆B, i.e. the roles of interstitial atom *X* and vacancy \square are exchanged. This implies that analogous types of ordering can occur for MX_y with $y = 1/2 + \delta$ and $y = 1/2 - \delta$.}

Ordered defect-NaCl type interstitial phases of the type $MY_{5/6}\square_{1/6}$ are known for interstitial transition metal carbides ($M = V, Nb; Y = C$): $MY_{5/6}$ or M_6C_5 . Three different, closely related superstructure types have been described for these carbides [68], in terms of idealised atomic coordinates (including those of the empty octahedral sites) and in terms of the basis vectors of the superlattices, as follows:

1. trigonal, space group $P3_1$, $\mathbf{a}_{tr} = 1/2[2\bar{1}\bar{1}]_{fcc}$, $\mathbf{b}_{tr} = 1/2[\bar{1}12]_{fcc}$, $\mathbf{c}_{tr} = 2[\bar{1}\bar{1}1]_{fcc}$,
 $V_{tr} = 4.5V_{fcc}$
2. monoclinic, space group $C2$, $\mathbf{a}'_{m1} = 1/2[\bar{1}\bar{1}\bar{2}]_{fcc}$, $\mathbf{b}'_{m1} = 3/2[110]_{fcc}$, $\mathbf{c}'_{m1} = [\bar{1}\bar{1}2]_{fcc}$,
 $V_{m1} = 6V_{fcc}$, $\beta'_{m1} = \arccos(-1/3) = 109.47^\circ$
3. monoclinic, space group $C2/m$, $\mathbf{a}_{m2} = 1/2[\bar{1}\bar{1}\bar{2}]_{fcc}$, $\mathbf{b}_{m2} = 3/2[110]_{fcc}$,
 $\mathbf{c}_{m2} = 1/2[\bar{1}\bar{1}\bar{2}]_{fcc}$, $V_{m2} = 3V_{fcc}$, $\beta_{m2} = \arccos(-1/3) = 109.47^\circ$

However, the space groups of the superstructures of types 1 and 2 have to be revised. According to Refs. [69, 70] the actual symmetry of type 1 is $P3_112$ (or $P3_212$) rather than $P3_1$ ($P3_2$). Furthermore, structures which exhibit the same ordering patterns of species on an ordering *fcc* type array of sites like that one occurring for type 2 were discussed (i) in the course of considerations on the hypothetical cation ordering in ionic NaCl derivative crystal structures (e.g. structure candidates for Li₅ReO₆ [62]), and (ii) in the course of a systematic derivation of possible crystal structures for octahedral molecules MX_6 which adopt an *fcc*

type array of X [71]. In these works the structures were conceived to be centrosymmetric ($C2/c$ rather than $C2$), suggesting that this is also the case for the corresponding M_6C_5 superstructure of type 2. Moreover, a basis transformation can be applied in order to bring the monoclinic angle β of the type 2 superstructure closer to 90° [62, 71]. The thus resulting idealised superlattice basis vectors and the atomic coordinates for the three candidate structure types for Pd₆B have been listed in Table 4.2 (superstructure of type 2) and in the Appendix (superstructures of types 1 and 3).

It should be noted here that all three ordering types give rise to superstructure reflections indexable as $\frac{h}{2} \frac{k}{2} \frac{l}{2} fcc$ with odd h, k, l with respect to the fcc unit cell of the solid solution (the indices with respect to the different supercells vary from type to type) [68, 72]. Such superstructure reflections have been observed previously for 'Pd₁₆B₃' [5]. However, in Ref. [5] a *cubic* $a' = 2a_{fcc}$ supercell⁶ was proposed with unspecified ordering pattern for B. Additional to these superstructure reflections common to the three superstructure types, further superstructure reflections occur in different ways for the three superstructure types, which should allow distinction between the three superstructure types. However, distinction of superstructure types 1 and 3 on the basis of powder diffraction patterns only may not be straightforward [72].

Table 4.2. Idealised structure parameters for the type 2 superstructure candidate for Pd₆B: space group $C2/c$: $\mathbf{a}_{m1} = 1/2[1\bar{1}\bar{2}]_{fcc}$ ($a_{m1} = \sqrt{6}/2 a_{fcc}$), $\mathbf{b}_{m1} = 3/2[\bar{1}\bar{1}0]_{fcc}$ ($b_{m1} = 3\sqrt{2}/2 a_{fcc}$), $\mathbf{c}_{m1} = 1/2[\bar{3}\bar{3}\bar{2}]_{fcc}$ ($c_{m1} = \sqrt{22}/2 a_{fcc}$), $V_{m1} = 6V_{fcc}$, $\beta_{m1} = \arccos(-1/\sqrt{33}) = 100.03^\circ$.

Atom	Wyckoff site	x_{id}	y_{id}	z_{id}
B	$4e$	0	1/12	1/4
Pd1	$8f$	1/8	1/4	1/8
Pd2	$8f$	1/8	7/12	1/8
Pd3	$8f$	1/8	11/12	1/8

⁶ This supercell structure proposal is reasonable because no splitting of the fundamental reflections was observed which would hint at a crystal system of lower symmetry than cubic. See further results obtained in the present work.

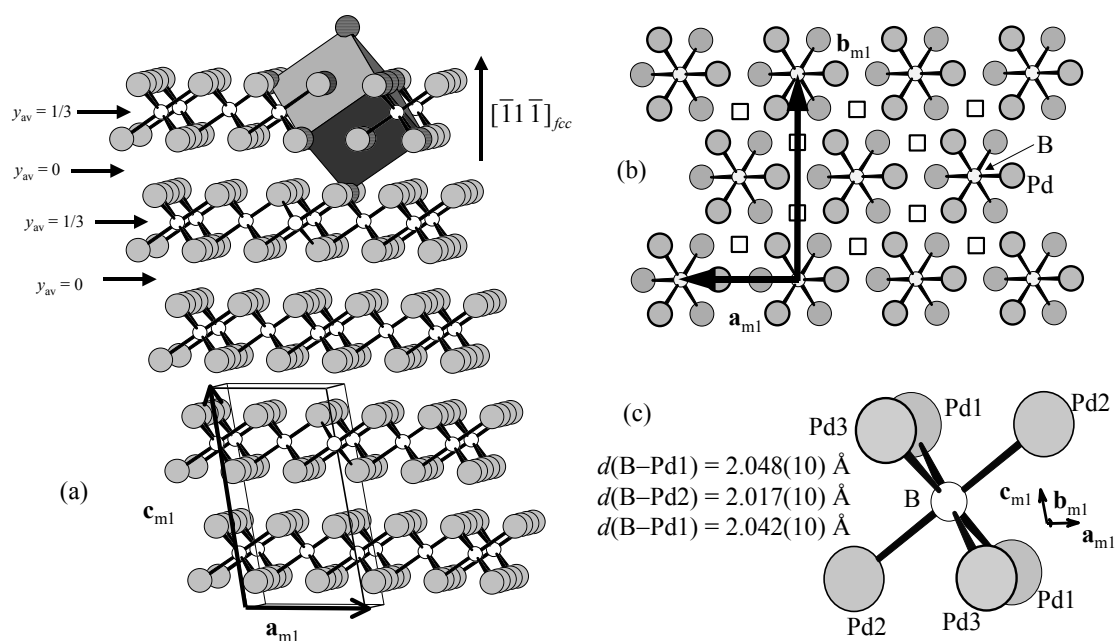


Fig. 4.2. Crystal structure of *pseudocubic* Pd₆B (space group *C2/c*) as obtained by Rietveld refinement of NPD data: (a) view along $[\bar{1}\bar{1}0]$; alternate sequence of layers of octahedral interstitial sites (looked upon ‘edge on’) within the cubic close packed arrangement of Pd with average occupancies for B of $y_{av} = 1/3$ and 0. The stacking direction corresponds to $[\bar{1}\bar{1}1]_{fcc}$ (see Table 2). One *fcc* unit cell has been highlighted in the upper part of the figure, and one monoclinic unit cell at the bottom. (b) view along $[\bar{1}\bar{1}1]_{fcc}$; arrangement of B atoms with the surrounding Pd atoms within one of the occupied octahedral layers, vacant octahedral sites within this layer are indicated by squares, \square . (c) One BPd₆ entity with shortest distances B-Pd.

4.3. Experimental

4.3.1. Preparation of the Pd-B alloys

The three PdB_y alloys investigated in this study were prepared from weighted amounts of about 3.5 g and about 1.5 g Pd foils (Heraeus, 99.9 wt.%), for the neutron and X-ray diffraction measurements, respectively, and an appropriate amount of B pieces (isotope enriched boron: Eagle Picher, 99.29% ¹¹B, chemical purity 99.97 wt.%; or B with isotopes in natural abundance: Johnson Matthey, chemical purity 99.5 wt.%) by arc melting under argon (550 hPa; Messer Griesheim, 99.999 vol.%). For an overview of the prepared alloys, see Table 4.3. For alloy 2 intended for neutron diffraction measurements the pure isotope ¹¹B was used instead of B with the natural mixture of its isotopes (about 20 at.% ¹⁰B), because ¹⁰B has

an extremely high neutron absorption cross section [27] and by its use the diffracted neutron beam intensities would decrease dramatically.

The homogeneity of the reguli and their compositions was checked by measuring the cubic lattice parameters by X-ray diffraction (XRD; cf. section 4.3.3.). The compositions were calculated by application of [11]:

$$a = 3.8920 \text{ \AA} + 0.6882 \text{ \AA} y \quad (4.1)$$

In the following the actual compositions, described by PdB_y, are used to identify the alloys used in the experiments (Table 4.3).

For the homogeneity measurements, small parts of the as-cast bulk samples were removed by filing from the top and bottom of the reguli using a diamond rasp⁷. The filings were sealed under vacuum in quartz capsules, annealed at 1073 K for 5 min and subsequently quenched in water. The heat treatment was performed in order to relieve deformation stresses due to the filing procedure. If homogeneity had not been achieved, the corresponding regulus was remelted and the X-ray test procedure was repeated. The samples listed in Table 4.3 contain apparently a little less B than corresponding to the composition aimed at; experience with the preparation of other Pd-B alloys has suggested that some B loss can happen during the arc beam melting.

For the structural and thermal analyses, heat treated powder and pieces of bulk specimen were prepared starting from the homogeneous reguli. The powder specimens (for XRD) were obtained by filing the reguli as described above for the homogeneity verification, and bulk pieces (for transmission electron microscopy, TEM and differential thermal calorimetry, DSC) were cut from the reguli by electrical discharge machining. The thus obtained powder filing batches and bulk pieces were encapsulated in evacuated quartz tubes and stress relieved at 1073 K for 5 min followed by quenching (including, for the bulk pieces, immediate subsequent crushing of the quartz tubes to obtain a higher cooling rate). For further heat treatments at lower temperatures, leading to the ordered and/or two-phase states (see sections 4.4.2. and 4.4.3.), filings and bulk pieces were re-encapsulated (as above) and again quenched (and crushed for the bulk pieces) after annealing.

⁷ The filing with the diamond rasp introduced diamond as an impurity phase as exhibited by corresponding reflections in diffraction patterns, as particularly visible in the neutron diffraction patterns.

For the neutron diffraction measurements a larger amount of powder than for the XRD measurements was required. To this end, the homogeneous regulus was filed entirely. The resulting powder (ca. 2.5 g) was encapsulated under helium (at about 500 hPa; Westfalen Reinstgase, 99.999 vol.%) in a quartz tube, stress relieved and water quenched. The He atmosphere (instead of vacuum) was chosen in order to achieve a fast cooling rate for the relatively large batch size.

Table 4.3. Overview of prepared Pd-B alloys, measured cubic lattice parameters by X-ray diffraction and calculated compositions (cf. Eq. (4.1)), and techniques applied for (structure and constitution) characterisation (X-ray powder diffraction (XRD), transmission electron microscopy (TEM), neutron powder diffraction (NPD) and differential scanning calorimetry (DSC)).

Alloy no.	Composition from weighing	Lattice parameter XRD ^a data at room temperature (Å)	Calculated composition using Eq. (4.1)	Characterisation technique
1	PdB _{0.150}	3.9913(1)	PdB _{0.144}	XRD, TEM
2	Pd ¹¹ B _{0.163}	4.0010(1)	Pd ¹¹ B _{0.158}	XRD, NPD
3	PdB _{0.177}	4.0040(1)	PdB _{0.163}	DSC, TEM

4.3.2. DSC Measurements

Differential scanning calorimetry (DSC) measurements were carried out using a power compensated Perkin Elmer DSC Pyris-1. The samples in form of one bulk piece of 20-40 mg of Pd-B were put into an open gold pan, whereas the reference pan was empty. A protective gas atmosphere of pure argon was employed. The used heating/cooling rate was 20°C/min. Since only the qualitative thermal behaviour of the samples was of interest here, the DSC measurements were performed without separate precise calibration involving an uncertainty of about +/- 5°C for all temperatures indicated.

4.3.3. X-ray diffraction measurements

X-ray powder diffraction (XRD) patterns were recorded at a Philips X'Pert MPD diffractometer applying Bragg-Brentano geometry and a primary beam monochromator to select the $K\alpha_1$ component of the employed copper radiation (wave length of 1.54056 Å). The samples consisted of a thin layer of the PdB_y alloy powders mixed with silicon powder (with lattice parameter $a = 5.43102$ Å) as internal standard (only used for lattice parameter measurements), deposited onto single crystalline silicon wafers with a (510) plane parallel to the surface.

Since a large amount of powder from the neutron diffraction measurements was available, the solid solution sample Pd¹¹B_{0.158} was prepared for XRD as a 'backloaded' specimen with a thickness of 2 mm and a diameter of 10 mm.

For the homogeneity measurements, all fundamental reflections (i.e. reflections expected from the *fcc* lattice of the solid solution phase) in the range of $25^\circ < 2\theta < 100^\circ$ (i.e. *hkl* from 111_{fcc} to 222_{fcc}) were recorded by measuring over 2θ ranges sufficiently large to determine the background at both sides of each reflection. The reflection positions were obtained by fitting the reflections with symmetrical pseudo-Voigt functions [28, 50]. The thus obtained 2θ values of the PdB_y reflections were corrected using the positions of the Si reflections in the same 2θ range for calibration. The lattice parameters of the PdB_y phase were subsequently determined by using the programme CELREF [29]. Similar procedures were applied for lattice parameter determinations of phases pertaining to more complicated low-temperature states involving occurrence of two-phase mixtures and/or non-cubic phases.

4.3.4. Neutron diffraction measurements

Neutron powder diffraction (NPD) was performed at the HRPT powder diffractometer [30] installed at the spallation neutron source SINQ (Paul Scherrer Institute, Villigen, CH) employing the high-intensity mode of the instrument. The present measurements were conducted in the same way as those presented earlier in Ref. [14]. The wavelength of the neutron beam was $\lambda = 1.1966$ Å. The Pd¹¹B_{0.158} powder was kept in a closed vanadium cylinder ($d = 4$ mm). To avoid frozen air in the vanadium cylinder and thus avoiding bad thermal contact, the powder had been put into the cylinders in a glovebox under helium

atmosphere. The sample was measured for about 8 h at 15 K (using a closed cycle CTI refrigerator). Absorption due to the sample was shown to be negligible; see Ref. [14].

Rietveld refinement on the basis of the NPD data was performed using the programme Jana2000 [31]. A fixed background was estimated from measured intensities at a series of 2θ values in between occurring reflections and subtracted from the intensity profile. In the subsequent Rietveld refinement allowance was made for a residual background described by a Legendre function with fitted coefficients. A possible zero-point shift was refined as well. The reflection profiles were fitted with pseudo-Voigt functions according to the Thompson-Cox-Hastings version [32].

4.3.5. TEM sample preparation

Transmission electron microscopy (TEM) and electron diffraction was performed to investigate the superstructure of the ordered low-temperature phase and microstructural phenomena related with the ordering. Plates with a thickness of a few hundred μm were cut from the arc-beam-melted bulk samples by electrical discharge machining. These plates were cleaned and polished to achieve a thickness of about 100 μm . Subsequently, conventional Ar⁺ ion-milling was performed at an acceleration voltage of 4 kV on a BalTec RES010 instrument for up to 35 h applying an angle of incidence of 6°. If necessary, the samples were additionally thinned at a modified [73] BalTec RES010 for 30 minutes applying a voltage of 1 kV until they were electron transparent. To avoid sample heating during the milling the sample was cooled with liquid nitrogen. The TEM measurements were carried out using JEOL 2000 FX (200 kV), Philips CM 30 (300 kV) and Philips CM 200 (200 kV) transmission electron microscopes.

4.4. Results

4.4.1. Thermal analysis;

phase transition ordered Pd₆B \rightleftharpoons disordered PdB_{1/6}

A bulk piece of PdB_{0.163} was annealed at 800°C for 5 min and subsequently quenched in water by crushing the quartz capsule. In this way the disordered state occurring at high temperature should be retained. Subsequently, in the DSC the sample was heated up to 500°C and cooled down, for three times in succession (Figure 4.3a). Only the first of these DSC cycles showed upon heating an exothermic signal in the range of 100°C to 230°C with the maximum at about 160°C (Figure 4.3b). This is followed by an endothermic signal with an onset temperature for the heating runs of about 440(5)°C (Figure 4.3a). In the following heating runs only the latter signal is observed. In all cooling runs an exothermic signal occurs with onset temperature of about 440(5)°C, i.e. the same temperature at which the endothermic signal occurring in all three heating runs is observed.

The exothermic signal at about 160°C during only the first heating run is ascribed to ordering of the as-quenched disordered alloy, disordered PdB_{0.163} \longrightarrow ordered Pd₆B. The signal at about 440°C observed upon heating and cooling in all cycles is attributed to the reversible order-disorder phase transition, ordered Pd₆B \rightleftharpoons disordered PdB_{0.163}, in agreement with earlier results [10].

It was found that samples which were quenched from 800°C *without* immediate subsequent crushing (see section 4.3.1.), led to absence of the initial exothermic signal at about 160°C upon heating in the first cycle. This implies that crushing is essential to realise efficacious quenching to retain the disordered solid solution state.

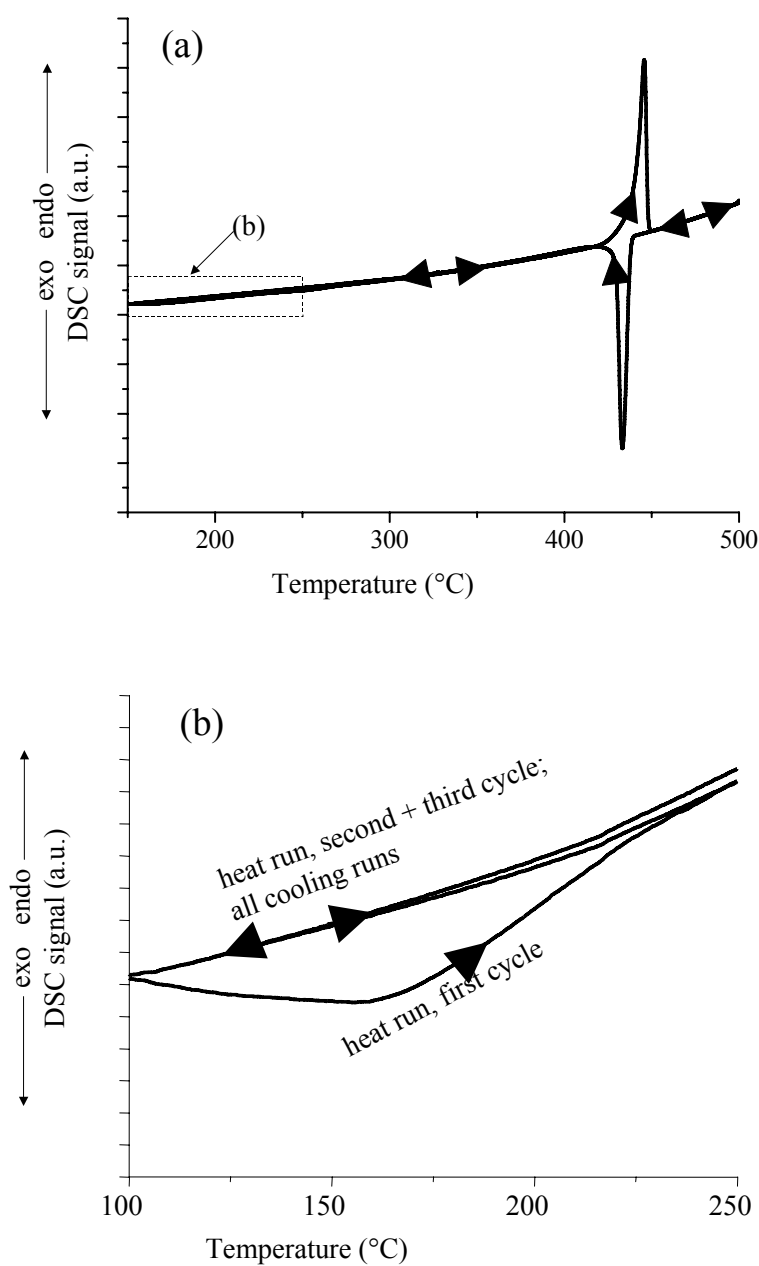


Fig. 4.3. DSC scans recorded from a PdB_{0.163} (alloy 3) bulk piece (after annealing for 5 min at 800°C followed by water quenching thereby retaining the disordered solid solution). During the first heating run the exothermic signal observed at about 160°C (b) indicates the at this temperature irreversible ordering of B atoms leading to Pd₆B. Upon further heating and subsequent cooling, at 440(5)°C the (reversible) transition ordered Pd₆B \rightleftharpoons disordered PdB_{0.163} occurs, in this and in all following heating and cooling cycles (a).

4.4.2. Electron diffraction; type of B ordering in the Pd₆B phase

Electron diffraction patterns recorded from PdB_{0.163} (alloy 3) annealed for 1 week at 360°C showed not only the fundamental reflections pertaining to the mean *fcc*-type arrangement of the Pd atoms but also many reflections ascribed to the occurrence of a superstructure (see Figure 4.4 a): a comparison of the recorded diffraction patterns with diffraction patterns simulated [74] on the basis of the three candidate structures (see section 4.2, Table 4.1 and the Appendix) showed that all observed superstructure reflections can be explained by the exclusive occurrence of type 2 ordering (*C2/c*, Table 4.2); diffraction patterns requiring the (additional) presence of ordering types 1 and 3 not were observed.

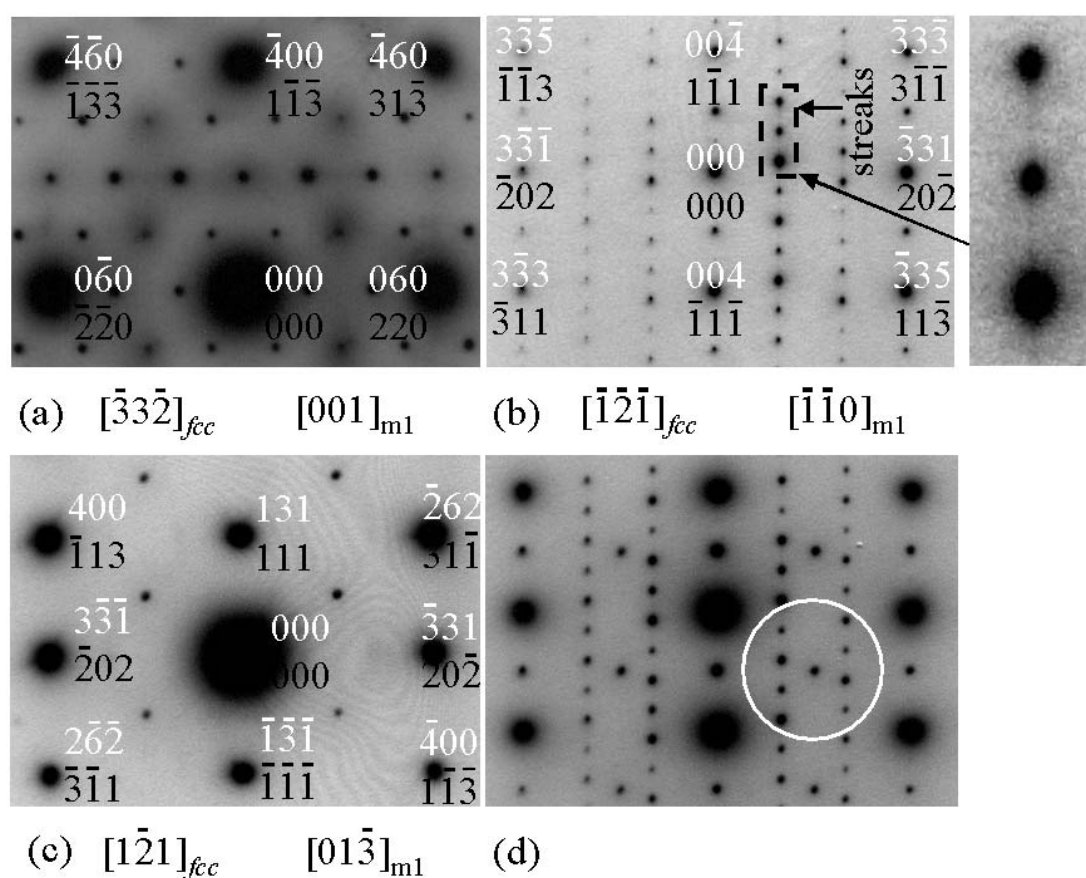


Fig. 4.4. Electron diffraction pattern negatives of a thin foil prepared from (a) PdB_{0.163} (alloy 3) quenched and annealed for 1 week at 360°C and (b-d) PdB_{0.144} (alloy 1) quenched and annealed for 3 weeks at 280°C. The fundamental reflections and zone axes of each pattern except (d) have been indicated according to the *fcc* average structure (white numbers) and to the monoclinic type 2 superstructure (black numbers, see Table 4.2). The directions of the incident electron beams have been indicated; (d) can be understood as a superposition of patterns (b) and (c). Weak streaks parallel to $[\bar{1}\bar{1}]_{fcc}$ hint at faults in the stacking sequence of partially occupied (by B) layers of octahedral interstitial sites of the close packed cubic arrangement of Pd, and have been indicated in the enlarged part of pattern (b). The circle in (d) indicates the (superstructure) reflections used to record the dark-field image in shown Figure 4.5.

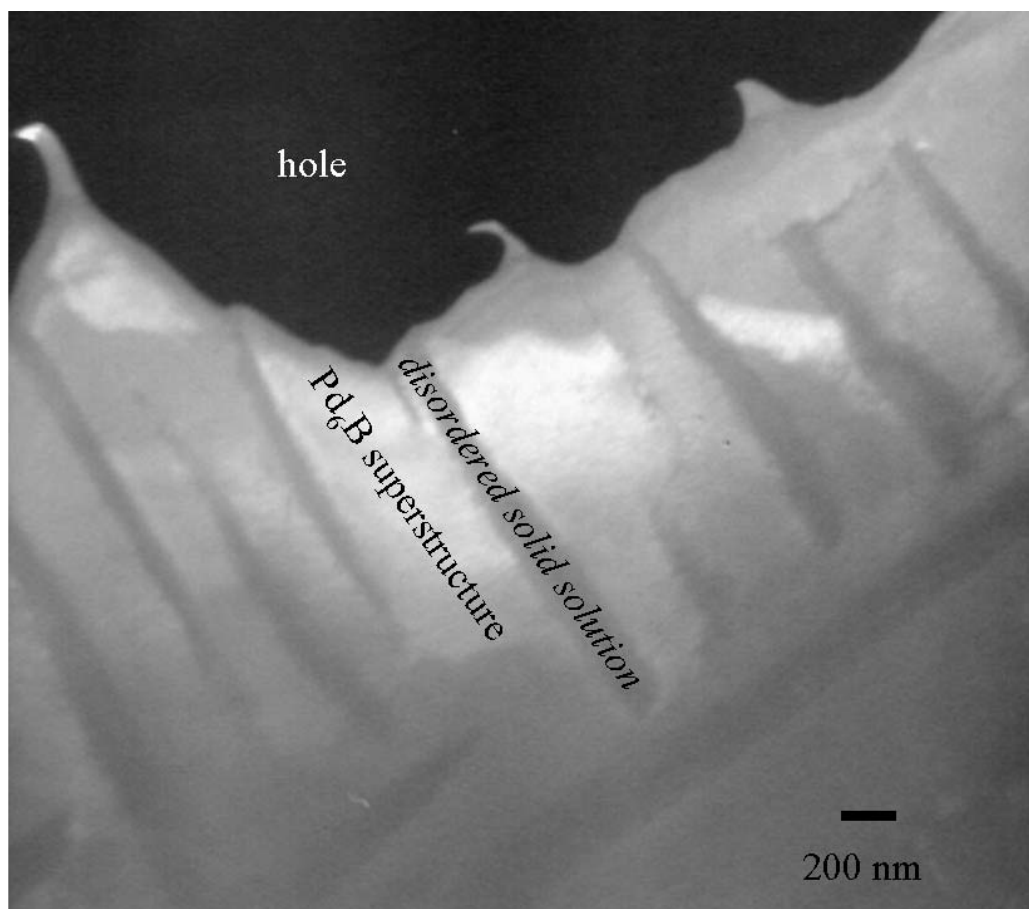


Fig. 4.5. Dark field images (positive) taken using the superstructure reflections of the ordering of type 2 encircled in Figure 4.4d. The plate-like dark regions are the solid solution disordered with respect to B.

Since the *monoclinic* superstructure of type 2 is formed from a *cubic* high temperature phase, different orientations of the superlattice with respect to the *fcc* lattice of the parent high temperature phase are possible, and thus differently oriented domains are expected to occur. Indeed some diffraction patterns were observed which could be explained as superpositions of diffraction patterns from differently oriented (with respect to the incident electron beam) domains, as shown in Figure 4.4d.

Whereas the annealed PdB_{0.163} (alloy 3, a week at 360°C) apparently consists of only one single phase, TEM of the annealed PdB_{0.144} (alloy 1, 3 weeks 280°C followed by quenching) reveals plates of a second phase in a matrix consisting of Pd₆B with the superstructure of type 2 (see Figures 4.4b-d). According to the selected area electron diffraction performed these plates (typical thickness < 100 nm) have – with respect to the fundamental reflections – the same crystallographic orientation as the surrounding matrix, but the superstructure reflections lack. Indeed, the plates appear dark in dark-field images

recorded from the superstructure reflections of the surrounding matrix (Figure 4.5). The superstructure reflections used for the dark field images have been indicated in Figure 4.4d.

Certain diffraction patterns pertaining to $\langle 211 \rangle_{fcc}$ zones showed besides the superstructure reflections corresponding to the type 2 ordering additional diffuse streaks parallel to $[\bar{1}\bar{1}\bar{1}]_{fcc}$ directions in these patterns (Figure 4.4b; see section 4.5). For the monoclinic Pd₆B phase specific directions $[uvw]_{fcc}$ or planes $(hkl)_{fcc}$ are defined according to Table 2.

4.4.3. X-ray powder diffraction; identification of two-phase equilibria

X-ray diffraction measurements on powder samples quenched from the solid solution phase field (i.e. from 800°C) were used to determine the lattice parameters of the *fcc* unit cell of the solid solution. Subsequent application of Eq. (4.1) led to determination of the B contents (cf. Table 4.3).

Inspection of the XRD patterns obtained from the Pd¹¹B_{0.158} (alloy 2) and PdB_{0.163} (alloy 3) powders quenched from 800°C revealed the presence of $\frac{h}{2} \frac{k}{2} \frac{l}{2}_{fcc}$ superstructure reflections with odd h, k, l (Figure 4.6) as reported previously for 'Pd₁₆B₃' [5], and which are also consistent with the *C2/c* (type 2) superstructure (as confirmed for this specimen by NPD, see section 4.4.4.). This indicates that the quenching for these powder samples was not sufficiently drastic; the quenched sample already reveals ordering of B, although splitting of the fundamental reflections does not occur, i.e. the fundamental reflections can be indexed on the basis of a *fcc* lattice with lattice parameter a_{fcc} ; Pd₆B in fact is monoclinic with 'true' lattice parameters which can easily be calculated from a_{fcc} using the relations given in Table 4.2. Thus in the following the present form of the ordered Pd₆B phase is designated as *pseudocubic*.

Upon annealing this batch of quenched Pd¹¹B_{0.158} powder for 70 h at 360°C or for 96 h at 280°C, according to the XRD analysis, decomposition into two apparently – according to the fundamental reflections – face-centred cubic phases occurred: a majority high-B content phase showing the same superstructure reflections as observed already for the sample quenched from 800°C and a minority low-B content phase showing no superstructure reflections. Thus it appears that low-B solid solution has precipitated from the initial ordered Pd₆B phase leading to a slight increase of the B content of the latter (which remains

pseudocubic). Single peak fitting of selected fundamental reflection pairs, of the solid solution phase and of the *pseudocubic* Pd₆B phase (originating from the 111_{fcc} , 200_{fcc} , 220_{fcc} , 311_{fcc} and 222_{fcc} reflections of the sample quenched from 800°C), provided the lattice parameters of the *fcc* unit cells as well as the integrated intensities of the different reflections. The mole fractions of the two phases (referring to formula PdB_y) were then calculated adopting that the mole fractions are proportional with the corresponding integrated intensities⁸. This was done separately for the abovementioned five reflection pairs of the two phases and the averaged results have been given in Table 4.4. The average B content of the samples (PdB_{0.153} for the annealing at 280°C and PdB_{0.152} for the annealing at 360°C), as calculated on the basis of the mole fractions and the B contents of the two phases, is close to the expected value of the alloy Pd¹¹B_{0.158} (Table 4.4).

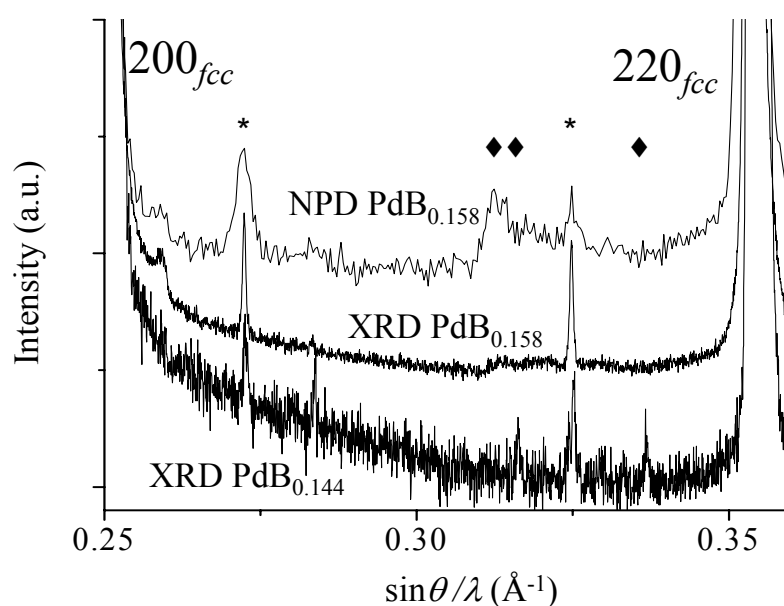


Fig. 4.6. Part of the neutron (NPD) and X-ray powder diffraction (XRD) patterns of Pd¹¹B_{0.158} (quenched from 800°C) and the XRD pattern of PdB_{0.144} (annealed for 70 h at 360°C; see also Figure 4.7), all in the range between the 200_{fcc} and 220_{fcc} reflections. The patterns have been scaled and shifted in order to allow easier comparison of the patterns. The $\frac{h}{2} \frac{k}{2} \frac{l}{2}_{fcc}$ superstructure reflections with odd h , k , l have been indicated by stars (*); further superstructure reflections have been indicated by diamonds (◆).

⁸ This is justified because the unit-cell volumes, the structure factors and the absorption coefficients are very similar for both phases.

The XRD patterns recorded from the PdB_{0.144} powder (alloy 1) showed no superstructure reflections after quenching from 800°C, indicating that the solid solution had been fully retained. Upon annealing for 70 h at 360°C and 70 h at 280°C new weak reflections and splitting of the fundamental reflections occurs. For both annealing temperatures the reflection groups originating from the fundamental reflections of the solid solution can be interpreted in terms of formation of a *fcc* low-B content solid solution phase and an apparently face-centred tetragonal (*fc*t) high-B content phase. The latter shows unsplit fundamental reflections hhh_{fc} (originating from 111_{fcc} and 222_{fcc} of the initial solid solution) and split (doublets) hhl_{fc} and lhh_{fc} of intensity ratio 2:1 or 1:2 (originating from 200_{fcc} , 220_{fcc} , 311_{fcc} , Figure 4.7). For both annealing temperatures the lattice parameter of the cubic low-B content phase (depending on the annealing temperature, see Figure 4.7) largely corresponds to that observed for the disordered low-B content phase that developed upon annealing of Pd¹¹B_{0.158} (see above and Table 4.4). The according to the fundamental reflections face-centred tetragonal high-B content phase has $c_{fc} > a_{fc}$; its B content is estimated on the basis of Eq. (4.1) by substituting the lattice parameter a_{fcc} in Eq. (4.1) by $(a_{fc}^2 \times c_{fc})^{1/3}$. As for the low-B content phase, the resulting B content of the *pseudotetragonal* Pd₆B phase is about equal to the one of the *pseudocubic* Pd₆B phase (with superstructure of type 2) developing upon annealing of Pd¹¹B_{0.158} at the same annealing temperatures (see Table 4.4). TEM analysis of PdB_{0.144} (alloy 1) annealed at 280°C indicated the presence of a two-phase state with a disordered solid solution minority component and an ordered majority component showing type 2 superstructure (see section 4.4.2.). Hence, it is concluded, that the two phases observed by XRD are the same: the *fcc* low-B component is the disordered solid solution, and the apparently face-centred tetragonal component is indeed the (same) monoclinic Pd₆B phase exhibiting now different lattice parameters (*pseudotetragonal* Pd₆B) than the Pd₆B phase produced by annealing PdB_{0.158} (*pseudocubic* Pd₆B). The *pseudotetragonal* unit cell suggested by inspection of the fundamental reflections in the XRD patterns can be related to the monoclinic supercell as described in Table 4.2 by choosing $\mathbf{c}_{fc} = [001]_{fcc}$ ($\mathbf{a}_{fc} = [100]_{fcc}$ and $\mathbf{b}_{fc} = [010]_{fcc}$). The two other alternatives, $\mathbf{c}_{fc} = [100]_{fcc}$ and $\mathbf{c}_{fc} = [010]_{fcc}$, would lead to lattices with lattice parameters incompatible with monoclinic symmetry. In fact, if the monoclinic lattice parameters for a type 2 superstructure (Table 4.2) are calculated on the basis of the *pseudotetragonal* cell parameters and the choice $\mathbf{c}_{fc} = [001]_{fcc}$, the weak reflections observed in the XRD patterns of annealed PdB_{0.144} (alloy 1) can be indexed with respect to this monoclinic cell; most of these superstructure reflections are observed (with the

same Miller indices) in the XRD patterns of the *pseudocubic* Pd₆B phase produced from Pd¹¹B_{0.158} (alloy 2). This confirms that indeed the *pseudotetragonal* Pd₆B produced from PdB_{0.144} (alloy 1) and the *pseudocubic* Pd₆B produced from Pd¹¹B_{0.158} (alloy 2) are different *manifestations* of the same phase (see section 4.5.1.). Furthermore, the superstructures as revealed for alloys 1 and 3 by electron diffraction are also the same as deduced from the corresponding XRD patterns. It follows that the ordered Pd₆B phase forming in all three alloys is the same and of ordering type 2.

Mole fractions of the low- and high-B content components of decomposed PdB_{0.144} (alloy 1) were obtained as described above for PdB_{0.158}. To this end, for the *pseudotetragonal* high-B Pd₆B component the integrated intensities of all reflections originating from a certain hkl_{fcc} were summed up. Again, good agreement between the calculated average B content and the value determined for the initial solid solution was obtained (PdB_{0.140} as calculated for both annealing temperatures vs. the initial boron content of PdB_{0.144}, cf. Table 4.4).

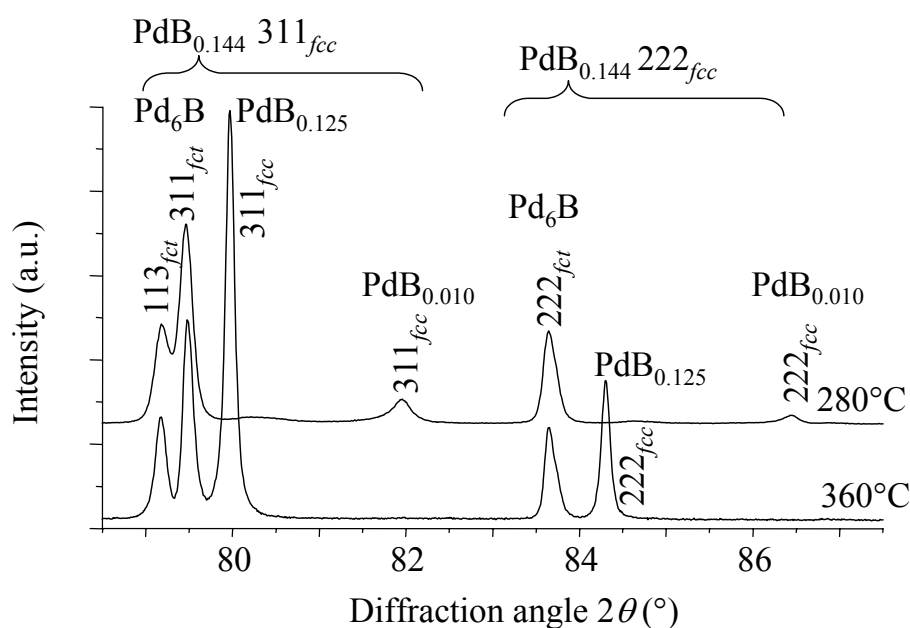


Fig. 4.7. Part of X-ray diffraction patterns of quenched PdB_{0.144} (alloy 1) after annealing for 70 h at 280°C (leading to decomposition into ordered Pd₆B + disordered PdB_{0.010}) and for 70 h at 360°C, (leading to decomposition into ordered Pd₆B + disordered PdB_{0.125}), exhibiting the formation of *pseudotetragonal* (*fct* = face-centred tetragonal) Pd₆B (cf. Table 4.4). The patterns have been scaled and shifted in order to allow easier comparison of the patterns. The braces on the top indicate which of the observed reflections ‘emerge’ from which reflections of the initial PdB_{0.144} solid solution, where the tips indicate the corresponding original reflection positions.

Table 4.4. Lattice parameters (measured by XRD at ambient temperatures) and mole fractions (referring to the formula PdB_y) of the high B component (ordered Pd₆B) and low B component (disordered solid solution) obtained by decomposing PdB_{0.144} (alloy 1) and Pd¹¹B_{0.158} (alloy 2) both at 280°C and 360°C.

Annealing temperature (°C)	Annealing time (h)	Calculated composition of low-B solid phase using Eq. (4.1)	Lattice parameters of Pd ₆ B phase a_{fcc} or a_{fct} , c_{fct} (Å)	Calculated composition using Eq. (4.1)	Mole fraction Pd ₆ B	Calculated average B content y_{av} of the whole sample
starting material Pd ¹¹ B _{0.158} (alloy 2, unsuccessfully quenched from 800°C, see section 4.4.3.)						
280 ^a	96	PdB _{0.008}	$a_{fcc}= 4.0020(1)$ <i>pseudocubic</i>	PdB _{0.160}	0.95(1)	0.153(2)
360	70	PdB _{0.127}	$a_{fcc}= 4.0022(1)$ <i>pseudocubic</i>	PdB _{0.160}	0.75(0)	0.152(0)
starting material PdB _{0.144} (alloy 1, successfully quenched from 800°C, see section 4.4.3.)						
280 ^a	70	PdB _{0.010}	$a_{fct}= 3.9971(2)$ $c_{fct}= 4.0133(3)$ <i>pseudo-tetragonal</i>	PdB _{0.161} ^b	0.86(1)	0.140(4)
360	70	PdB _{0.125}	$a_{fct}= 3.9960(2)$ $c_{fct}= 4.0146(2)$ <i>pseudo-tetragonal</i>	PdB _{0.160} ^b	0.42(1)	0.140(1)

^a A small and broad residual hump in the X-ray powder patterns indicates the presence of some remaining parent solid solution (see Figure 4.7). This is not considered here.

^b For the *pseudotetragonal* Pd₆B phase the cubic root of the unit cell volume is taken as the lattice parameter in Eq. (4.1); see text.

4.4.4. Neutron diffraction; structure parameters of Pd₆B

As compared to the corresponding XRD pattern taken at ambient temperatures, the NPD pattern (Figure 4.6 and 4.8) of the Pd¹¹B_{0.158} sample taken at 15 K⁹ shows much stronger superstructure reflections relative to the intensities of the fundamental reflections: the effect of ordering of B is more pronounced in NPD patterns because the scattering power of B is higher than that of Pd in NPD (as can be expressed in terms of the coherent scattering lengths; see Table 4.5), whereas for XRD the scattering power (expressed in terms of the atomic form factors, or basically in terms of the number of electrons) is much smaller for B than for Pd.

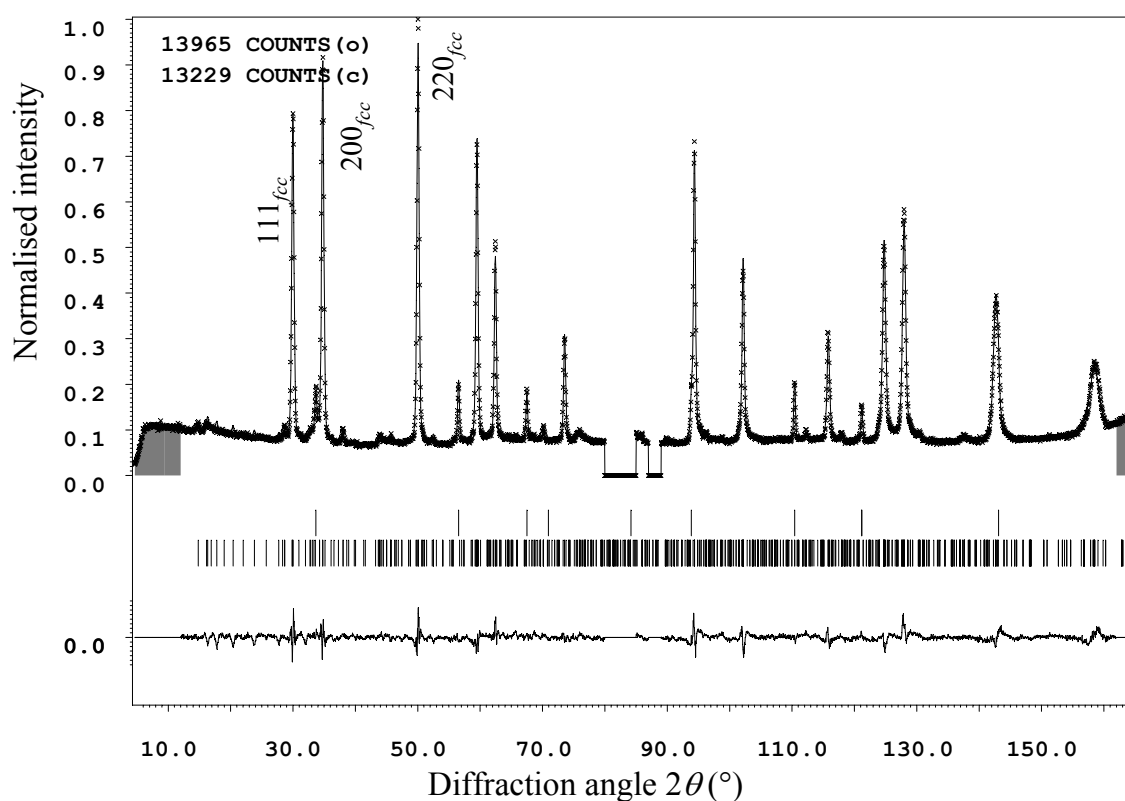


Fig. 4.8. Rietveld refinement on the basis of the neutron diffraction pattern recorded at 15 K from the quenched Pd¹¹B_{0.158} sample after annealing for 5 min at 800°C (alloy 1): measured data points, calculated intensity profile and difference curve. The reflection markers indicate reflection positions of diamond (top of marker bar), an impurity (see section 4.3.1.) and of ordered Pd₆B. Regions excluded from the refinement have been shaded; the corresponding 2θ ranges 80-85° and 87-89° were excluded as well due to the accidental occurrence of electronic interfering signals.

⁹ The low temperature compared to room temperature has no influence on the B ordering in the phase, the measurements were recorded at 15°K in the course of another investigation [4].

In agreement with the XRD data (section 4.4.3.), the $\frac{h}{2} \frac{k}{2} \frac{l}{2} fcc$ superstructure reflections with odd hkl are the strongest superstructure reflections. Additionally, peculiar broad intensity humps occur in the NPD pattern (e.g. at about $2\theta = 44^\circ$, Figure 4.9a). Rietveld refinement was performed adopting ordering according to superstructure of type 2 (sections 4.4.2. and 4.4.3.). The monoclinic lattice parameters were taken consistent with the *pseudocubic* lattice as indicated by the unsplit fundamental reflections in the NPD data (and also in XRD data of the same specimen showing narrower reflections than the NPD data) by fixing the ratios of a_{m1} , b_{m1} , c_{m1} as well as by fixing the value of β_{m1} to 100.03° (Table 4.2). Rietveld refinement was initially performed with the fixed fractional coordinates from Table 4.2 which already gives a reasonable fit to the experimental profile (Figure 4.9b), implying that the above-mentioned intensity humps are superstructure reflections additional to the indexed $\frac{h}{2} \frac{k}{2} \frac{l}{2} fcc$ reflections with odd hkl , and being thus characteristic for the superstructure of type 2. In a next step refinement of the fractional coordinates of the Pd and B atoms led to a significant improvement of the fits (Figure 4.9a), in particular to the superstructure reflections, although considerable correlations occur between the refined fractional coordinates, in particular for the Pd atoms. The final coordinates are listed in Table 4.6. Comparison of the finally calculated diffraction pattern with the observed diffraction pattern suggests that some superstructure reflections are relatively broad, whereas others are relatively sharp (in particular the $\frac{h}{2} \frac{k}{2} \frac{l}{2} fcc$ reflections with odd hkl) (see 4.5.1.).

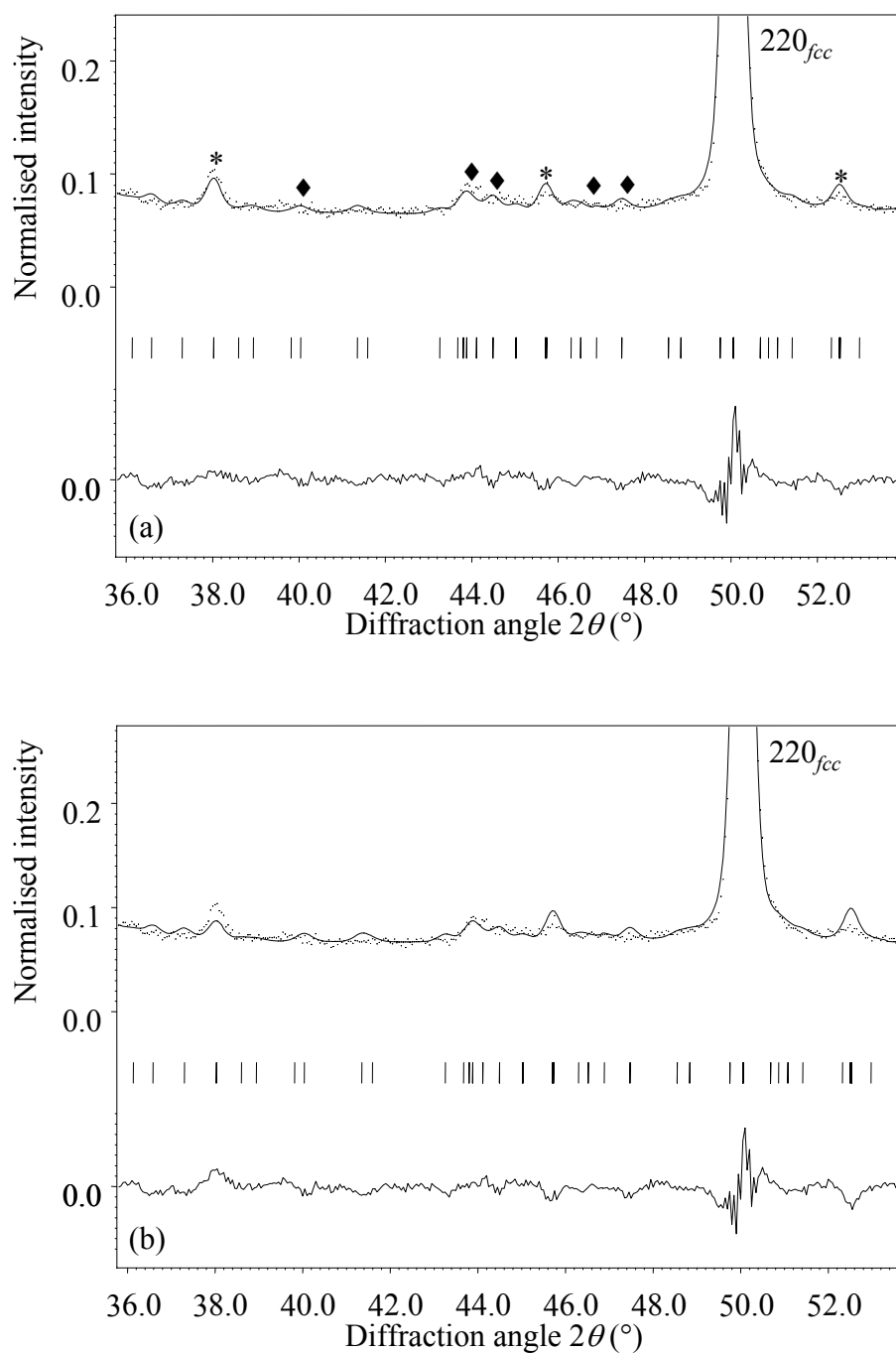


Fig. 4.9. (a) Enlarged part of Figure 8. Fundamental reflections have been indicated by hkl_{fcc} , superstructure reflections $\frac{h}{2} \frac{k}{2} \frac{l}{2}_{fcc}$ with odd h, k, l by stars (*) and further (noticeable) superstructure reflections by diamonds (♦). (b) shows the same region after a Rietveld refinement using fixed ideal fractional coordinates according to Table 4.2, demonstrating the influence of the Pd atom displacements from their ideal sites on the intensities of the superstructure reflections (compare Figure 4.9a (allowing for displacements) with Figure 4.9b (Pd atoms on ideal positions)).

Table 4.5. Experimental details for the neutron powder diffraction data taken at 15 K from ordered Pd₆B phase powder of the composition Pd¹¹B_{0.158} (alloy 2 powder quenched from 800°C), containing diamond impurities from filing. Figure of merits for the performed Rietveld analysis have been indicated. For the refined fractional coordinates of the Pd₆B phase see Table 4.6.

wave length (Å)	1.1966
diffraction angle range used (°)	12-162
stepwidth (°)	0.05
excluded regions (°) ^a	80-85, 87-89
phase 1	Pd ₆ B (composition Pd ¹¹ B _{0.158})
space group	C2/c
coherent scattering lengths [27], <i>b</i> (barn)	
Pd	5.91
¹¹ B	6.65
<i>a</i> _{m1} (Å)	$=\sqrt{6}/2 a_{fcc}$
<i>b</i> _{m1} (Å)	$3\sqrt{2}/2 a_{fcc}$
<i>c</i> _{m1} (Å)	$=\sqrt{22}/2 a_{fcc}$
β _{m1} (°)	$\arccos(-1/\sqrt{33})$
<i>a</i> _{fcc} (Å) ^b	3.99279(4) Å
fractional coordinates: see Table 4.6	
phase 2	diamond
crystal system	monoclinic
space group	$Fd\bar{3}m$
fractional coordinates: C	1/8 1/8 1/8
coherent scattering lengths [27], <i>b</i> (barn)	
C	6.646
<i>a</i> (Å)	3.56692(8)
weight fraction diamond	0.0082(3)
<i>R</i> _{wp} [34]	0.0569
<i>R</i> _B [34]	0.0579
<i>R</i> _{wp} and <i>R</i> _B with ideal fractional coordinates from Table 4.2:	
<i>R</i> _{wp} = 0.0624; <i>R</i> _B = 0.0746	

^a Due to accidental occurrence of interfering signals

^b The lattice parameters are restricted to be pseudocubic, so that *a*_{fcc} constitutes effectively the only refined lattice parameter of the Pd₆B phase.

Table 4.6. Refined fractional coordinates of ordered Pd₆B^a (composition Pd¹¹B_{0.158}; C2/c; ideal structure model, see Table 4.2) as obtained by Rietveld analysis of the neutron powder diffraction data taken at 15 K.

Atom	Wyckoff site	$x=x_{id} + \delta x^b$	$y=y_{id} + \delta y^b$	$z=z_{id} + \delta z^b$	$\langle u^2 \rangle$ (Å ²) ^c	occupancy
B	4e	0	0.0807(10)	¼	0.0071(-)	0.954(-) ^d
Pd1	8f	0.125(3)	0.2507(7)	0.1200(6)	0.0026(1)	1
Pd2	8f	0.120(2)	0.5819(7)	0.1244(4)	$=\langle u^2(\text{Pd1}) \rangle$	1
Pd3	8f	0.128(3)	0.9104(7)	0.1223(4)	$=\langle u^2(\text{Pd1}) \rangle$	1

^a Further details of the crystal structure investigation is available from the Fachinformationszentrum Karlsruhe, D-76344 Eggenstein-Leopoldshafen, Germany (fax: +49-7247-808-666; email: crysdata@fiz-karlsruhe.de) on quoting the depository number CSD-415013, the name of the author, and the citation of the paper.

^b The fractional coordinates are regarded as the sum of the ideal coordinates (see Table 4.2) modified by displacements δx , δy , δz .

^c The atomic displacement parameter for B was fixed at the same value used for a series of PdB_y alloys at 15 K [14]. The atomic displacement parameters of Pd were assumed to be the same for the three different Pd sites.

^d The occupancy of the B site was fixed at the value expected from the composition Pd¹¹B_{0.158} and the assumption that all B is located on this site.

4.5. Discussion

4.5.1. The ordered arrangement of B in Pd₆B

The here observed ordering pattern of B on the octahedral interstices of the *ccp* arrangement of Pd atoms (superstructure of type 2) corresponds to that of vacancies on the octahedral interstices of the *ccp* arrangement of V atoms in a superstructure reported for V₆C₅ [75].

The formation of superstructures of types 1-3, i.e. including the observed one of type 2 (see Figure 4.2), can be understood qualitatively considering repulsive pair interactions B···B: The superstructure avoids the occurrence of (i) nearest neighbour B···B pairs (i.e. avoids 'edge-sharing' Pd₆B octahedra using the terminology of the Pauling rules [76], for which $d = 2^{1/2}/2a_{fcc}$, where d is the distance between the pair of B atoms considered, if distortions with respect to the initially disordered *fcc* structure are neglected) and of (ii) next-nearest neighbour B···B pairs (i.e. avoids 'corner-sharing' Pd₆B octahedra for which $d = a_{fcc}$). This is realised by keeping each second layer of octahedral sites perpendicular to one $[111]_{fcc}$ direction (i.e. $[\bar{1}\bar{1}\bar{1}]_{fcc}$ in the Pd₆B structure as given in Table 4.2) devoid of B atoms, whereas

the other half of the octahedral layers is occupied by B with an (average) occupancy¹⁰ of 1/3 (Figure 4.2a). By this type of incorporation of B atoms into only each second layer of octahedral sites, the occurrence of next-nearest neighbour pairs B...B is excluded. Furthermore, a specific ordering of B atoms exists within the occupied layers, as indicated in Figure 4.2b, ensuring that also no nearest-neighbour pairs B...B occur, and leads to the occurrence of isolated [BPd₆] (formally molecular) entities. The composition PdB_y with $y = 1/6$ is the one with the highest B content for which this is possible.

The superstructures of types 1-3 differ only in the way of stacking of the (partially) occupied layers of octahedral interstices [68]. In all these superstructures nearest and next-nearest neighbour B...B pairs are absent. The relative stability of the three superstructure types is determined by (subtle) longer distance (pair-)interactions. This makes faulting in the stacking sequence discussed likely. The occurrence of faulting is indeed suggested by the diffraction streaks (see section 4.4.2.) along $[\bar{1}\bar{1}\bar{1}]_{fcc}$, i.e. parallel to the stacking direction of the alternately (partly) occupied and unoccupied layers of octahedral sites; a similar phenomenon was observed for V₆C₅ [78]. Moreover, the line-broadening of certain weak superstructure reflections as observed in the NPD data (see section 4.4.4.) also suggests faulting; see similar phenomena in NPD patterns observed for Nb₆C₅ (for which type 1 superstructure occurred) [79].

According to the fundamental reflections the average lattice of the Pd₆B phase of the Pd¹¹B_{0.158} as quenched from 800°C is apparently not distorted: it is *pseudocubic* (cf. section 4.4.2.). This means that systematic overlap between inequivalent Bragg reflections occurs in the NPD data, in particular for the fundamental reflections. Yet, the Rietveld refinement on the basis of the NPD data is able to reveal (Table 4.6, and comparison of Figure 4.9a and b) that shifts of the Pd and B atoms with respect to their ideal fractional coordinates occur (Table 4.2). In the undistorted structure (as described by the ideal fractional coordinates (cf. Table 4.2) using the refined *pseudocubic* lattice parameter $a_{fcc} = 3.993$ Å, (cf. Table 4.5) all distances Pd – B within the isolated Pd₆B entities would be $a_{fcc}/2 = 1.996$ Å. However, the refined fractional coordinates indicate significantly larger Pd – B distances within these entities ranging from 2.02(1) to 2.05(1) Å (Figure 4.2c). The angles B – Pd_{ideal} – Pd (where Pd_{ideal} corresponds to Pd sites with the ideal fractional coordinates from Table 2) vary between 138° and 166° for Pd1, Pd2 and Pd3, indicating that the displacements of the Pd

¹⁰ Note that complete occupation of the latter octahedral layers leads to the CdCl₂-type structure as occurring for a couple of hemicarbides, M₂C [38].

atoms from their ideal sites occur largely radially away from the B atom (for purely radial displacements the angle B – Pd_{ideal} – Pd would be 180°). For the disordered solid solution such Pd atom displacements were observed and described in terms of a static displacement contribution to the overall atomic displacement parameters [14]. The shortest Pd-B distances in Pd₆B, 2.02 to 2.05 Å (at 15 K), are about equal to or somewhat shorter than those observed for other compounds with octahedral coordination of B by Pd, e.g. $d(\text{Pd-B}) = 2.04$ Å for YbPd₃B [80], 2.10-2.12 Å for Pd₂B [81] or 2.13 Å for Li₂Pd₃B [82].

The displacements of the Pd atoms in Pd₆B lead to Pd-Pd distances ranging from 2.74(1) to 2.91(1) Å (see Figure 4.10; the twelve nearest Pd neighbours of Pd1, Pd2 and Pd3 were considered, leading to 36 Pd-Pd pairs), whereas the Pd-Pd nearest neighbour distances would be equal to $a_{fcc}/2^{1/2} = 2.82$ Å for an undistorted *ccp* structure of Pd atoms with lattice parameter a_{fcc} . As follows from the radial displacements of the Pd atoms surrounding octahedrally a B atom, the Pd-Pd distances which form the edges of [BPd₆] octahedra are the longest nearest neighbour distances for Pd, i.e. all longer than 2.855 Å (12 distances, see Figure 4.10), whereas the other ones (being edges of only unoccupied Pd₆ octahedra) are shorter than 2.855 Å (24 distances). The present observations concerning Pd-Pd nearest neighbour distances agree well with results from EXAFS measurements on disordered PdB_{0.16} [8]. The EXAFS signals were interpreted by fitting to the experimental data two different shortest Pd-Pd distances of 2.782(5) Å and 2.897(5) Å, respectively, which are smeared due to static displacements in a Gaussian fashion (see Figure 4.10). The distance of 2.897(5) Å was attributed to edges of Pd₆ octahedra occupied by B, and the distance of 2.782(5) Å was attributed to edges of unoccupied Pd₆ octahedra.

The observed deviations of the fractional coordinates of Pd in Pd₆B from the geometrically ideal ones can be understood recognising the relative large size of B with respect to the size of the octahedral sites of Pd [11], as also evidenced by the strong dependence of the lattice parameter of the PdB_y solid solution on the B content, as given by Eq. (4.1).

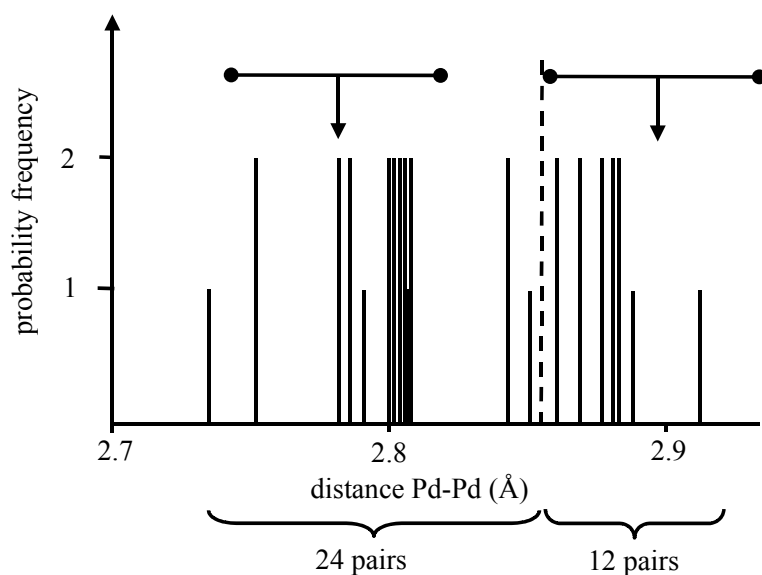


Fig. 4.10. Histogram showing the distribution of Pd-Pd distances shorter than 3 Å for the coordination spheres of one Pd1, one Pd2 and one Pd3 atom in Pd₆B. The 24 distances shorter than 2.855 Å (limit indicated by dashed line) correspond to edges of empty Pd₆ octahedra, whereas the 12 longer ones correspond to Pd₆ octahedra occupied by B ([BPd₆] entities). The arrows indicate the maxima of two Gaussian Pd-Pd distance distributions located at 2.782(5) Å and 2.897(5) Å fitted to EXAFS data for Pd-Pd distances [8]. The standard deviation ranges 2σ of these distance distributions have been indicated by horizontal bars.

Formation of the Pd₆B phase from disordered PdB_{0.144} led to a considerably distorted, *pseudotetragonal* lattice (according to the fundamental reflections), whereas Pd₆B obtained by the not sufficiently drastic quenching of Pd¹¹B_{0.158} from 800°C is *pseudocubic*, and remains *pseudocubic* even after annealing treatments comparable to those subjected to PdB_{0.144}. Although the observed lattice parameters of the Pd₆B generated in these two ways are different, the volumes of the *pseudocubic* and of the *pseudotetragonal* cells are practically the same, and thus the estimated compositions are the same (see Table 4.4). Further, the electron and X-ray diffraction evidence attained in this work demonstrates that the type of ordering in both cases is also the same (superstructure of type 2).

The occurrence of the *pseudocubic* and *pseudotetragonal* manifestations for the same Pd₆B phase is a striking observation, because, if equilibrium occurs, at the same measuring temperature, pressure and composition the same lattice parameters should occur for a crystalline phase irrespective of the way of preparation. Hence, the occurrence of different lattice parameters for the same phase must have a microstructural origin. Due to the monoclinic symmetry of the Pd₆B phase usually anisotropic ordering strain [83], with respect

to the original *fcc* solid solution, is expected, reflecting a long-range accumulation of the local atomic displacements due to the ordering. If monoclinic domains are formed initially coherently in an initially cubic crystallite, the ordering strain can be accommodated by a special arrangement of ordered domains and/or elastic/plastic deformation. Possibly remaining coherency stresses counteracting the ordering strain will elastically distort the domains so that lattice parameters different from the equilibrium ones are measured. Therefore, the different lattice parameters of the *pseudocubic* and of the *pseudotetragonal* manifestations of Pd₆B are likely due to their different domain microstructures caused by different initial alloy compositions and thus different ‘ways’ of formation (section 4.5.2.). Probably, neither the *pseudocubic* nor the *pseudotetragonal* manifestation exhibit the ‘true’ (stress free) lattice parameters of ordered Pd₆B (of the considered composition).

4.5.2. Consequences for the constitution of the binary system Pd-B

The experimental results presented in this work are compatible with a tentative phase diagram for the Pd-B system (Pd-rich side) as proposed in Figure 4.11. The compositions of the three PdB_y alloys investigated have been indicated (Table 4.3). The composition PdB_{0.163} (alloy 3) apparently lies within the homogeneity range of the Pd₆B phase, because it was possible to transform the whole quenched sample into this phase upon annealing at 360°C (section 4.4.2.). The same quenched alloy was analysed by DSC, which indicated that the congruent transformation, ordered Pd₆B \rightleftharpoons disordered PdB_{1/6}, occurs at about 440(5)°C (section 4.4.1.).

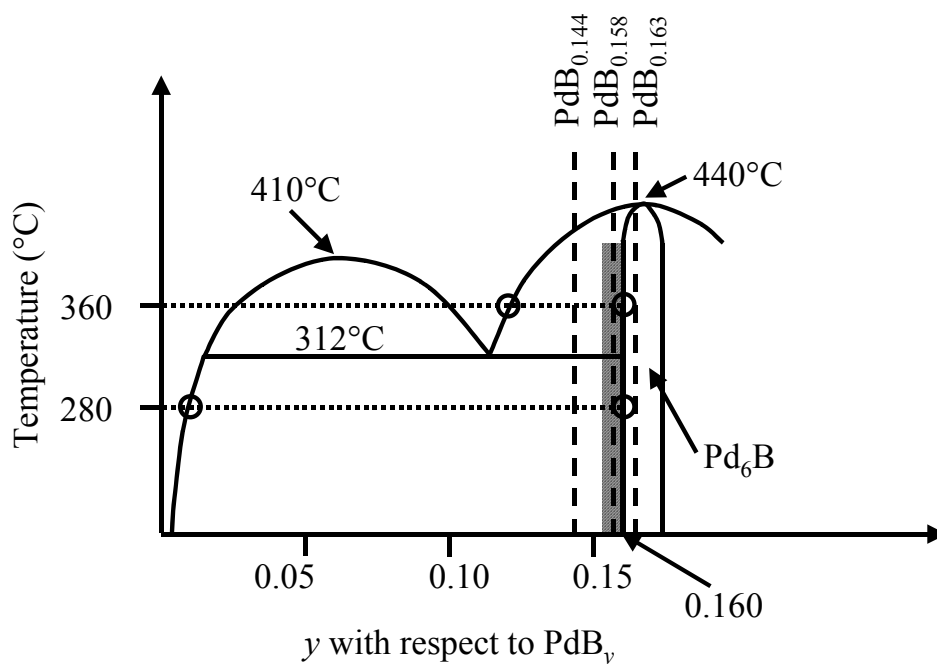


Fig. 4.11. Proposed phase diagram of the Pd-B system (Pd-rich side) indicating the observed phases, their respective compositions and the initial compositions of the alloys investigated in this work. The shaded region indicates that upon moderately fast cooling of the PdB_y solid solution in that range a homogeneous (ordered) Pd₆B phase (of unchanged B content) develops, which upon annealing decomposes by diffusion according to the two-phase regions as indicated (see open circles).

The not sufficiently drastic quenching of Pd¹¹B_{0.158} (alloy 2) led to, also, an apparently homogeneous Pd₆B phase (sections 4.4.3. and 4.4.4.). However, the Pd₆B phase with this composition is not stable at the annealing temperatures of 360°C and 280°C because it is decomposed into the Pd₆B phase with the composition PdB_{0.160} and a disordered PdB_y solid solution (of composition about PdB_{0.009} at 280°C and of composition about PdB_{0.126} at 360°C; Table 4.4). These results are compatible with the presence of a miscibility gap with a critical temperature of 410°C and a monotectic temperature at 312°C adopting values as given in Ref. [5].

Evidently, the ordered phase Pd₆B is easily formed upon cooling by ordering of the B atoms on the octahedral interstices of *ccp* Pd as suggested by the difficulties to retain the solid solution upon quenching of the PdB_{0.163} (alloy 3) bulk material (end of section 4.4.1.) and the relatively large powder batch of Pd¹¹B_{0.158} (alloy 2, section 4.4.3. and 4.4.4.). Clearly, the subsequent decomposition of the latter alloy upon annealing (into the ordered phase Pd₆B

of composition PdB_{0.160} and the solid solution PdB_y of lower B content) requires much more time at the same temperature since long-range diffusion is necessary.

The rapid formation of the ordered Pd₆B phase from the solid solution even during quenching has only been observed in a limited composition range below about $y = 1/6$, as indicated in Figure 4.11 by the shaded region: the solid solution of the composition PdB_{0.144} could be retained easily (section 4.4.3.). Subsequent annealing of PdB_{0.144} produced the same equilibrium phases as annealing of quenched Pd¹¹B_{0.158}. This suggests that the Pd₆B phase cannot be formed with the composition PdB_{0.144}. Thus, in the PdB_{0.144} alloy, long-range diffusion is required leading to the enrichment of B in parts of the alloy where the ordered Pd₆B phase develops (now in its *pseudotetragonal* form; see sections 4.4.2. and 4.4.3., and Figure 4.5).

Because of coincidence of the lattice parameter of $a_{fcc} = 4.005 \text{ \AA}$ of the apparently cubic 'Pd₁₆B₃' phase (PdB_{0.188}) [5] with the value of $a_{fcc} = 4.001\text{--}4.002 \text{ \AA}$ as observed for *pseudocubic* Pd₆B as generated from alloy 2 of the average compositions Pd¹¹B_{0.158} (see section 4.4.3.) and because of the compatibility of the superstructure reflections $\frac{h}{2} \frac{k}{2} \frac{l}{2}_{fcc}$ with odd hkl observed for the 'Pd₁₆B₃' phase with similar reflections observed in this work for the Pd₆B phase (exhibiting the superstructure of type 2) for compositions close to PdB_{1/6}, it seems very likely that both phases, in fact, are the same. The difference between the assigned compositions – PdB_{0.188} [5] and PdB_{0.163} (this work) – probably originates from the different methods used to assign compositions to alloys, and their possible systematic errors: The good agreement of the reported lattice parameter values (see above), in fact, suggests that the composition of 'Pd₁₆B₃' from Ref. [5] in reality is close to the composition of the presently observed Pd₆B phases. In this context, it must be mentioned that in the present work all compositions, of both the solid solution phase and the Pd₆B phase were obtained by application of Eq. (4.1), which was determined on the basis of measured lattice parameters of an extensive series of PdB_y solid solution samples and chemical analyses of the corresponding samples [11]. In Ref. [5] a different equation was used¹¹. Finally, in any case the occurrence of an ordering pattern based on the avoidance of nearest-neighbour and next-nearest-neighbour B...B pairs (leading to isolated Pd₆B entities) strongly suggest that the B content in the Pd₆B phase cannot be higher than as indicated by PdB_{1/6}.

¹¹ A considerable lattice volume shrinkage of $\Delta V/V = 0.75 \%$ was reported [6] to occur upon ordering. The present data cannot confirm this due to the lack of solid solution lattice parameters for these alloys. Yet the good consistency of the B considerations in Table 4.4 and section 4.4.3. seem to contradict the magnitude of this shrinkage.

4.6. Conclusions

(i) The crystal structure of the Pd₆B phase can be described as a superstructure variant of the PdB_y solid solution with *fcc* arrangement of Pd and B on the octahedral interstices. The observed occupational ordering pattern (space group *C2/c*) of the B atoms avoids the occurrence of nearest and next-nearest neighbour pairs B...B. The crystal structure can be regarded as built from "isolated" BPd₆ entities, conserving the basic cubic close-packed arrangement of Pd. The same ordering pattern as observed for the B atoms in Pd₆B□₅ has been observed previously for vacancies in defect-NaCl type V₆C₅□ in which V takes the places of Pd, C those of □, and □ those of B.

(ii) The same ordered Pd₆B phase can occur, for the same composition, in different *manifestations* with respect to its lattice parameters, a *pseudocubic* one, which forms upon direct formation of B ordering from the solid solution which has the same composition as the Pd₆B phase, and a *pseudotetragonal* one, which forms when the Pd₆B precipitates from a (quenched) solid solution of significantly lower B content than the Pd₆B phase.

(iii) The phase equilibria between the ordered Pd₆B phase and the disordered PdB_y solid solution of (much) lower B content have been established.

Appendix to Chapter 4

Table A1. Idealised structure parameters for the type 1 superstructure candidate for Pd₆B:

space group $P3_112$: $\mathbf{a}_{tr} = 1/2[\bar{1}\bar{1}\bar{2}]_{fcc}$ ($a_{tr} = \sqrt{6}/2 a_{fcc}$), $\mathbf{b}_{tr} = 1/2[\bar{1}12]_{fcc}$ ($b_{tr} = \sqrt{6}/2 a_{fcc}$), $\mathbf{c}_{tr} = 2[\bar{1}\bar{1}1]_{fcc}$
 ($c_{tr} = 2\sqrt{3} a_{fcc}$), $V_{tr} = 4.5V_{fcc}$.

Atom	Wyckoff site	x_{id}	y_{id}	z_{id}
B	$3a$	1/9	8/9	1/3
Pd1	$6c$	1/9	8/9	7/12
Pd2	$6c$	4/9	5/9	7/12
Pd3	$6c$	7/9	2/9	7/12

Table A2. Idealised structure parameters for the type 3 superstructure candidate for Pd₆B:

space group $C2/m$: $\mathbf{a}_{m2} = 1/2[\bar{1}\bar{1}\bar{2}]_{fcc}$ ($a_{m2} = \sqrt{6}/2 a_{fcc}$), $\mathbf{b}_{m2} = 3/2[110]_{fcc}$ ($b_{m2} = 3\sqrt{2}/2 a_{fcc}$), $\mathbf{c}_{m2} = 1/2[\bar{1}\bar{1}\bar{2}]_{fcc}$
 ($c_{m2} = \sqrt{6}/2 a_{fcc}$), $V_{m2} = 3V_{fcc}$, $\beta_{m2} = \arccos(-1/3) = 109.47^\circ$.

Atom	Wyckoff site	x_{id}	y_{id}	z_{id}
B	$2a$	0	0	0
Pd1	$4i$	1/4	0	3/4
Pd2	$8j$	1/4	2/3	3/4

5.

The Pd-rich part of the Pd-B phase diagram

T. G. Berger, A. Leineweber, E. J. Mittemeijer

The Pd-B system in the composition range of the solid solution PdB_y has been the topic of a number of investigations as it provides an attractive model system for interstitial compounds. No consensus about the crystal structures and phase boundaries, particularly in the low-temperature regime, has been reached in earlier works. In the light of very recent results on the crystal structure and composition ranges of the low-temperature phases, on the basis of X-ray, electron and neutron diffraction analyses, a tentative phase diagram is presented which is compatible with practically all previous results.

5.1. Introduction

The extraordinary properties of the palladium-rich terminal solid solution of the Pd-B system motivated a large number of studies using it as a model system for interstitial alloys. On the one hand, striking disagreements between structural and compositional results of the different works exist. On the other hand, certain general key features are agreed upon: Palladium dissolves up to ~20 at. % boron at temperatures higher than 450°C (e.g. [5]). The boron atoms are regarded to occupy the octahedral interstices of the *fcc* palladium lattice without exhibiting long-range order [4, 5]. This has been demonstrated by studying the diffusivity of H in PdB_y alloys [7], by extended X-ray absorption fine structure analysis (EXAFS) [8] and by neutron powder diffraction [14]. Upon dissolving boron, the Pd host lattice experiences an exceptionally large expansion, as indicated by the strong composition dependence of the cubic lattice parameter a_{fcc} as measured at ambient temperatures [4, 5, 11]. Three quite similar equations have been formulated:

$$a_{fcc} = 3.8875 \text{ \AA} + 0.675 \text{ \AA} y \quad (5.1), \text{ from [4]}$$

$$a_{fcc} = 3.8895 \text{ \AA} + 0.660 \text{ \AA} y \quad (5.2), \text{ from [5]}$$

$$a_{fcc} = 3.8920 \text{ \AA} + 0.6882 \text{ \AA} y \quad (5.3), \text{ from [11]}$$

where y denotes both the atomic ratio B/Pd (corresponding to y in PdB_y) and the occupancy of the octahedral interstitial sites by B atoms.

The solid solution is only stable at elevated temperatures, but can be retained by quenching. The local strain effects of a random incorporation of B atoms on the octahedral interstices of the PdB_y solid solution were studied in terms of static displacements of the Pd atoms from their ideal sites by EXAFS [8] and neutron powder diffraction [14].

According to Hägg's rule of a critical atomic radius ratio for the occurrence of interstitial solid solutions [20, 21], interstitial incorporation of boron into palladium should be quite unfavourable [11]. Similar conclusions can be drawn from the large magnitude of the so-called volume-size factor proposed as a criterion by King [26]. These geometric criteria apparently do not apply to Pd-B.

Similar to PdH_y, the thermodynamic properties for PdB_y can straightforwardly be measured as a function of y . To this end, PdB_y is equilibrated with atmospheres of controlled

B activity [4, 6]. Thereby, the outstanding character of the solid solution Pd-B is revealed by the particularly negative partial dissolution enthalpy of B in Pd compared to the values found for B in Ni and B in Pt [6]. However, the occurrence of a pronounced solid solubility (as observed for Pd-B) is not only determined by the Gibbs energy of formation of the solid solution, but it is determined by the relative magnitudes of the Gibbs energies of the solid solution and the adjacent intermetallic phase which is in the case of Pd-B the Pd₃B phase.

Furthermore, the non-ideal solid solution PdB_y is a perfect candidate for the application of thermodynamic models [4, 6] for interstitial compounds with a large composition range. The *y*-dependent excess contributions to the Gibbs energy of formation of the PdB_y solid solution were interpreted to consist of elastic interactions of the B atoms as well as of an electronic contribution. The concentration dependence of this electronic contribution can be understood by the chemical bonding situation in PdB_y, where 2*s* and in particular 2*p* orbitals of B overlap with the 4*d* orbitals of Pd leading to Pd-B bonding and where, at the same time, the additional electrons provided by B cause an increase of the Fermi-energy, as also observed for H and C in Pd but also for substitutional Pd alloys [84, 85, 86].

The observed *y*-dependent excess contributions to the Gibbs energy successfully predict the occurrence of a miscibility gap in the solid solution field [4]. On the basis of X-ray diffraction experiments, this miscibility gap was reported to occur in the range of 0.02 < *y* < 0.11 between the temperatures of a monotectic point (312°C, *y* = 0.11) and of a critical point at *y* = 0.065 at 410°C (cf. Figure 5.1a) [4, 5]. A slightly different composition range for the miscibility gap was reported later [48].

Besides the above discussed miscibility gap, more two-phase areas and one or more low-temperature phases with various *fcc* type based crystal structures have been reported at temperatures lower than 450°C in the range of the compositions Pd-PdB_{0.2}, which are dealt with below in more detail.

The phase diagram reported in Ref. [5] (Figure 5.1a) shows for higher boron contents *one* low-temperature phase occurring below 397°C which was characterised later as Pd₁₆B₃ having an apparently cubic superstructure with $a' = 2a_{fcc}$ (where a_{fcc} denotes the cubic lattice parameter of the corresponding *fcc* solid solution) due to the occurrence of superstructure reflections which could be indexed by half-integer *h*, *k* and *l* with respect to a_{fcc} (cf. Figure 5.1a) [5]. Recently, a low-temperature phase Pd₅B was reported with a tetragonally distorted structure ($c_{fct} < a_{fct}$ with *fct* denoting face-centred tetragonal) which formed apparently

congruently from the solid solution below the temperature of $385(1)^\circ\text{C}$ [12]. This Pd_5B phase was supposed to be identical to the mentioned Pd_{16}B_3 phase.

Another reported phase diagram (cf. Figure 5.1b) [10], based on differential scanning calorimetry (DSC) and X-ray powder diffraction measurements (XRD) (no details were provided), shows *two* low-temperature phases Pd_{-6}B (polymorphic transition temperature: $440(5)^\circ\text{C}$) and Pd_{-5}B (decomposing peritectically at $372(5)^\circ\text{C}$) without providing any crystallographic information.

Some controversial issues about the Pd-B equilibrium phase diagram, concerning mostly high-temperature phases occurring for boron contents higher than those considered here, have been addressed in Ref. [22]. The aim of the present work is to clarify the abovementioned apparent disagreements concerning the low-temperature behaviour in the Pd-B system for the composition range of the PdB_y solid solution largely on the basis of three recent works [17, 18, 19].

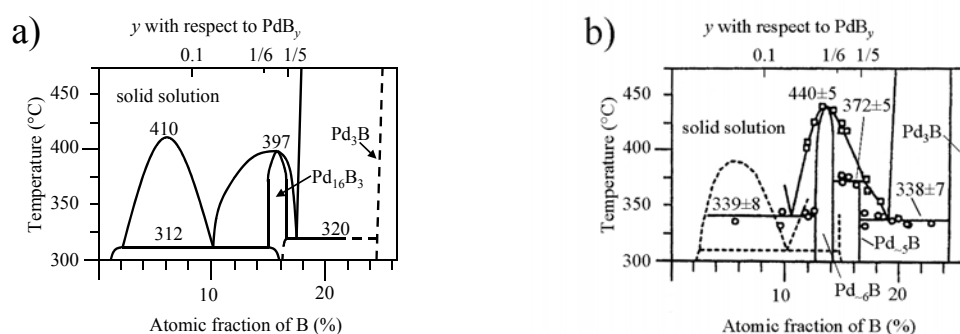


Figure 5.1. Phase diagrams reproduced (a) according to Ref. [5] and (b) as reported in Ref [10].

5.2. Solid solution

So far, three equations (Eq. (5.1)-(5.3)) have been published to calculate the boron content y from the cubic lattice parameter of the solid solution. These equations have been obtained by relating the measured lattice parameter a_{fcc} (room temperature) with the composition determined either by weight gain of the Pd pieces upon gas loading (Eq. (5.1), [4]; Eq. (5.2), [5]) or by chemical analyses (Eq. (5.3), [11]). Which of the three equations fits reality most exactly cannot be said but the most probable error source are the used methods of composition determination. However, already published values for pure Pd scatter considerably [87], with most values being close to 3.8905 \AA .

Nevertheless, the determination of lattice parameters by XRD employing state-of-the-art techniques can be regarded as significantly more accurate than the applied composition determination methods and can also be applied to assign compositions to phases in multi-phase mixtures e.g. generated by annealing alloys within the miscibility gap. By adopting any of the Eq. (5.1-5.3), XRD allows determining a consistent picture of the compositions of various specimens and of the location of the phase boundaries of the associated miscibility gap. Yet, given a certain lattice parameter a_{fcc} , one obtains considerably different compositions e.g. $a_{fcc}=4.005 \text{ \AA}$ results in calculated compositions of $y = 0.174$ by Eq. (5.1), $y = 0.175$ by Eq. (5.2) and $y = 0.164$ by Eq. (5.3). If composition values from different works (related with lattice parameter data) are compared, care must be taken since apparently contradictory compositions may also be the result of application of different formulas to relate a_{fcc} and y .

5.3. Miscibility gap in the solid solution field

The decomposition of the solid solution in the range of the miscibility gap has been investigated by ex-situ annealing-time resolved X-ray powder diffraction measurements; small powder samples taken from one large homogeneous batch were annealed for various times at different temperatures [16]. The progress of the decomposition has been traced by fitting a discretised probability density function for composition, $p(y)$, to the diffraction patterns. The following observations have been made by analysis of the time- and annealing temperature-dependent evolution of $p(y)$:

Maxima in $p(y)$ indicate the presence of three main components: the initial solid solution with a phase fraction decreasing with annealing time, as well as two ‘boundary phases’ with phase fractions increasing with annealing time. The two latter components have a lower and a higher B content than the decomposing initial solid solution, respectively, which further decrease and increase with annealing time, asymptotically approaching ‘final values’ (Figure 5.2) which should correspond to the boundaries of the miscibility gap. The lattice parameters of the boundary phases of the miscibility gap at 340°C and 355°C measured by X-ray diffraction¹² [16] largely reproduce earlier measurements [4], but do not

¹² The lattice parameters of the maxima in $p(y)$ were determined by parabolic fits of the three highest local $p(y)$ values.

agree with the results from Ref. [48]. Thus, as expected, the lattice parameters for the ‘boundary phases’ depend strongly on the annealing temperature, but apparently also slightly on the composition of the initial solid solution. This may be attributed to phenomena related with the microstructure and misfit strains between the different phases. Furthermore, the XRD patterns reveal remaining diffracted intensity between the two reflections pertaining to the boundary phases, even for very long annealing times (of up to 8 weeks, cf. Figure 5.2).

The rate of the decomposition depends on the annealing temperature and on the composition of the initial solid solution. The decomposition is faster for lower annealing temperatures (corresponding with a larger width of the miscibility gap) and faster for compositions close to the middle of the miscibility gap ($y \sim 0.065$). This behaviour can be understood if the reaction rate depends on the magnitude of the driving force, i.e. the Gibbs energy difference upon decomposition, which - for a given temperature - is largest in the middle of the composition range of the miscibility gap and - for a given composition - increases with decreasing temperature.

Although XRD and conductivity measurements clearly confirm the occurrence of decomposition of the solid solution [4, 6, 48], until now all attempts failed to visualise the microstructure of bulk solid solution after decomposition in the miscibility gap in real space; these attempts involved application of techniques like classical metallography, scanning electron microscopy, transmission electron microscopy (TEM), spatially resolved electron energy loss spectroscopy and scanning Auger analysis [Berger, Leineweber, Mittemeijer, unpublished].

For annealing of initial solid solution in the composition range of the miscibility gap at temperatures between 295°C and 340°C, close to the monotectic temperature of 312°C given in Ref. [4], three product phases were observed, Pd₆B/Pd₁₆B₃ additional to the two boundary phases of the miscibility gap. This situation persists for long annealing times compared with typical time periods needed to establish other phase equilibria at similar annealing temperatures. Hence, it was not possible to unequivocally confirm the monotectic temperature of 312°C as obtained by resistivity measurements on the basis of XRD measurements. These ‘three phase samples’ confirmed similar observations reported earlier [4]. This might be understood as the result of the known to be fast precipitation of the Pd₆B phase in the lower two-phase area upon heating the sample from room temperature to the annealing temperature, compared to the decomposition in the miscibility gap which happens on the timescale of days [4, 16, 23].

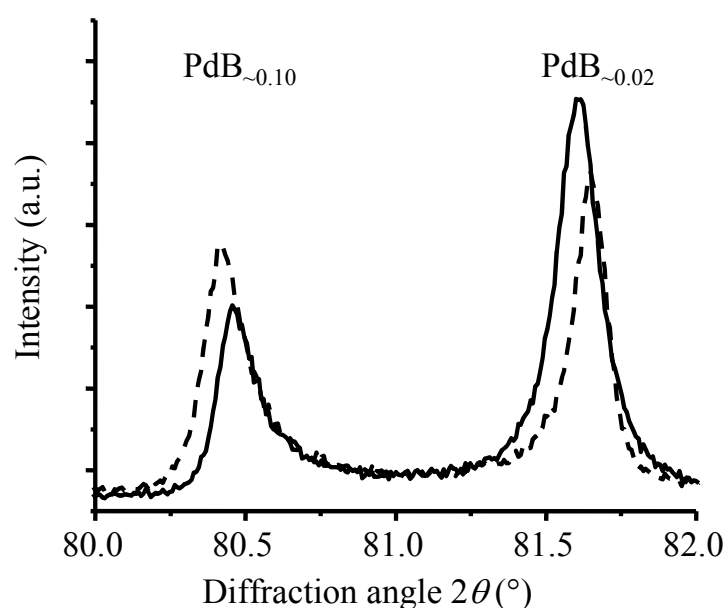


Figure 5.2. 311-Diffraction peak group showing the so-called ‘final state’ of decomposition. Patterns have been recorded from a $\text{PdB}_{0.064}$ sample (dashed line) and $\text{PdB}_{0.050}$ sample (non-interrupted line) after annealing for 8 weeks at 340°C.

5.4. Low-temperature phases

Several low-temperature phases have been mentioned in the literature (cf. Chapter 5.1). Distinctively different data regarding their compositions and crystal structures have been reported. The determination of the crystal structure of these phases on the basis of X-ray powder diffraction is difficult due to the low scattering power of B compared to Pd, which implies that at first view the X-ray diffraction patterns of the low-temperature phases closely resemble those of the solid solution. Only very weak superstructure reflections as well as a possible slight splitting of fundamental reflections (see discussion on the *pseudocubic/pseudotetragonal* Pd_6B phase below and Figure 5.3) may occur which reveal the presence of a low-temperature phase. Hence, neutron diffraction with its, as compared to X-ray diffraction, relatively large scattering power of B compared to Pd, and, in particular, electron diffraction, with its large spatial resolution allowing observation of single crystal-like diffraction patterns, can be powerful tools for the identification and characterisation of low-temperature phases. Thus, it became possible to elucidate the crystal structures of the

low-temperature phases Pd₆B and ‘Pd₅B’ [17, 19] and on that basis it was also found to be possible to explain in a comprehensive manner most of the phenomena observed in the previous works (cf. Table 5.1 and 5.2).

5.4.1. Pd₆B phase:

The so-called Pd₁₆B₃ phase, considered in Ref. [5] as an ordered low-temperature phase with doubled unit cell parameter $a' = 2a_{fcc}$, in fact is the Pd₆B phase as discussed in Ref. [17]. Similarly, also the Pd₆B phase shown in Ref. [10] in fact is the Pd₆B phase described in Ref. [17]. The reversible order-disorder transformation has been reported to occur at 440(5)°C according to DSC measurements [10, 17] or at 397°C according to XRD and resistivity measurements [5].

The boron ordering at low temperatures present in the Pd₆B phase has been elucidated by a combination of X-ray, neutron and electron diffraction [17]. The crystal structure of the ordered Pd₆B phase is monoclinic, C2/c (cf. Table 5.1), and the position of boron atoms correspond to those of the vacancies in an ordered V₆C₅ modification [72] while the C atom positions stay empty. The strongest superstructure reflections of the monoclinic Pd₆B structure correspond to the $\frac{h}{2} \frac{k}{2} \frac{l}{2} fcc$ superstructure reflections which were observed for Pd₁₆B₃ [17].

The B ordering in Pd₆B can be described as a stacking of layers of octahedral interstitial sites in a $\langle 111 \rangle_{fcc}$ direction, alternatingly empty and occupied with 1/3 B in an ordered fashion in each of the layers. In this way, it is possible to avoid nearest neighbour B···B pairs (distance B···B: $\sqrt{2}/2 a_{fcc}$) and next-nearest neighbour B···B pairs (distance B···B: a_{fcc}); thus only second next-nearest neighbour pairs occur (closest distance B···B: $\sqrt{6}/2 a_{fcc}$). This avoidance of nearest neighbours and next-nearest neighbours is established by the occurrence of ‘isolated’¹³ [BPd₆] octahedral entities as constituents of the crystal structure (Figure 5.4a), and this can only be realised for compositions $y \leq 1/6$. For $y = 1/6$ all Pd atoms can be assigned to such an isolated octahedron, for higher boron contents either next-nearest or nearest neighbour B···B pairs have to occur.

The Pd₆B phase was observed as two different forms, a *pseudocubic* one and a *pseudotetragonal* one, depending on the initial solid solution composition:

¹³ However, these octahedra must not be regarded as isolated molecules, because Pd₆B is metallic like the solid solution.

- *Pseudocubic* Pd₆B: Pd₆B prepared from solid solution compositions slightly lower than or equal to PdB_{0.167} are *pseudocubic*, i.e. the fundamental reflections of the cubic *fcc* solid solution did not split up upon ordering according to XRD, although the symmetry of the B ordering observed by electron diffraction is monoclinic. For this range of original compositions (e.g. PdB_{0.163} and Pd_{0.158}, assigned according to Eq. (5.3)) quenching turned out to be difficult, i.e. the long-range-order of the Pd₆B phase is easily formed. For PdB_{0.158} the homogeneous Pd₆B phase obtained upon quenching decomposes only upon annealing at 280°C and 360° into low-B content solid solution enriching the Pd₆B-phase in B content, while it remains *pseudocubic*.
- Pd₆B could also be obtained as a *pseudotetragonal* form (i.e. in XRD pattern the fundamental reflections of the cubic *fcc* solid solution are split as expected for a tetragonal lattice, while the B ordering is the same monoclinic one as observed for the *pseudocubic* form). This situation was observed when solid solution of significantly lower B content than PdB_{0.167} (e.g. PdB_{0.144}), which is easily retained by quenching, is annealed at 280°C or 360°C (cf. Ref. [17]). These annealing treatments give apparently the same two-phase equilibria with low-B content solid solution produced from PdB_{0.158} (see above). The only difference is the occurrence of a *pseudotetragonal* form for Pd₆B produced from PdB_{0.144} and of a *pseudocubic* form for Pd₆B produced from PdB_{0.158}. The compositions of these two forms of Pd₆B in the corresponding two-phase equilibria were estimated to be the same on the basis of the unit cell volumes.

This phenomenon (*pseudocubic* vs. *pseudotetragonal*) was ascribed to the way of formation of the ordered phase from the solid solution. The ease to form the abovementioned arrangement of [BPd₆] octahedra depends clearly on the composition of the initial solid solution, the closer to the composition Pd₆B, the easier the Pd₆B is formed. Whereas for the composition PdB_{0.158} it is still possible upon quenching to form the homogeneous Pd₆B (which however decomposes upon annealing as described above), for PdB_{0.144} this was not possible; only decomposition of the solid solution involving long-range diffusion allows formation of Pd₆B. This causes different microstructures which influence the possible distortion of the Pd host lattice.

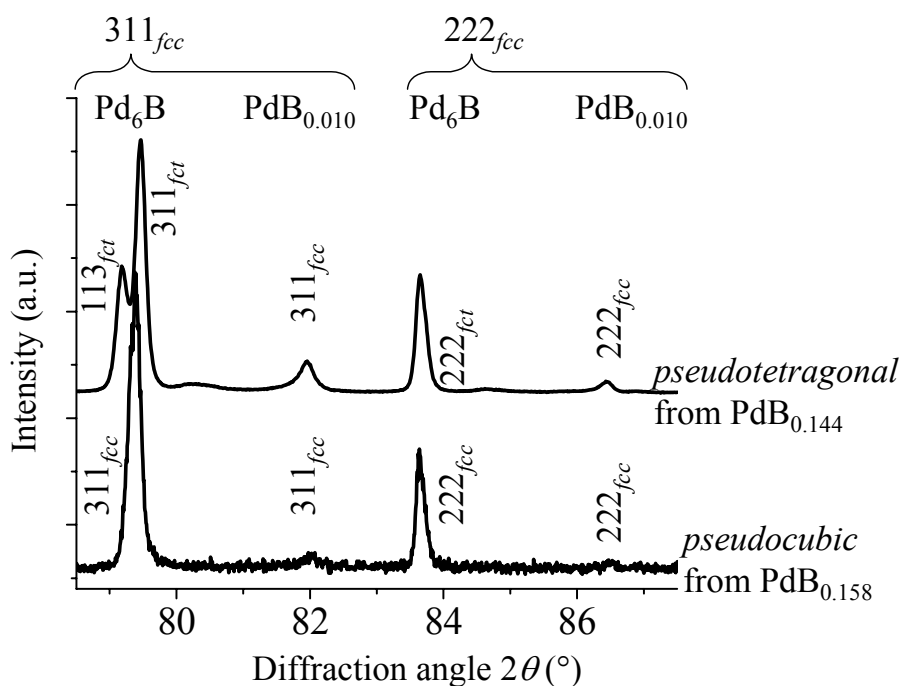


Figure 5.3. X-ray powder diffraction patterns of $\text{PdB}_{0.144}$ and $\text{PdB}_{0.158}$ alloys after annealing at 280°C for 70 h and for 3 weeks, respectively, in the two phase area below the monotectic temperature showing the expected decomposition into the Pd_6B phase and the *fcc* solid solution phase of a composition $\text{PdB}_{0.010}$. For initial compositions close to Pd_6B such as $\text{PdB}_{0.158}$, the Pd_6B phase appears as a *pseudocubic* form, for lower B contents such as $\text{PdB}_{0.144}$ the exhibited reflection splitting is *pseudotetragonal*.

5.4.2. ‘ Pd_5B ’ phase:

The apparently tetragonally distorted Pd_5B phase, decomposing upon heating at about 385°C has been suggested [12] to be identical with Pd_{16}B_3 [5]. This is not the case. Instead the Pd_5B phase is probably identical with the previously reported Pd_{-5}B [19], occurring at somewhat higher boron contents than Pd_6B . Recent X-ray and neutron powder diffraction as well as electron diffraction experiments have shown that the ‘ Pd_5B ’ phase exhibits a monoclinic crystal symmetry with an incommensurately modulated occupation of the octahedral sites by B [19]. The main structural properties can be described by a commensurate *approximant* structure having the ideal composition Pd_5B which is isostructural with UCl_5 (with space group $P2_1/n$) [61], and with Pd and B taking the roles of Cl and U, respectively. This results in a *fcc* arrangement of Pd atoms with 1/5 of the octahedral sites occupied by B in an ordered fashion. The ordering pattern of B is associated with the occurrence of nearest-neighbour

B··B pairs on the sublattice formed by the octahedral sites. This arrangement of nearest neighbour B··B pairs can also be conceived as *edge-sharing* of [BPd₆] octahedra which results in [B₂Pd₁₀] entities (Figure 5.4b).

Whereas in the superstructure of Pd₆B, isolated [BPd₆] octahedral entities can be discerned, i.e. nearest and next-nearest neighbour B··B pairs do not occur, such B··B pairs unavoidably must occur for higher B contents (maintaining mostly the *fcc* Pd arrangement). This could in principle be realised by the occurrence of either only nearest or only next-nearest neighbours B··B. The ‘Pd₅B’ structure reveals that the former occurs (B··B distance: $\sqrt{2}/2 a_{fcc}$), whereas the latter is prevented. The avoidance of next nearest B··B pairs can be qualitatively understood as follows. *Edge-sharing* of [BPd₆] octahedra (Figure 5.4b) is energetically favourable compared to *corner-sharing* of [BPd₆] octahedra (Figure 5.4c): An interstitial B atom expands the surrounding Pd octahedron in order to increase the relatively short B-Pd distances [8, 17]. The vectors describing these Pd atom displacements add up for *edge-sharing* [BPd₆] octahedra (Figure 5.4b) such that sideways displacement occurs of the Pd atoms forming the common edge. For *corner-sharing* [BPd₆] octahedra these displacements would cancel each other, and the desired larger Pd-B distances cannot be realised, thereby making this configuration energetically unfavourable (Figure 5.4c, see also Ref. [19]).

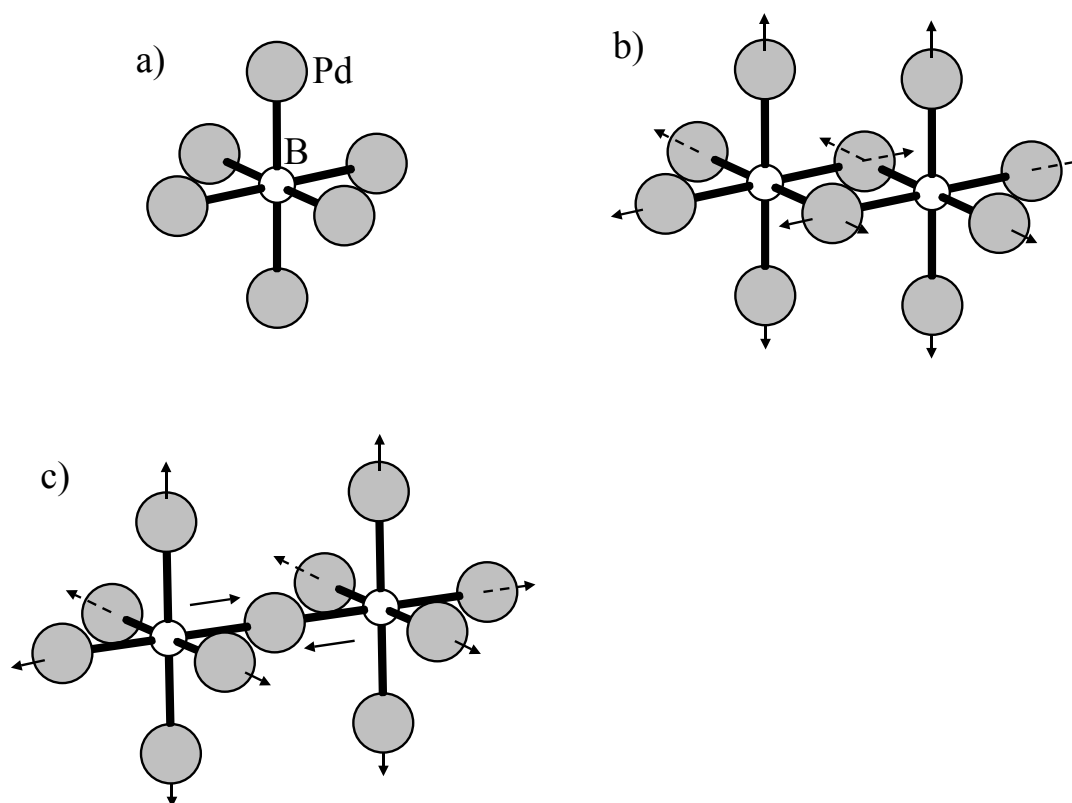


Figure 5.4. A single (a) and pairs of *edge-* (b) and *corner-sharing* (c) $[\text{BPd}_6]$ octahedra. The directions of these displacements of the Pd atoms caused by the presence of the B atoms on the octahedral interstitial site have been indicated.

The monoclinic ordering of B in the ‘Pd₅B’ phase is evidenced by characteristic splitting of the fundamental reflections in the X-ray diffraction patterns (i.e. the reflections which were already visible for the solid solution phase) [19]. This splitting was interpreted previously due to lesser instrumental resolution falsely in terms of a tetragonally distorted structure with $c_{\text{fcc}} < a_{\text{fcc}}$ [12]. The structure has now been investigated in detail by TEM on a single-phase sample with a composition PdB_{0.184} (annealed for 256h at 360°C). The deviation from the ideal composition (PdB_{0.184} vs. PdB_{1/5}) can be conceived as an ordered mixed occurrence of $[\text{B}_2\text{Pd}_{10}]$ entities (Figure 5.4b) and of isolated $[\text{BPd}_6]$ entities (Figure 5.4a). Different compositions, i.e. different ratios of $[\text{B}_2\text{Pd}_{10}]$ entities of *edge-sharing* octahedra and $[\text{BPd}_6]$ entities of isolated octahedra, lead to a *composition-dependent modulation vector* adjusting the crystal structure to composition by increasing upon lowering the B content, the number of $[\text{BPd}_6]$ units in a systematic fashion, which permits a homogeneity range of the

ordered ‘Pd₅B’ phase¹⁴ [19]. In fact, the structure found for incommensurate ‘Pd₅B’ of the assigned composition PdB_{0.184} is very close to an idealised model structure of the composition PdB_{0.1875} which can be regarded as [B₂Pd₁₀]·[BPd₆] ≡ Pd₁₆B₃, i.e. with a 1:1 ratio of [B₂Pd₁₀] entities and [BPd₆] entities.

All observed/reported low-temperature phases demonstrate only slight monoclinic distortions of the *fcc* Pd host lattice (or none at all as for *pseudocubic* form of Pd₆B). Yet, the observed boron ordering allows a multitude of similar structures built from [B₂Pd₁₀] and/or [BPd₆] entities for a given composition (e.g. possible alternative superstructures for Pd₆B [17]). Indeed, hints of at least one additional yet unresolved low-temperature phase have been observed by TEM analysis performed by the present authors as a two-phase mixture (PdB_{0.193} annealed for 3 weeks at 350°C) with ‘Pd₅B’ (closer to ideal PdB_{1/5} than ‘Pd₅B’ mentioned above of the composition PdB_{0.184}). Hence, although it is claimed that all reported data until now can be ascribed to the described Pd₆B and ‘Pd₅B’ phases, it cannot be excluded that more ordered phases have still to be discovered.

Table 5.1. Overview of the low-temperature phases Pd₆B and ‘Pd₅B’, together with phases as reported in the literature which, according to this work, are identical to either of the Pd₆B or ‘Pd₅B’ phases:

New phase denominations	Previous phase denomination
Pd ₆ B [17]: monoclinic <i>C2/c</i> , <i>pseudotetragonal</i> and <i>pseudocubic</i> , $V_{fcc} = (4.002 - 4.004 \text{ \AA})^3$	- Pd ₁₆ B ₃ : cubic, superstructure hints at $a' = 2a_{fcc}$ [5], $V_{fcc} = (4.005 \text{ \AA})^3$ - Pd ₆ B [10], only indicated in phase diagram
‘Pd ₅ B’ [19]: monoclinic incommensurate, close to $P2_1/n$	- Pd ₁₆ B ₃ , Pd ₅ B [12] tetragonally distorted with $c_{fct} < a_{fct}$ - Pd ₅ B [10], only indicated in phase diagram

¹⁴ This phase is denoted as ‘Pd₅B’ (i.e. between quotes) due to its deviation from the ideal UCl₅ structure prototype with respect to composition and commensurability.

Table 5.2. Pd-B phase crystal structure data: the solid solution and the low-temperature phases.

phase	composition range y (atomic ratio)	Pearson symbol	space group	structure prototype	reference
PdB _{y}	0 to 0.25	$cF(4+4y)^a$	$Fm\bar{3}m$	Cu	[8, 10, 14] ^b
Pd ₆ B	0.160-0.164 ^c	$mC28$	$C2/c$	$V_6C_5\Box^d$	[17]
‘Pd ₅ B’	0.184 ^e	$mP24^f$	$P2_1/n^f$	UCl ₅	[19]

^a $(4+4y)$ denotes the presence of 4 Pd atoms and 4 y B atoms per unit cell.

^b Maximal solubility limit taken from Ref. [10].

^c Upper solubility limit not determined precisely, probably close to 0.167.

^d \Box denotes a vacancy, which is on the site of the boron atom in Pd₆B; the C atom positions are vacancies in the Pd₆B structure.

^e Uncertain homogeneity range.

^f Approximant structure; crystal structure in fact is incommensurate.

5.5. Conclusions for the phase diagram

On the basis of the evaluation given in this paper, an updated tentative phase diagram of the Pd-B system is presented in Figure 5.5. The results from Ref. [4] (Figure 5.1a) for the range of the miscibility gap have been confirmed by the recent data, whereas for the low-temperature phases the findings from Ref. [10] (Figure 5.1b) seem to apply as evidenced by the new, much more detailed data from Refs. [17, 19]. It has been found that both the Pd₆B and the ‘Pd₅B’ phase are monoclinic (Table 1). The shaded regions indicate observed features, which in the previous works often led to confusion:

- I. Miscibility gap: the location of the boundary phase compositions are approximate due to the incomplete demixing into two solid solution phases and the apparent dependence of the ‘final’ state from the initial composition (coherency strains may play a role). The compositions assigned to these phases may differ due to the use of different available expressions, such as Eqs. (5.1-5.3), to relate the composition to the lattice parameter.
- II. For initial compositions in the range of the miscibility gap, observation of so-called ‘three phase samples’ (cf. Chapter 5.3) has been confirmed for the indicated temperatures. Therefore, the exact location of the monotectic temperature of 312°C could not be confirmed unequivocally.

- III. In this range of slightly lower boron contents than Pd_6B , ordering upon cooling from the solid solution phase field resulted in *pseudocubic* Pd_6B ; Pd_6B phase developing from the quenched solid solution with $y < 0.15$ is *pseudotetragonal* and exhibits the same B ordering as *pseudocubic* Pd_6B .
- IV. The homogeneity ranges of the low-temperature phases, in particular ‘ Pd_5B ’, were approximated. The latter is probably not stoichiometric as suggested in Ref. [10]. The occurrence of additional low-temperature phases cannot be excluded.

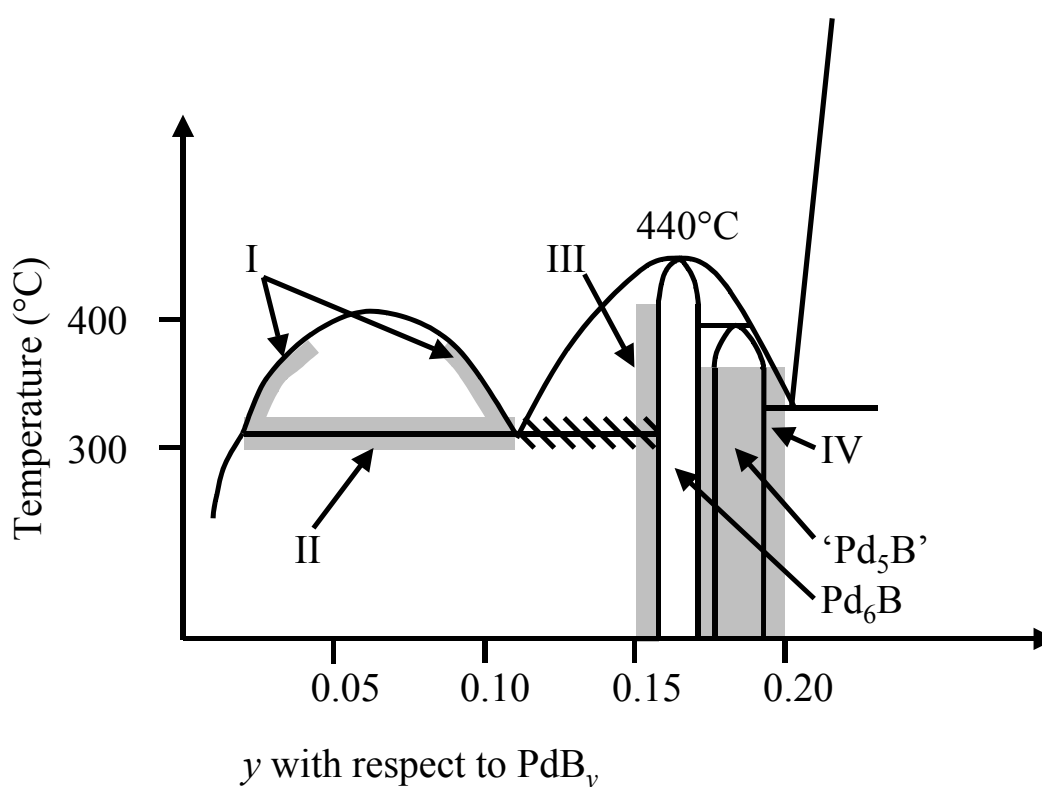


Figure 5.5. Phase diagram showing the miscibility gap corresponding to Ref. [4] and the low-temperature phases corresponding to Ref. [10]. The shaded areas labelled with Roman numbers refer to particular regions in this phase diagram referred to in section 5.5.

6.

Zusammenfassung der Dissertation in deutscher Sprache

6.1. Einleitung

Die einzigartigen Eigenschaften des palladiumreichen Mischkristalls motivierten eine große Zahl von Untersuchungen im System Pd-B, in denen es als Modellsystem für interstitielle Legierungen angesehen wurde. Diese widmeten sich insbesondere der Kristallstruktur [1-5, 11, 12], den thermodynamischen Eigenschaften [4, 6, 86] und der Diffusion von B in Pd [23, 24] oder von H im Mischkristall PdB_y [7]. Hinsichtlich gewisser Schlüsselmerkmale stimmen alle neueren Veröffentlichungen überein [4, 5, 8-12]:

- Pd löst bei Temperaturen über 450°C bis zu ca. 20 Atom-% B (PdB_{-0.25}). B besetzt die Oktaederlücken im kubisch flächenzentrierten Palladiumgitter interstitiell ohne Ausbildung von Fernordnung. Dieser Mischkristall ist eine Hochtemperaturphase, bleibt jedoch bei rascher Abkühlung auf Raumtemperatur erhalten¹⁵.
- Durch Aufnahme von B wird das Palladiumgitter stark aufgeweitet, klar ersichtlich durch die signifikante, weitgehend lineare Zunahme des kubischen Gitterparameters a_{fcc} mit dem Borgehalt (vgl. Eq. (5.1-5.3)).
- Unter 450°C existieren im Bereich zwischen $0.02 < y < 0.11$ eine Mischungslücke und im Bereich zwischen $0.16 < y < 0.20$ eine oder mehrere Tieftemperaturphasen, in denen die Kristallstruktur von Palladium größtenteils erhalten bleibt.

Speziell hinsichtlich der Konstitution des Systems und der Struktur der Tieftemperaturphasen existieren Widersprüche in der Literatur. Mittels eines kombinierten Einsatzes von Röntgen-, Neutronen- und besonders Elektronenbeugung als komplementäre Methoden zur Strukturanalyse konnte die Kristallstrukturen zweier Tieftemperaturphasen identifiziert werden [17-19]. Diese neuen Ergebnisse erlaubten eine Überarbeitung des Phasendiagramms Pd-B im Tieftemperaturbereich.

6.2. Experimentelles

Die verwendeten Legierungen wurden durch mehrfaches Aufschmelzen abgewogener Mengen Pd und B im Lichtbogenofen unter einer schützenden Argonatmosphäre

¹⁵ Messungen innerer Reibung bei Raumtemperatur suggerieren einen Zerfall abgeschreckter Legierungen mit 0.3 bis 2 Atom-% B im Zeitraum von Monaten, was auf eine gewisse Mobilität von B auch bei Raumtemperatur hindeutet. Andere Meßmethoden konnten derartige Beobachtungen bisher nicht bestätigen.

hergestellt¹⁶. Dabei traten kleinere Gewichtsverluste und Abweichungen von den eingewogenen Zusammensetzungen auf. Die Homogenität der Reguli wurde durch Röntgenographie mittels Messung des Gitterparameters überprüft. Die Zusammensetzung der Probe wurde dann anhand von

$$a_0 (\text{Å}) = 3.8920 + 0.6882 y \quad (6.1)$$

bestimmt [11] und auch zur weiteren Bezeichnung der Probe als PdBy verwendet. Die Pulverproben wurden mit einer Diamantfeile üblicherweise an Ober- und Unterseite der Reguli abgefeilt, da dort die größten Zusammensetzungsunterschiede zu erwarten waren. Das erhaltene Pulver wurde nach mehrmaligem Argonspülen unter Vakuum in Quarzkapillaren eingeschmolzen und für 5 min auf 800°C erhitzt, danach wurde die geschlossene Kapillare in Wasser abgeschreckt. Diese Wärmebehandlung wurde bei allen Proben durchgeführt, um durch das Feilen entstandene Spannungen im Material zu beseitigen. Inhomogene Proben wurden nochmals aufgeschmolzen, bis zufriedenstellende Homogenität erreicht worden war.

Für die durchgeführten strukturellen und thermischen Untersuchungen wurden Pulver und Stücke der Gußproben verwendet. Die Pulverproben wurden wie bei den Homogenitätstests hergestellt, die Gußproben wurden durch Diamantsägen oder Funkenerosion vom Regulus getrennt, gesäubert, spannungsfreigeglüht, und für die Elektronenbeugungsexperimente durch Polieren und Ionendünnen (letzteres unter Kühlung mit flüssigem Stickstoff) weiterpräpariert (Details siehe Kapitel 4.3. des englischsprachigen Teils). Für etwaige weitere Wärmebehandlungen wurden die massiven oder pulverförmigen Proben wieder wie oben eingeschmolzen und nach dem Temperaturprogramm in Wasser abgeschreckt, bei den Gußproben wurde dabei die Quarzkapillare zerbrochen.

Die derartig hergestellten und teilweise ausgelagerten Proben wurden mit folgenden Messmethoden untersucht (Details im englischsprachigen Teil):

- Röntgenbeugung wurde zur Untersuchung von Phasenumwandlungen bei weiteren Wärmebehandlungen (z.B. Entmischung, Ordnungsbildung) und zur Charakterisierung der gebildeten Zustände verwendet.
- Transmissionselektronenmikroskopie und Elektronenfeinbereichsbeugung wurde für Mikrostrukturuntersuchungen und zur Identifikation der Überstrukturen der Tieftemperaturphasen durchgeführt.

¹⁶ Genauere Angaben zu Herstellern und Reinheit der verwendeten Ausgangsmaterialien sowie zur Verwendung des Isotops ¹¹B für die Neutronenbeugungsexperimente finden sich im englischsprachigen Teil dieser Arbeit.

- Neutronenpulverdiffraktometrie wurde zu zuverlässigen Messungen der Bragg-Intensitäten eingesetzt und auch zur genauen Bestimmung des Beitrags der Boratome zur gebeugten Intensität. Ersteres war bei der Bestimmung der statischen Auslenkungen der Palladiumatome im Mischkristallbereich vonnöten, letzteres bei der quantitativen Analyse der Überstrukturen in den Tieftemperaturphasen. Die Neutronendiffraktogramme wurden mit Hilfe der Rietveldmethode ausgewertet.
- DSC (Differential Scanning Calorimetry)-Messungen wurden zur Überprüfung von Phasenübergangstemperaturen eingesetzt. Außerdem wurde damit der Erfolg des Abschreckens des Mischkristalls überprüft (siehe 4.4.1. im englischsprachigen Teil).

6.3. Neutronenbeugung: Statische Auslenkungen der Palladiumatome im PdB_y-Mischkristall (0 < y < 0.2)

Das Palladiumgitter wird durch die interstitielle Aufnahme von B ungewöhnlich stark aufgeweitet. Diese Aufweitung lässt große statische Auslenkungen der Palladiumatome von ihren idealen Gitterpositionen in der Umgebung um ein interstitielles Boratom erwarten. Dieses sollte sich in Beugungsexperimenten als eine Abschwächung der Bragg-Intensitäten in Form eines sogenannten statischen Debye-Waller-Faktors, insbesondere bei hohen Beugungswinkeln, auswirken. Für substitutionelle und interstitielle Mischkristalle ist ein Zusammenhang zwischen der mittleren quadratischen Auslenkung der Palladiumatome $\langle u^2 \rangle$ von der Zusammensetzung y und dem sogenannten *volume size factor* Ω_{sf} hergeleitet worden [13].

$$\langle u^2(y) \rangle \sim \Omega_{sf}^2 \cdot y \cdot (1 - y) \quad \text{mit } \Omega_{sf} = \left. \frac{\partial \ln V(y)}{\partial y} \right|_{y=0} \quad (6.2)$$

Für die Untersuchung dieser statischen Auslenkungen wurde Neutronenbeugung verwendet, da bei dieser Messmethode im Vergleich zur Röntgenbeugung keine Beugungswinkelabhängigkeit des atomaren Streufaktors auftritt und wegen geringerer Störeffekte (z.B. Absorption) die gebeugte Intensität zuverlässiger gemessen werden kann. Es wurde eine Reihe von PdB_y-Legierungen (mit $y = 0.05, 0.100, 0.184$) bei 15 K und 300 K untersucht. Die thermischen Auslenkungen von Pd wurden durch den Auslenkungsparameters von reinem Pd angenähert; für die PdB_y-Legierungen wurde im Vergleich zum reinen Pd ein signifikanter Anstieg des statischen Auslenkungsparameters gemessen, der für beide Messtemperaturen ähnlich groß war. Allerdings war keine weitere

nennenswerte Zusammensetzungsabhängigkeit von $\langle u^2 \rangle$ zu erkennen, wie z.B. gemäß Gl. (6.2) zu erwarten wäre. Ein Vergleich mit verfügbaren Daten zu isotypen, nichtstöchiometrischen Übergangsmetallcarbiden und -nitriden ergab einerseits, dass die gemessenen Auslenkungsparameterwerte für die Palladiumatome gemessen am *Volume size factor* ungewöhnlich klein sind und andererseits, dass generell die Größe der statischen Auslenkungen nicht mit der Größe des *volume size factor* skaliert sind (vgl. Abb. 6.1). Dieses steht im Gegensatz zu substitutionellen Mischkristallen, bei denen Gleichung (6.2) für Beispielfälle bestätigt werden konnte [15].

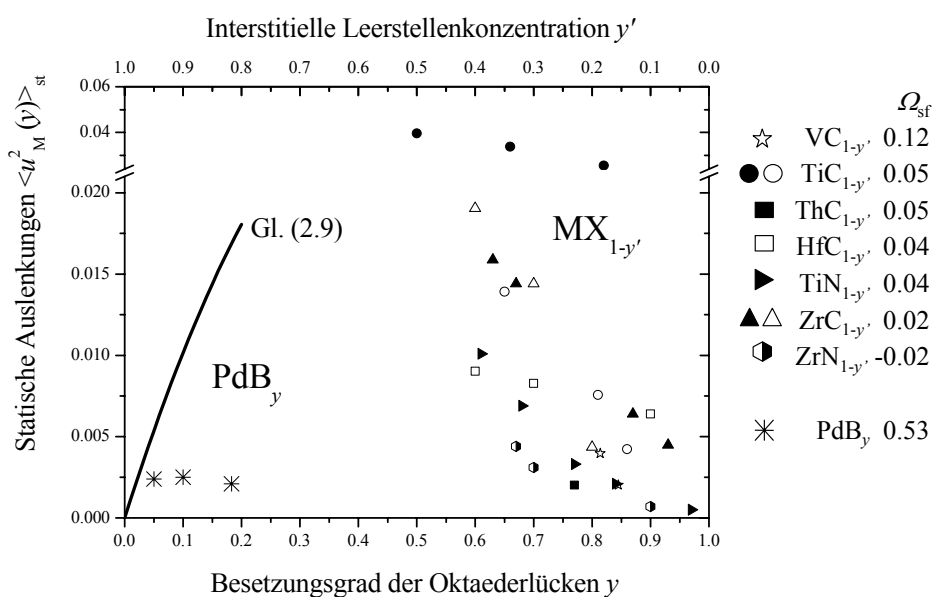


Abb. 6.1. Statische Auslenkungen der kubisch flächenzentriert angeordneten M-Atome in PdB_y (M = Pd) und in anderen isotypen Übergangsmetallcarbiden und -nitriden MX_{1-y'} [38-40, 44]. Die *volume size factoren* Ω_{sf} (vgl. Gl. (6.2)) sind rechts aufgelistet (berechnet anhand von Daten aus den Refs. [42, 43, 45]).

6.4. Eine zeitaufgelöste Methode zur Beschreibung der Entmischung im PdB_y Mischkristall

Die Entmischung der festen Lösung im Bereich der Mischungslücke wurde, ähnlich wie in Ref. [48], mit auslagerungszeit aufgelöster Röntgenbeugung untersucht. Der Verlauf der Entmischung wurde analysiert, indem an jedes einer gewissen Auslagerungszeit entsprechendes Diffraktogramm eine diskretisierte Wahrscheinlichkeitsdichtefunktion der Zusammensetzung, $p(y)$, angepasst wurde. Die Auswertung der auslagerungszeit- und auslagerungstemperaturabhängigen Entwicklung von $p(y)$ ergab:

Drei lokale Maxima der Wahrscheinlichkeitsdichtefunktion $p(y)$ entsprechen den drei Hauptbestandteilen der (partiell) entmischten Proben: Erstens dem Mischkristall (Ausgangsmaterial) mit einem mit der Auslagerungszeit abnehmenden Phasenanteil, zweitens zwei sogenannten „Grenzphasen“ mit zunehmendem Phasenanteil. Die beiden letzteren haben einen höheren, bzw. einen niedrigeren Borgehalt als der sich zersetzende Mischkristall. Diese beiden Borgehalte nehmen zu bzw. ab und nähern sich dabei asymptotisch bestimmten Grenzwerten an, die den Grenzzusammensetzungen der Mischungslücke entsprechen sollten. Wie erwartet ergab sich eine starke Temperaturabhängigkeit der Grenzphasenzusammensetzungen, aber überraschenderweise auch eine nicht zu vernachlässigende Abhängigkeit von der Ausgangszusammensetzung des Mischkristalls. Dieses könnte Einflüssen der Mikrostruktur und Verspannungen zwischen den beiden Phasen zugeschrieben werden. Außerdem zeigen die Röntgenpulverdiffraktogramme selbst für lange Auslagerungszeiten bis zu 8 Wochen verbleibende gebeugte Intensitäten zwischen den Intensitätsmaxima der beiden Grenzphasen (vgl. Abb. 6.2).

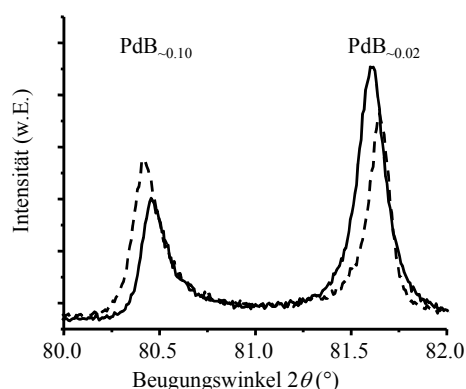


Abb. 6.2. 311-Reflexgruppe des nach Auslagerungszeiten von 8 Wochen bei 340°C scheinbar erreichten Endzustands der Entmischung, aufgenommen für eine $\text{PdB}_{0.064}$ Probe (gestrichelte Linie) und eine $\text{PdB}_{0.064}$ Probe (durchgezogene Linie).

Die Geschwindigkeit der Entmischung hängt von der Auslagerungstemperatur und der Anfangszusammensetzung des Mischkristalls ab. Sie ist schneller für niedrigere Auslagerungstemperaturen und für Zusammensetzungen in der Mitte des Zusammensetzungsbereichs ($y \sim 0.065$). Dieses wird verständlich, wenn man die Gibbs'sche Reaktionsenthalpie für den Entmischungsvorgang als Triebkraft für die Entmischung annimmt.

Sowohl Röntgenbeugungs- und Widerstandsmessungen [4, 6, 48], als auch Messungen des chemischen Potentials [4], bestätigen die Existenz der Mischungslücke. Trotzdem war es bisher nicht möglich, die aus der Entmischung resultierende Mikrostruktur direkt sichtbar zu machen (siehe 4.4.2. im englischsprachigen Teil).

6.5. Die Tieftemperaturphasen Pd₆B und ‚Pd₅B‘

In der Literatur existieren unterschiedliche und teils widersprüchliche Angaben über Anzahl, Zusammensetzungsbereich und Kristallstruktur der Tieftemperaturphasen des Mischkristalls Pd_y. Die Untersuchung und Unterscheidung dieser Tieftemperaturphasen anhand von Röntgenpulverdiffraktometrie gestaltet sich aus mehreren Gründen schwierig. Einerseits bleiben bei sämtlichen beobachteten Tieftemperaturphasen die kubisch dichtgepackte Gitter der Palladiumatome erhalten. Gitterverzerrungen - wahrscheinlich aufgrund von Fernordnung der Boratome - führen nur zu einer maximal geringen Aufspaltung der Fundamentalreflexe (d.h. der Reflexe des Mischkristalls) im Röntgenbeugungsbild. Andererseits ist für Röntgenbeugung der atomare Streufaktor von B deutlich kleiner als der von Pd, wodurch Überstrukturreflexe aufgrund von Besetzungsordnung nur sehr niedrige Bragg-Intensitäten besitzen.

Aus diesen Gründen wurde Neutronenbeugung und Elektronenbeugung eingesetzt. Bei ersterer ist die Streufähigkeit von Bor vergleichbar mit der von Pd, bei zweiterer erlaubt die hohe lokale Auflösung (Elektronenfeinbereichsbeugung) die Aufnahme einkristallähnlicher Beugungsbilder. Anhand der dadurch gewonnenen Erkenntnisse über die Überstruktur und Borordnung in den Tieftemperaturphasen Pd₆B und ‚Pd₅B‘ [17, 19] gelang eine erfolgreiche Interpretation der Röntgenpulverdiffraktogramme und es war möglich, fast alle bisherigen Ergebnisse in einen sinnvollen Zusammenhang einzuordnen [18].

6.5.1. Die Pd₆B-Phase

Die in Ref. [5] als Pd₁₆B₃ bezeichnete geordnete Tieftemperaturphase mit verdoppeltem Gitterparameter $a' = 2a_{fcc}$ (in Bezug auf den Mischkristall) erwies sich als identisch mit der Pd₆B Phase aus Ref. [17]. Gleiches gilt für die Pd₆B Phase aus dem Phasendiagramm in Ref. [10]. Die Kristallstruktur der Pd₆B-Phase wurde durch eine Kombination aus Röntgen-, Neutronen- und Elektronenbeugung bestimmt. Die Struktur ist monoklin und kristallisiert in der Raumgruppe C2/c. Die Überstruktur entspricht einer für V₆C₅ mit defekt-NaCl-Struktur

beobachteten [72] (Bor und Leerstellen in Pd₆B jeweils an den Stellen von Leerstellen und Kohlenstoff in V₆C₅). Die stärksten Überstrukturreflexe dieser monoklinen Pd₆B-Phase stimmen mit denen für Pd₁₆B₃ veröffentlichten [5] überein; der Gitterparameter für die reine Phase ist, unabhängig von der zugeordneten Zusammensetzung, ebenfalls identisch, obgleich unterschiedliche Zusammensetzungen zugeordnet wurden.

Die Besetzungsfernordnung von B in Pd₆B besteht aus abwechselnd partiell besetzten (1/3) und leeren Oktaederlückenschichten, die entlang einer ausgezeichneten $\langle 111 \rangle_{fcc}$ Richtung gestapelt sind. Auf diese Art und Weise werden prinzipiell mögliche kürzeste (*kantenverknüpfte* Oktaeder) und zweitkürzeste (*spitzenverknüpfte* Oktaeder) Abstände von besetzten Oktaederlücken vermieden, der nächste Abstand zwischen zwei benachbarten Boratomen beträgt $\sqrt{6}/2 a_{fcc}$. Die besetzten Pd₆-Oktaeder kann man formal als ‚isolierte‘ [BPd₆]-Einheiten betrachten. Das alleinige Auftreten solcher isolierter [BPd₆]-Einheiten kann nur für Zusammensetzungen bis $y = 1/6$ realisiert werden. Für höhere Borgehalte müssen entweder *kanten-* oder *spitzenverknüpfte* Paare von Pd₆-Oktaedern besetzt werden (siehe ‚Pd₅B‘ und Abb. 6.4).

Die Pd₆B-Phase wurde in zwei verschiedenen Formen beobachtet, die je nach Zusammensetzung des ausgelagerten Mischkristalls auftraten (vgl. Abb. 6.3):

- *Pseudokubisches* Pd₆B entsteht in Legierungen mit einer Zusammensetzung, die Pd₆B entspricht oder bezüglich des Borgehalts knapp darunter liegt. Die Fundamentalreflexe des Mischkristalls spalten im Röntgenbeugungsbild nicht auf, nachdem sich die Ordnung der Boratome einstellt, obwohl die in der Elektronenbeugung anhand der Überstrukturreflexe beobachtete Ordnung monoklin ist. Für den beobachteten Zusammensetzungsbereich (PdB_{0.158} bis PdB_{0.163}) war das Abschrecken des Mischkristalls schwierig; die Fernordnung der Pd₆B-Phase stellt sich sehr schnell ein. Für PdB_{0.158}-Pulver wurde nach erfolglosem Abschrecken (und dementsprechendem Einstellen der Ordnung der Boratome) bei weiterer Auslagerung bei 280°C oder 360°C eine Zersetzung in eine Mischkristallphase niedrigeren Borgehalts (vgl. Phasendiagramm) und einer bezüglich B leicht angereicherten Pd₆B-Phase beobachtet. Die *pseudokubische* Struktur der Pd₆B-Phase blieb dabei jedoch erhalten.
- *Pseudotetragonales* Pd₆B (d.h. die Aufspaltung im Röntgenbeugungsmuster entsprach einer tetragonalen Gitterverzerrung mit $c_{ft} > a_{ft}$) wurde bei Auslagern des Mischkristalls niedrigeren Borgehalts erhalten, z.B. für PdB_{0.144}. Auslagern bei 280°C

oder bei 360°C ergibt anscheinend die gleichen Zweiphasengleichgewichte wie bei *pseudokubischem* Pd₆B hergestellt aus PdB_{0.158}, jedoch mit dem Unterschied einer *pseudotetragonalen* Aufspaltung der Fundamentalreflexe des Pd₆B (vgl Abb X). Die Zusammensetzungen der beiden Formen von Pd₆B im Gleichgewicht mit dem Mischkristall nach Auslagerung bei 280°C oder 360°C waren anhand des Volumens der Einheitszellen identisch.

Das Auftreten der *pseudotetragonalen* und *pseudokubischen* Form des Pd₆B wurde durch die unterschiedliche Bildung der geordneten Phase aus dem Mischkristall erklärt. Während PdB_{0.158} beim Abschrecken die Pd₆B Struktur (auch wenn sie sich bei weiterem Auslagern noch zersetzt) durch wenige Platzwechsel von Boratomen annehmen kann, ist dies für PdB_{0.144} oder niedrigere Borgehalte nur nach vorheriger langreichweitiger Diffusion von B und Zersetzung des ursprünglichen Mischkristalls möglich. Dadurch bildet sich je nach Ausgangszusammensetzung ein anderes Gefüge aus welches z.B. durch Kohärenzspannungen zwischen unterschiedlich orientierten geordneten Domänen. Diese Gefüge beeinflusst die Ausprägung der Verzerrung des Palladiumgitters offensichtlich stark.

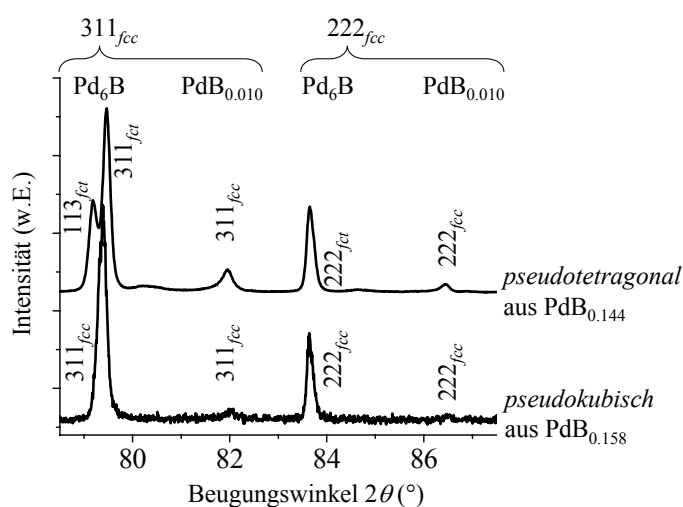


Abb. 6.3. Röntgenpulverdiffraktogramme von PdB_{0.144} (70 h ausgelagert) und PdB_{0.158} (3 Wochen ausgelagert) Proben im Zweiphasengebiet unterhalb der monotektischen Temperatur. Die zu erwartende Entmischung in die Pd₆B-Phase und eine entsprechende Mischkristallphase ist klar erkennbar. Für ausgelagerte Zusammensetzungen nahe bei Pd₆B formt sich die Pd₆B-Phase in ihrer pseudokubischen Form, für niedrigere Borgehalte wird eine pseudotetragonale Aufspaltung beobachtet.

6.5.2. Die ‚Pd₅B’-Phase

Die früher als tetragonal verzerrt beschriebene Pd₅B-Phase mit einer kritischen Temperatur von 385°C [12] war dort fälschlicherweise als die Pd₁₆B₃-Phase [5] identifiziert worden. Anstelle dessen ist diese Phase wohl identisch mit der Pd₅B-Phase [10] mit etwas höherem Borgehalt als Pd₆B [17]. Mit der für Pd₆B beschriebenen Kombination aus Neutronen- und Röntgenpulverdiffraktometrie sowie mit Elektronenfeinbereichsbeugung wurde diese, im folgenden als ‚Pd₅B’ bezeichnete Phase (die Anführungsstriche ergeben sich wegen der zum Teil großen Abweichung von der Idealzusammensetzung PdB_{1/5}), als monoklin geordnet mit einer inkommensurabel modulierten Besetzung der Oktaederlücken durch Boratome identifiziert [19]. Die Struktur kann durch einen kommensurablen Approximanten PdB_{1/5} beschrieben werden, der eine zu UCl₅ isotype Kristallstruktur hat (Raumgruppe *P2₁/n* [61], Pd und B jeweils an den Stellen von Cl und U). Dabei liegt eine geordneten Besetzung von 1/5 der Oktaederlücken durch B Atome vor.

Die für Pd₆B beobachtete Überstruktur kann noch durch isolierte Einheiten von besetzten Pd Oktaedern [BPd₆] gebildet werden (s.o.). Für höhere Borgehalte müssen jedoch entweder *kantenverknüpfte*- oder *spitzenverknüpfte* [BPd₆]-Oktaederpaare gebildet werden. In der ‚Pd₅B’ Struktur ist ausschließlich ersteres der Fall, wodurch isolierte [B₂Pd₁₀]-Einheiten auftreten. Eine Begründung für die Bevorzugung der Bildung *kantenverknüpfter* [BPd₆]-Oktaeder lässt sich aus der lokalen Aufweitung der Pd₆-Oktaeder durch den Einbau von B ableiten: Die Palladiumatome werden von den Boratomen nach außen ausgelenkt um die Pd-B Abstände zu vergrößern. Bei *kantenverknüpften* Oktaederpaaren können sich diese Auslenkungen vektoriell addieren, bei *spitzenverknüpften* Oktaederpaaren ist eine Auslenkung des gemeinsamen Palladiumatoms auf diese Art nicht möglich und somit kann die energetisch günstigere Verlängerung des Pd-B Abstandes nicht einfach realisiert werden (vgl. Abb. 6.4).

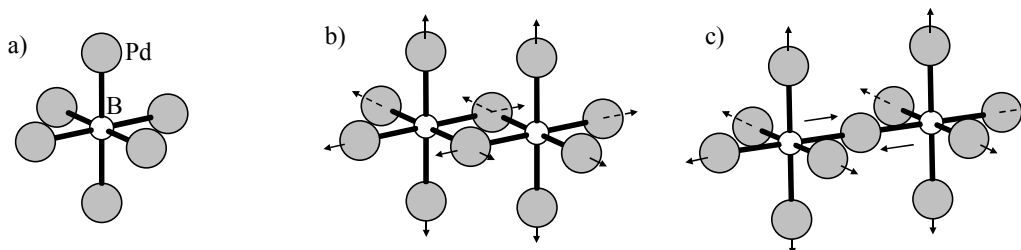


Abb. 6.4. Ein (a) einzelner [BPd₆]- Oktaeder und Paare von (b) *kanten-* und (c) *spitzenverknüpften* [BPd₆]-Oktaedern. Die Richtungen der Auslenkungen der Palladiumatome durch den Einbau der Boratome sind durch Pfeile gekennzeichnet.

Die monokline Ordnung von B in der ‚Pd₅B‘-Phase zeigt sich im Röntgenbeugungsbild durch eine charakteristische Aufspaltung der Fundamentalreflexe. Diese Aufspaltung wurde in Ref. [12] aufgrund von nicht ausreichender instrumenteller Auflösung in den Röntgenpulverdiffraktogrammen als tetragonale Verzerrung interpretiert.

Die Struktur der ‚Pd₅B‘-Phase wurde u.a. anhand einer Probe der Zusammensetzung PdB_{0.184} (ausgelagert bei 360°C für 256 h) untersucht. Die Abweichung von der idealen Zusammensetzung (PdB_{0.184} im Vergleich zu PdB_{1/5}) wird durch ein gemischtes aber geordnetes Auftreten von isolierten [BPd₆]-Einheiten und kantenverknüpften [B₂Pd₁₀]-Einheiten realisiert. Verschiedene Zusammensetzungen, also unterschiedliche Verhältnisse zwischen [BPd₆]-Einheiten und [B₂Pd₁₀]-Einheiten, ergeben einen zusammensetzungsabhängigen Modulationsvektor der inkommensurablen Kristallstruktur. Die Zusammensetzung PdB_{0.184} liegt beispielsweise nahe an der Idealzusammensetzung PdB_{0.1875}, bei der eine Struktur gemäß [B₂Pd₁₀]·[BPd₆] ≡ Pd₁₆B₃ auftreten kann, d.h. gebildet mit einem 1:1 Verhältnis von [B₂Pd₁₀]- und [BPd₆]-Einheiten.

6.6. Zusammenfassung und Phasendiagramm

Alle beobachteten Tieftemperaturphasen zeigen nur leichte monokline Verzerrungen des Palladiumgitters (oder gar keine sichtbaren, wie beispielsweise beim *pseudokubischen* Pd₆B). Allerdings erlaubt das beobachtete Ordnungsprinzip von B in Pd eine Vielzahl von möglichen Strukturen aus [B₂Pd₁₀]- und/oder [BPd₆]-Einheiten. In der Tat wurden mit Elektronenfeinbereichsbeugung Hinweise auf mindestens eine weitere Tieftemperaturphase gefunden, die wahrscheinlich ebenfalls dem genannten Prinzip gehorcht. Alle früheren veröffentlichten Daten zu den Tieftemperaturphasen können jedoch mit den hier genauer charakterisierten Phasen Pd₆B und ‚Pd₅B‘ erklärt werden.

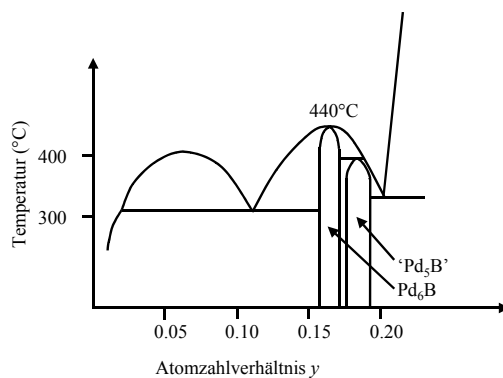


Abb. 6.5. Pd-B Phasendiagramm wie in Kapitel 5 des englischsprachigen Teils im Detail beschrieben.

References

- [1] H. Brodowsky, H.-J. Schaller, Ber. Bunsenges. 71, 926 (1967).
- [2] H. Brodowsky, H.-J. Schaller, T. Metall. Soc. AIME 245, 1015 (1969).
- [3] H. Brodowsky, H.-J. Schaller, Ber. Bunsenges. 76, 360 (1972).
- [4] H. Brodowsky, H.-J. Schaller, Ber. Bunsenges. 80, 656 (1976).
- [5] R. A. Alqasmi, H. Brodowsky, H.-J. Schaller, Z. Metallkd. 73, 331 (1982).
- [6] R. A. Alqasmi, H. Brodowsky, H.-J. Schaller, Z. Metallkd. 77, 637 (1986).
- [7] K. D. Allard, T. B. Flanagan, E. Wicke, J. Phys. Chem. 74, 298 (1970).
- [8] B. Lengeler, Solid State Comm. 55, 679 (1985).
- [9] H. Ipsier, P. Rogl, J. Less-Common Met. 82, 363 (1981).
- [10] P. Rogl, Phase diagrams of ternary metal-boron-carbon systems, ASM International, Materials Park, OH (USA), 1998, pp. 234-241.
- [11] M. Beck, M. Ellner, E. J. Mittemeijer, Acta Mater. 49, 985 (2001).
- [12] M. Beck, M. Ellner, E. J. Mittemeijer, Z. Kristallogr. 216, 591 (2001).
- [13] M. A. Krivoglaz, X-ray and Neutron Diffraction in Nonideal Crystals, Springer (Berlin, Heidelberg, 1996).
- [14] T. G. Berger, A. Leineweber, E. J. Mittemeijer, P. Fischer, Phys. Stat. Sol. (a) 201, 1484 (2004); (Chapter 2 of this dissertation).
- [15] W. W. Webb, J. Appl. Phys. 33, 3546 (1962).
- [16] T. G. Berger, A. Leineweber, E. J. Mittemeijer, M. Knapp, Z. Kristallogr. Suppl. accepted; (Chapter 3 of this dissertation).
- [17] T. G. Berger, A. Leineweber, E. J. Mittemeijer, C. Sarbu, V. Duppel, P. Fischer, in preparation; (Chapter 4 of this dissertation).
- [18] T. G. Berger, A. Leineweber, E. J. Mittemeijer, in preparation; (Chapter 5 of this dissertation).
- [19] A. Leineweber, T. G. Berger, E. J. Mittemeijer, in preparation.
- [20] G. Hägg, Z. Phys. Chem. B 12, 33 (1931).
- [21] G. Hägg, Z. Phys. Chem. B 12, 221 (1931).
- [22] P. K. Liao, K. E. Spear, M. E. Schlesinger, J. Phase Equilib. 17, 340 (1996).
- [23] H. Brodowsky, J. Fleischhauer, M. Kayashima, Scr. Metallurg. 17, 541 (1983).

- [24] K. Albertsen, H. Brodowsky, H.-J. Schaller, H.-J. Wernicke, *Z. Metallkd.* 85, 339 (1994).
- [25] A. G. Khachaturyan, *Theory of Structural Transformations in Solids*, Wiley (1983).
- [26] H. W. King, *J. Mater. Sci.* 6, 1157 (1971).
- [27] A. J. C. Wilson, *International Tables for Crystallography, Volume C*, Kluwer Academic Publishers (Dordrecht, 1995).
- [28] E. J. Sonneveld, R. Delhez, *PROFIT for Windows User's Guide*, Philips Analytical X-Ray, first edn., Almelo, 1996.
- [29] H. Meyer, *Program for the refinement of lattice parameters*, MPI for Metals Research (Stuttgart, 1993).
- [30] P. Fischer, G. Frey, M. Koch, M. Könnecke, V. Pomjakushin, J. Schefer, R. Thut, N. Schlumpf, R. Bürge, U. Greuter, S. Bondt, E. Berruyer, *Physica B*, 276-278, 146 (2000).
- [31] V. Petricek, M. Dusek, *Jana2000: The crystallographic computing system*, Institute of Physics, Praha, Czech. Republic.
- [32] P. Thompson, D. E. Cox, J. B. Hasting, *J. Appl. Crystallogr.* 20, 79 (1987).
- [33] B. E. Warren, *X-ray Diffraction*, Dover Publications, Inc. (New York, 1990).
- [34] R. A. Young, *The Rietveld Method*, IUCr, Oxford University Press (Oxford, 1993).
- [35] V. F. Sears, S. A. Shelley, *Acta Crystallogr. A* 47, 441 (1991).
- [36] N. Binsted, M. J. Pack, M. T. Weller, J. Evans, *J. Am. Chem. Soc.* 118, 10200 (1996).
- [37] M. A. Krivoglaz, *Theory of X-Ray and Thermal-Neutron Scattering by Real Crystals*, Plenum Press (New York, 1969).
- [38] A. I. Gusev, *Disorder and Order in Strongly Nonstoichiometric Compounds*, Springer, (Berlin, 2001).
- [39] I. Khidirov, I. Karimov, V. T. Em, V. E. Loryan, *Neorg. Mater.*, 17, 2106 (1981).
- [40] I. I. Timofeeva, L. A. Klochkov, *Variation of lattice periods and static distortions in homogeneity region of transition metal carbides*, *Refractory Carbides*, G. V. Samsonov (Naukova Dumka), (Kiev, 1970) pp.143-147.
- [41] I. Karimov, V. T. Em, I. Khidirov, F. Faizullaev, *Fiz. Met. Metalloved.* 44, 184 (1977).
- [42] L. Ramqvist, *Jernkontorets Ann.* 152, 517 (1968).
- [43] L. Ramqvist, *Jernkontorets Ann.* 152, 465 (1968).
- [44] V. Moisy-Maurice, C. H. de Novion, *Acta Crystallogr. A* 36, 916 (1980).
- [45] W. Lengauer, *J. Alloys Compd.* 186, 293 (1992).

- [46] R. Delhez, Th. H. de Keijser, E. J. Mittemeijer, *Fresenius Z. Anal. Chem.* 312 (1), 1, (1982).
- [47] R. L. Snyder, J. Fiala, H.-J. Bunge, *Defect and Microstructure Analysis by Diffraction* (Oxford University Press), 1999, chapter 26 -27.
- [48] M. Beck, E. J. Mittemeijer, *Z. Metallkde.* 92, 1271 (2001).
- [49] M. Knapp, C. Baetz, H. Ehrenberg, H. Fuess, *J. Synchrotron Rad.* 11, 328 (2004).
- [50] A. A. Coelho, TOPAS, General Profile and Structure Analysis Software for Powder Diffraction Data, V2.0, Bruker AXS GmbH, Karlsruhe, Germany, Release 2003.
- [51] A. R. Stokes, A. J. C. Wilson, *Proc. Phys. Soc.* 56, 174 (1944).
- [52] A. Leineweber, E. J. Mittemeijer, *J. Appl. Cryst.* 37, 123 (2004).
- [53] I. J. Good, R. A. Gaskins, *Biometrika* 58, 255 (1971).
- [54] R. Louboutin, D. Louër, *Acta Cryst. A* 25, 335 (1969).
- [55] A. A. Coelho, *J. Appl. Cryst.* 33, 899 (2000).
- [56] H. J. Goldschmidt, *Interstitial Alloys*, Butterworth & Co., London (UK), 1967.
- [57] J. Hauck, K. Mika, *Progr. Solid State Chem.* 28, 1 (2000).
- [58] H. Okamoto, D. J. Chakrabarti, D. E. Laughlin, T. B. Massalski, *Binary Alloy Phase Diagrams*, Second Edition (Ed. T. B. Massalski), ASM International, Materials Park, OH (USA), 1998, 1, pp. 358-362.
- [59] M. L. Huggins, *Phys. Rev.* 27, 638 (1926).
- [60] J. P. Dismukes, J. G. White, *Inorg. Chem.* 3, 1220 (1964).
- [61] G. S. Smith, Q. Johnson, R. E. Elson, *Acta Crystallogr.* 22, 300 (1967).
- [62] J. Hauck, *Acta Crystallogr.* A36, 228 (1980).
- [63] B. J. Kooi, M. A. J. Somers, E.J. Mittemeijer, *Met. Mater. Trans. A* 27, 1055 (1996).
- [64] T. Mohri, J. M. Sanchez, D. de Fontaine, *Acta Metallurg.* 33, 1171 (1985).
- [65] M. I. Pekelharing, A.J. Böttger, M. A. J. Somers, E.J. Mittemeijer, *Metall. Mater. Trans A*30, 1945 (1999).
- [66] R. Hoppe, *Angew.Chem.* 78, 52 (1966).
- [67] G. C. Mather, C. Dussarat, J. Etourneau, A. R. West, *J. Mater. Chem.* 10, 2219 (2000).
- [68] A. I. Gusev, A. A. Rempel, *J. Phys. C: Solid State Phys.* 20, 5011 (1987).
- [69] B. V. Khaenko, V.V. Kuhol, *Dop. Akad. Nauk. Ukr. A*, 78 (1987).
- [70] K. Cenzual, L. M. Gelato, M. Penzo, E. Parthé, *Acta Crystallogr.* B47, 433 (1991).
- [71] U. Müller, *Acta Crystallogr.* A35, 188 (1979).
- [72] A. I. Gusev, A. A. Rempel, *Phys. Stat. Sol. (a)* 135, 15 (1993).

- [73] A. Strecker, U. Bader, M. Kelsch, U. Salzberger, M. Sycha, M. Gao, G. Richter, K. van Benthem, *Z. Metallkde.* 94, 290 (2003).
- [74] P. H. Jouneau, P. Stadelmann, EMS Online. Centre Interdepartemental de Microscopie Electronique EPFL, Lausanne (CH).
- [75] J. Billingham, P. S. Bell, M. H. Lewis, *Phil. Mag.* 25, 661 (1972).
- [76] L. Pauling, *The Nature of the Chemical Bond*. 3rd edition, Cornell University Press, Ithaca, NY (USA), 1960.
- [77] E. Parthé, K. Yvon, *Acta Crystallogr.* B26, 153 (1970).
- [78] K. Hiraga, *Phil. Mag.* 7, 1301 (1973).
- [79] J. P. Landesman, A. N. Christensen, C. H. de Novion, N. Lorenzelli, P. Convert, J. *Phys. C: Solid State Phys.* 18, 809 (1985).
- [80] S. K. Dhar, S. K. Malik, R. Vijayaraghavan, *Mater. Res. Bull.* 16, 1557 (1981).
- [81] L. E. Tergenius, T. Lundstroem, *J. Solid State Chem.* 31, 361 (1980).
- [82] U. Eibenstein, W. Jung, *J. Solid State Chem.* 133, 21 (1997).
- [83] F. Povolo, H. O. Mosca, *Phys. Stat. Sol. (a)* 164, 609 (1997).
- [84] C. D. Gelatt, jr., A. R. Williams, V. L. Moruzzi, *Phys. Rev. B* 27, 2005 (1983).
- [85] H. Brodowsky, *Z. Phys. Chem NF* 44, 129 (1965).
- [86] H. Brodowsky, H.-J. Schaller, H.-J. Wernicke, *Z. Metallkd.* 70, 631 (1979).
- [87] P. Villars, M. Berndt, K. Brandenburg, K. Cenzual, J. Daams, F. Hulliger, T. Massalski, H. Okamoto, K. Osaki, A. Prince, H. Putz, S. Iwata, *PAULING FILE, Binaries Edition*, ASM International, Materials Park, OH (USA), 2002.

Curriculum Vitae

Tilman Georg Berger

born on September 12th 1973 in Stuttgart (Germany)

School:

1980-1984 primary school: Grundschule Schönaich
1984-1993 high school: Max Planck Gymnasium Böblingen

Academic studies:

1993-1999 Universität Stuttgart,
Faculty of Physics

1999-2000 Universität Stuttgart,
2. Phys. Institute,
diploma thesis: *Installation and Application of a Magnetic Field
Stabilization Device for high-field Bitter Magnets*

Dissertation:

2001-2004 PhD student at Max Planck Institute for Metals Research,
Institute for Materials Science, Stuttgart,
Promoter: Prof. Dr. Ir. Eric J. Mittemeijer
Research Theme: *Phase transformations in interstitial
Pd-B alloys*

Danksagung

Die vorliegende Dissertation wurde an der Universität Stuttgart und am Max-Planck Institut für Metallforschung, Stuttgart, angefertigt.

Herrn Prof. Dr. Ir. E. J. Mittemeijer, meinem Doktorvater, gilt mein besonderer Dank für die Aufnahme in seine Abteilung. Seine Betreuung und Förderung und die regelmäßigen wissenschaftlichen Diskussionen waren von großer Bedeutung für den Erfolg der Arbeit.

Herrn Prof. Dr. T. Schleid danke ich für die freundliche Übernahme des Mitberichts.

Zum Gelingen dieser Arbeit hat Herrn Dr. A. Leineweber in großem Maße beigetragen. Als täglicher Ansprechpartner stand er mit seiner herausragenden fachlichen Kompetenz, insbesondere im Bereich der Strukturanalyse, immer zur Verfügung.

Herrn Dr. P. Fischer und Dr. D. Sheptyakov sei für ihre tatkräftige Unterstützung und die ausführlichen wissenschaftlichen Diskussionen im Laufe der Neutronenbeugungsmessungen am SINQ/PSI gedankt. In gleicher Weise möchte ich auch Herrn C. Sarbu, Fr. V. Duppel und Herrn Dr. L. Kienle für die intensive Betreuung bei der Durchführung einiger Elektronenfeinbereichsbeugungsexperimente danken.

Allen Mitarbeitern der Abteilung Mittemeijer möchte ich für das gute Arbeitsklima und die gute Zusammenarbeit danken.

Nicht zuletzt möchte ich noch meinen Eltern und meiner Freundin Sonja für ihre Unterstützung danken.